Silicon Thin Film Concepts for Building Integrated Photovoltaic Applications

Von der Fakultät für Mathematik und Naturwissenschaften
der Carl von Ossietzky Universität Oldenburg
zur Erlangung des Grades und Titels eines
Doktors der Naturwissenschaften
(Dr. rer. nat.)
angenommene Dissertation

von
Nies Reininghaus
geboren am 17.02.1985
Werther (Westf.)

angefertigt am
DLR Institut für Vernetzte Energiesysteme e. V.
Carl-von-Ossietzky-Straße 15, 26129 Oldenburg

Oldenburg, den 15.01.2019

Gutachter: Prof. Dr. Carsten Agert

Zweitgutachter: Prof. Dr. Sascha Schäfer

Drittgutachter: Prof. Dr. Jürgen Parisi

Tag der Disputation: 13. Dezember 2018

Abstract

The growing market of building integrated photovoltaic applications and projects increases the demand for versatile and novel photovoltaic modules that can be easily tailored to the specific requirements of the architects and installers. Thin-film silicon solar cells have a significant advantage over other photovoltaic module types because of their high flexibility: They can be made homogeneously transparent with tunable transmission and can be deposited on different types of substrates like ceramic or plastic.

In addition, silicon photovoltaic modules are made from abundant resources and do not use any hazardous materials which allows for easy recycling. Long term stability of the cell itself has been shown to be almost unlimited and the manufacturers guarantee up to 30 years.

This thesis will show that using doped layers made out of phosphine doped hydrogenated microcrystalline silicon oxide in tandem cells for building integrated photovoltaic applications poses a significant advantage compared to conventional layers. To achieve the same lifetime as the conventional layers, they have to be stabilized. This can be accomplished by inserting thin SiO_2 atom diffusion barrier layers into the stack. In order to reduce the production time of multi-junction cells for building integrated photovoltaic applications, the absorption of the silicon absorber material can be enhanced by adding germanium. Using the advantages of a band-gap reduced by the addition of germanium enables the absorption of light with a longer wavelength. The μc-$Si_{1-X}Ge_X$:H absorbers investigated show the same efficiency as the μc-Si:H absorbers but with reduced thickness.

For applications like fences or facades it can be advantageous for a photovoltaic module to be able to collect sunlight from both sides. Those types of modules are called bifacial modules. The project explores simulations of different planes of orientation and tilt were simulated in terms of irradiance for bifacial modules. Results show that, even for Oldenburg, vertically installed modules with high bifaciality can receive more irradiance than monofacial modules with optimum tilt and orientation.

While tandem-junction thin-film silicon solar cells show an inferior performance because of the current matching problem caused by shifting irradiation conditions, it was found that a bifaciality of over 95 % can be achieved for single junction cells by redesigning the n-layer for high energy light transparency. This can be done by alloying the material with carbon, oxygen and decreasing its thickness which increases the transparency. The result is a semi transparent bifacial solar module which meets the demands of many building integrated photovoltaic applications in the most efficient way.

Kurzfassung

Der schnellwachsende Markt von Gebäudeintegrierten Photovoltaik Produkten und -Anwendungen erhöht den Bedarf an vielseitigen und neuartigen Photovoltaik-Modulen, die einfach auf die verschiedenen Bedürfnisse der Architekt∗innen und Installateur∗innen zugeschnitten werden können. Dünnschicht Silizium Photovoltaik hat in diesem Feld durch ihre Flexibilität einen großen Vorteil gegenüber anderen Photovoltaik Modultypen. Sie kann ganzflächig und einstellbar-transparent hergestellt werden und sie kann auch auf Keramiken oder Plastik abgeschieden werden. Zusätzlich wird die Silizium Photovoltaik mit einfach verfügbaren und ungiftigen Rohstoffen hergestellt, was das Recycling stark vereinfacht. Die Langzeithaltbarkeit der Zelltechnologie ist fast unendlich, weshalb die Hersteller sogar eine Haltbarkeit von bis zu 30 Jahren garantieren.

Diese Arbeit zeigt, dass phosphin dotierte Schichten aus mikrokristalliniem Siliziumoxid in Tandem-Zellen für Gebäudeintegrierten Photovoltaik Anwendungen einen großen Vorteil gegenüber herkömmlichen Schichten bieten. Diese müssen allerdings mit dünnen Schichten aus SiO_2 stabilisiert werden, um das Diffundieren von Atomen zu verhindern. Um die Depositionszeit (und damit die Produktionskosten) dicker Tandemzellen zu verringern, können die Silizium Absorberschichten mit Germanium verbessert werden. Germanium hat eine kleinere Bandlücke und ermöglicht so die Absorption von langwelligerem Licht. μc-$Si_{1\text{-}X}Ge_X$:H Absorber wurden untersucht, die bei gleicher Effizienz eine geringere Schichtdicke aufweisen.

Für Anwendungen wie Zäune oder Fassaden kann es von Vorteil sein, wenn ein Solarmodul von der Front- und der Rückseite Licht absorbieren kann. Solarmodule, die dies können, werden bifaciale Module genannt. Eine Simulation von Solarmodulflächen in Oldenburg zeigt sogar eine höhere Einstrahlleistung für bifaciale Module in senkrechter Aufstellung unabhängig der Orientierung im Vergleich zu konventionell installierten, monofacialen Solarmodulen.

Tandem-Junction Solarmodule sind durch Strom-Matching Probleme, die durch die veränderlichen Einstrahlbedingungen verursacht werden, in bifacialen Anwendungen stark beeinträchtigt. Einfach-Stapel Solarzellen können durch eine Modifikation der n-Schicht auf Transparenz in Solarzellen mit einer sehr hohen Bifacialität von 95 % verwandelt werden. Diese eignen sich hervorragend für verschiedenste, teiltransparente building integrated photovoltaic (BIPV) Anwendungen.

List of Abbreviations

IPCC	Intergovernmental Panel on Climate Change
GHG	greenhouse gas
LCA	life cycle assessment
RF-PECVD	radio frequency plasma enhanced chemical vapour deposition
STC	standard test conditions ($25\,^{\circ}\mathrm{C}$, $1000\,\mathrm{W/m^2}$, AM1.5G)
LCOE	levelized costs of electricity
AM1.5G	air mass 1.5 global
HIT	heterojunction with intrinsic thin-layer
BIPV	building integrated photovoltaic
UV-VIS-NIR	ultraviolet-visible-near infrared
PTFE	polytetrafluoroethylene
c-Si	crystalline silicon
GEBA	global energy balance archive
$\mathbf{J_{sc}}$	short-circuit current density
$\mathbf{V_{oc}}$	open-circuit voltage
MPP	maximum power point
$\mathbf{J_{mp}}$	current density at maximum power
$\mathbf{V_{mp}}$	voltage at maximum power
FF	fill factor
η	power conversion efficiency
$\mathbf{R_{s}}$	series resistance
$\mathbf{R_{sh}}$	shunt resistance
$\mathbf{J_{ph}}$	photocurrent
EQE	external quantum efficiency
OMO	oxide-metal-oxide
TCO	transparent conducting oxide
a-Si:H	hydrogenated amorphous silicon
ITO	indium tin oxide
ZnO:Al	aluminum-doped zinc oxide

μc-Si:H	hydrogenated microcrystalline silicon
n-μc-$Si_{1\text{-}X}O_X$:H	phosphine doped hydrogenated microcrystalline silicon oxide
CO_2	carbon dioxide
sccm	standard cubic centimeter per minute
PH_3	phosphine
ARC	anti reflection coating
μc-$Si_{1\text{-}X}Ge_X$:H	hydrogenated microcrystalline silicon germanium
LID	light-induced degradation
GeH_4	germane
a-SiGe:H	hydrogenated amorphous silicon germanium
GD	glow discharge
rf	radiofrequency
ToFMS	time of flight mass spectrometry
OES	optical emission spectrometry
BR	back reflector
SPP	surface plasmon polaritons
SiO_2	silicon dioxide
PVF	polyvinylfluorid

List of Figures

List of Tables

Contents

1

Introduction and Outlook

1.1 Motivation

With the constant world-wide growing need for photovoltaic installations and an expected addition of 104 GW of installed photovoltaic power in 2018 [1], finding new places to integrate solar cells becomes more and more important. Especially for dense urban areas, where most of the power is consumed and space is limited, new and more efficient solutions for integrating solar cells need to be found. But also rural areas demand more space-saving solutions, since the option to install free standing solar power plants competes with the agricultural use of the same space. Thus, as the amount of installed solar modules increases, new ways to integrate power generation have to be found. For buildings with large physical footprints, as the Gigafactory in Nevada, the optimal solution is obvious: The whole roof of the building will be covered with solar panels reaching a planned 70 MWp of power [2], in this case used to improve the production of batteries for electrical vehicles. The largest rooftop array to date only has a capacity of 11.6 MWp [2]. For dense urban areas, which do not offer that much rooftop space, using BIPV offers various options to find space for photovoltaic generators. Integrating the power generation into existing structures is a sustainable solution which has many advantages: The structure has to be build regardless of this additional purpose, using photovoltaic modules as part of the structure therefore saves material and makes the building more cost-effective.

One use case that illustrates this is the building of skyscrapers or big office buildings with facades made out of glass. Since glass accounts for a main part of the costs of a solar module and the offices behind the glass facade have to be shaded from the sun, it makes sense to integrate the photovoltaic modules into the facade. This way, the

Figure 1.1: Test of a solar roadway in the Netherlands. Generating approximately 70 kWh per square meter per year. Picture from http://www.solaroad.nl/

need for air conditioning is reduced by shading the occupants and a potential return of investment is created by the option to sell the power. The costs of the solar modules can be reduced by the amount of money the facade of glass without them plus the shading would have costed. A good overview of large scale BIPV projects can be found here[1].

Another very prominent example is the solar roadway in the Netherlands: solar modules integrated into the roadway for bicycles on 70 m as depicted in figure 1.1. Though the anti-slip coating of the glass still has to be improved, the test has been deemed a success and will be expanded by additional 20 m of roadway soon [3]. This first test has accumulated so much attention, even outside the Netherlands, that France decided to build 1000 km of solar roadway over the next years [4]. The first kilometer was already build and is now being tested for endurance and productivity[2].

The integration of solar modules in structures such as fences and facades, however, has some advantages over the use on roadways. Modules in fences or facades are cleaned by the rain, easier to maintain, and are not so likely to be covered by snow or shadowed by traffic. Moreover, they are significantly less expensive than roadway modules, because only minimal changes are necessary to turn a standard module into a module usable in a fence or facade element.

---

[1] https://www.onyxsolar.com/projects

[2] https://arstechnica.com/cars/2016/12/worlds-first-solar-road-opens-in-france/

Silicon wafer modules have already been integrated into glass used as semi-transparent noise barriers. This use of wafer modules, however, has the negative effect of creating a check board shadow pattern that is uncomfortable to look at when driving by in a train or a car. A better option is the use of thin-film silicon solar cells that have a homogenous appearance and can be made transparent homogeneously by reducing the layer thickness and omitting the back reflecting layer. The thin-film silicon technology is as durable as the silicon wafer technology but has a lower power conversion efficiency. Up to this date, there are only few building integrated thin-film silicon photovoltaic products on the market. Especially bifacial products with tunable transparency that can be installed vertically seem to be missing on the marked. The investigation of this particular module type will be one of the focuses of this thesis.

Attending international workshops on the current state of BIPV endeavors has shown some challenges that need to be addressed: Big BIPV projects like those linked above are done with the primary goal of publicity. Architects are sometimes forced to make aesthetic decisions that make no sense for power generation. Some project reports even show that photovoltaic modules installed in a building were not electrically connected because there was no person responsible for the electrical design of the BIPV project. Most of the solar module manufacturers build standard size modules and are not flexible enough to provide customizable BIPV products. The market for BIPV products has to expand in order to cater to the different needs of the BIPV projects. That also creates an additional problem: Because BIPV products are varied and are often customized for a specific project, there is no general certification of solar modules as building material. Most BIPV projects have to hire a consultant at the end of the project to check the safety of each new material and module without certification used. This significantly increases the costs of any BIPV project. An improvement of this situation can be reached either by a government funded initiative to subsidize certification or the certification has to be initiated and financed by the manufacturers.

1.2 Outlook

The following chapters will concentrate on the investigation of the material basics to create a building integrable, semi-transparent, and stable thin-film silicon solar cell that can generate power no matter which side faces the sun. In short, this thesis will focus on improving the performance of the window layer, the whole absorber, and an exemplary BIPV application: a vertically installed bifacial module. In order to increase the amount of light reaching the absorber in BIPV solar cells, the project investigates the use of n-μc-$Si_{1-X}O_X$:H as a window layer. Next, the absorber itself is improved by the use of germanium and its improved absorption. Finally, the application of a bifacial module in vertical installation is investigated as well as the method of how to increase a thin-film silicon solar cell's bifaciality.

- Chapter 3 concentrates on investigating how using doped layers made out of n-μc-$Si_{1-X}O_X$:H can improve the performance of tandem cells for BIPV applications. It identifies an improved performance with the 3 layers and a way to stabilize the layer against degradation.
- Chapter 4 focuses on the reduction of the production time of multi-junction cells for BIPV applications by enhancing the absorption of the silicon absorber material by adding germanium. It demonstrates that the same current density generation can be reached with reduced absorber thickness and production time.
- Chapter 5 investigates the changes that have to be made to thin-film silicon solar cells in order to be able to collect sunlight from both sides. Different planes of orientation and tilt are simulated in terms of irradiance for bifacial modules. It is shown that free standing and vertical bifacial modules are exposed to more sunlight than conventional modules in optimum tilt and orientation. Modification of the n-layer can turn thin-film silicon solar cells into bifacial cells with an bifaciality of 98 %.

2

Fundamentals

2.1 Thin-Film Silicon Solar Cells

As a backdrop to the investigations done in this project, the following section will give a brief introduction into the working principle and fabrication of thin-film silicon solar cells.

The fabrication of thin-film silicon solar cells can be described with the following steps: First, a glass substrate covered with transparent conducting oxide (TCO) is cleaned and inserted into a vacuum chamber which is kept at a temperature between 150 and 220 °C during processing. Then, the silicon layers are deposited with radio frequency plasma enhanced chemical vapour deposition (RF-PECVD). During this process, different source gas combinations of Silane - SiH_4, Hydrogen - H_2, Phosphine - PH_3, Diborane - B_2H_6, Methane - CH_4, Germane - GeH_4, and carbon dioxide - CO_2 are let into the chamber with the substrate and mix at pressures around 4 to 12 mbar. Two opposite planar electrodes with a gap of 1 cm with the substrate placed in between are supplied with an alternating voltage. The resulting radiofrequency (rf) electric field ignites the source gases between the plates to form a plasma. In the plasma, the source gases are dissociated into atoms, radicals, molecules, and ions. Some of those molecules reach the substrate and sublime on the surface. The chamber surfaces and the other electrode are covered with molecules as well. The layer growth and formation of amorphous or microcrystalline material depends on the plasma and surface conditions and can be fine-tuned by changing the deposition gas composition, pressure in the chamber, temperature, and power of the alternating voltage. Generally, amorphous material is formed by using lower pressures, less power, and less hydrogen diluted process gas compared to microcrystalline deposition conditions[1]. Then, the cells are covered with TCO again and interconnected by laser-scribing. Alternatively to defining the area of measurement by a laser scribe, a common technique is to omit the TCO layer and evaporate a silver pad as a back contact and reflector layer. Because of the bad in-plane conductivity of the silicon layers, the area covered by the silver is the only area where charge carriers can be extracted.

Thin-film silicon solar cells have a great advantage compared to other thin-film solar cell types like Cu(In,Ga)Se_2 (CIGS) that are deposited at up to 500 °C [6]. The gas in the plasma and the electron temperature are not in thermal equilibrium [5]. The chemical reactions on the surface of the substrate and in the plasma are initiated by electrons of high kinetic energy. The substrate temperature can therefore be kept at relatively low temperatures of about 220 °C. Contrary to most other stable solar cell technologies, this enables the deposition of thin-film silicon solar cells on flexible and cheap substrates like metal and plastic foils, ceramic, and even fiber glass composites. Figure 2.1 a) shows the schematic layer setup of a thin-film silicon solar cell. The light passes through the glass substrate, through a TCO and the positively-doped layer (p-layer) before being absorbed in the intrinsic layer (i-layer). Some of the light is absorbed by the glass, TCO, or p-layer and is lost for conversion to energy. Therefore, these window layers are kept as transparent as possible for the wavelengths the i-layer is able to absorb[2].

2.2 Structure and Functional Principle

When electron and hole pairs are created by an absorption of a photon in the intrinsic layer, they start drifting apart due to the internal potential created by the very thin p-layer and the negatively-doped layer (n-layer). The internal potential is created because the silicon in the p-layer is doped with boron. This creates a negatively charge because boron has less electrons than silicon. The same works for the n-layer: It is doped with phosphor and therefore charged positive because phosphor has more electrons silicon. This is only true when the n-layer and the p-layer are electrically connected by the i-layer and the surplus electrons from the n-layer have moved to the

---

[1] For more information on the deposition procedure see [5]

[2] Which wavelengths of light an absorber is able to convert to charge carriers depends on the band-gap. Amorphous silicon has a mobility gap of 1.75 eV and microcrystalline silicon has a band-gap of 1.1 eV [7: p. 37]. Amorphous silicon can absorb light up to a wavelength of approximately 800 nm while microcrystalline silicon can absorb light up to a wavelength of 1100 nm due to the different band gap

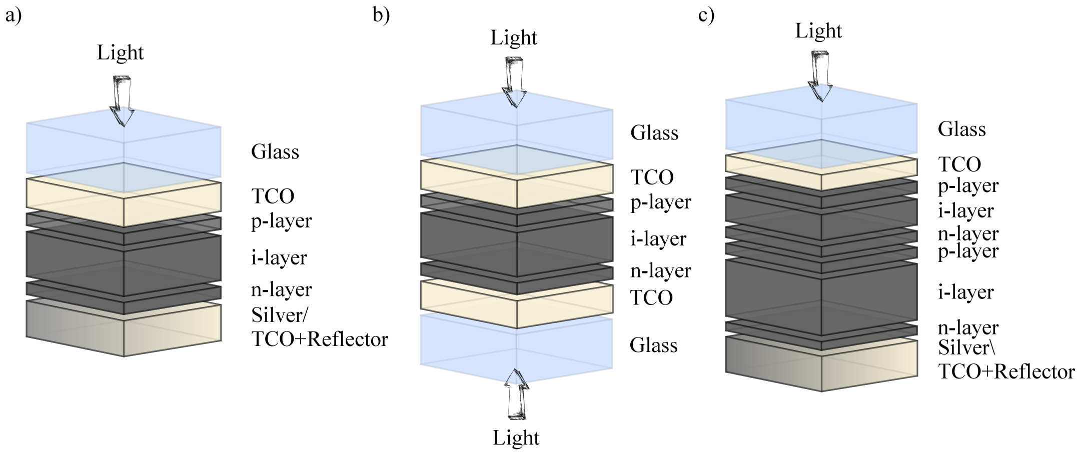

Figure 2.1: Structure of a): A single junction thin-film silicon solar cell, b): A single junction bifacial thin-film silicon solar cell, c): A tandem junction thin-film silicon solar cell. Layer thicknesses are not scaled.

holes in the p-layer. The electrons drift towards the n-layer and the holes towards the p-layer. Because the holes have a lower lifetime than the electrons in amorphous silicon, most amorphous solar cells are illuminated through the p-layer. Most high energy light is absorbed in the first few nanometers and the holes have only a few nanometers to travel towards the p-layer. The charge carriers can then be collected at the TCO electrodes. More information on the detailed workings can be found in [7].
Figure 2.1 b) shows the structure of a bifacial single junction cell that can be illuminated from both sides. In contrast to the structure of the cell stack displayed in a) and c), no reflecting layer in combination with the TCO or silver is deposited on top of the n-layer.
Figure 2.1 c) displays the stack structure of a tandem silicon thin-film device. In most cases, a microcrystalline silicon solar cell is stacked on top of an amorphous cell. Tandem devices are solar cells connected in series. Two solar cells can be connected in a series connection in two ways. The conventional way which is used to build wafer modules is to connect the plus contact of one wafer cell with the minus contact of the next wafer cell. This way the resulting module voltage is the sum of the voltage of all series connected wafer cells. The resulting module current is the lowest current of all series connected wafer cells because it limits all other cells. One can think (as a rough analogue) of a module of serially connected solar cells as different segments of a pipe connected to each other. The steepness of all pipes connected will add to the potential of the water flowing through it which can be seen analogue to the voltage. The

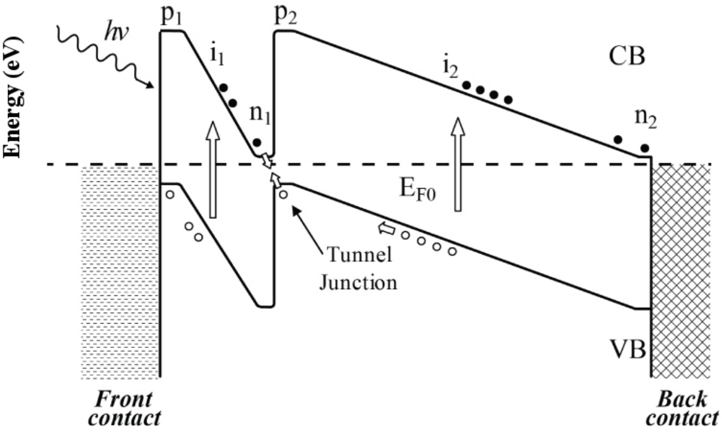

Figure 2.2: Schematic band diagram of a tandem-junction device with a tunnel junction in between. Figure abbreviated from [8]

circumflex of the smallest pipe will determine the amount of water flowing through it and can be seen analogue to the current flowing.

In thin-film silicon solar modules, two or more solar cells can be connected in series by depositing them on top of each other with similar ramifications as the serially connected wafer cells show. Two hydrogenated amorphous silicon (a-Si:H) cells deposited on top of each other with a open-circuit voltage (V_{oc}) of 0.9 V each will result in a multi-junction or tandem cell with 1.8 V. Three a-Si:H cells with 0.9 V deposited on each other result in a triple junction cell of 2.7 V. When stacking the cells on top of each other, one has to take into account that the topmost cell gets the most light while all cells below only get what is left after passing the cells above. The light reaching a cell determines the amount of current it generates. As with the wafer cells, the lowest current determines the current generated by the multi-junction cell. Therefore, the cell stack has to be tailored in a way that each cell is generating the same amount of current. This is called current matching and results in the cell at the bottom of the stack being the thickest. This technique has an additional benefit: The band-gap of each cell in the stack can be tailored to the light it is supposed to absorb. The stack therefore starts with an absorber material with a high band-gap, as for example amorphous silicon, and ends with a subcell absorber with low band-gap like silicon-germanium. A band-gap close to the energy of the light it is absorbing will result in less thermalization losses. Hydrogenated microcrystalline silicon with a band-gap of 1.1 eV, for example, absorbs light with an energy of 1.9 eV but looses 0.8 eV of that energy to thermalization. Fabricating a multi-junction solar cell is not as easy as depositing two cells on top of each other. For a tandem solar cell of two cells connected in series, a tunnel junction or recombination junction has to be inserted at the interface of the two sub-cells. The interface consists of the n-layer of the topcell and the p-layer of the bottom cell (see figure 2.1 c) and figure 2.2. As described before, the generated charge carriers move to the doped layers. The electrons move to the n-layer and the holes to the p-layer. Where the n-layer of the topcell is in contact with the p-layer of the bottom cell, the generated charge carriers have to recombine fast and completely. This is also called band-to-band tunneling [9] and can be seen in figure 2.2 indicated with an arrow. Otherwise, a charge would build up that would hinder the extraction of charge carriers at the front- and back-contact of the multi-junction stack. In order to promote the recombination at the interface, a thin and highly doped p- or n-layer can be included as a recombination junction. This layer has to have a large density of defects or dangling bonds to enable recombination. Additionally, it has to be thin enough in order to absorb the least amount of light possible. The recombination junction is also called tunnel junction because tunneling can be used to help charge carriers to reach the area where the other type is in majority. Electrons can, for example, tunnel to the defects in a p-doped recombination layer where the holes are in majority. Tunneling is possible when the recombination layer is highly doped and the Fermi level is close to the band edge. This state is easier to achieve with microcrystalline doped layers [7: p. 243]. Therefore, most recombination layers are made from microcrystalline doped layers and not amorphous doped layers. For multi-junction stacks, a lower $\mathrm{V_{oc}}$ and higher series resistance ($\mathrm{R_s}$) for a non functional or bad functioning (tunnel) recombination junction can be expected[3].

2.3 Characterization Methods

2.3.1 Sunsimulator

The electrical properties of the solar cells are characterized by measurement with a WACOM super solar simulator class AAA with a dual xenon/halogen lamp setup. The measurements were carried out under standard test conditions (25 °C, 1000 $\mathrm{W/m^2}$, AM1.5G) (STC). A Frauenhofer ISE solar cell is used to reference the measurements. The solar cell is illuminated with 1000 $\mathrm{W/m^2}$ and the air mass 1.5 global (AM1.5G) spectrum provided by combining the xenon and halogen lamp and keeping the temperature at 25 °C. Simultaneously, the measurement setup sweeps the voltage of the

---

[3] More information on different multi-junction stacks and recombination layers can be found in [7]

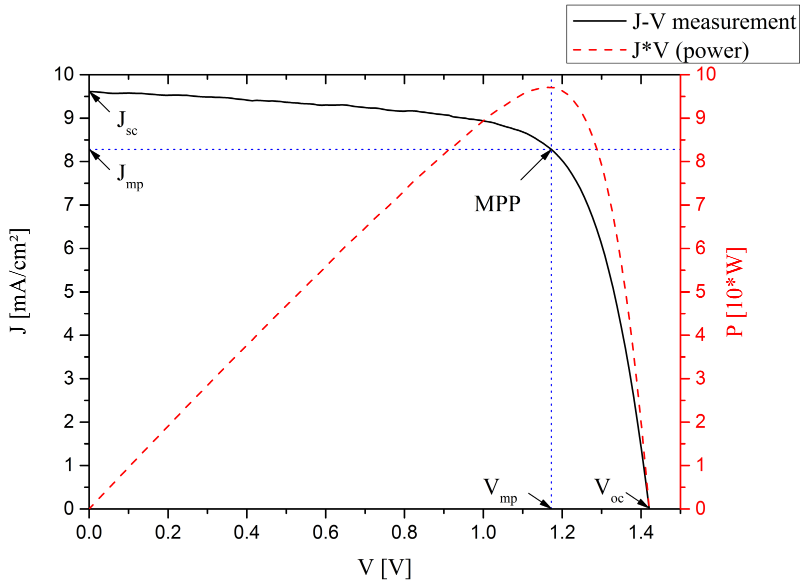

Figure 2.3: Voltage sweep of a tandem cell under STC and the product of J, V, and the position of different electrical values.

cell while measuring the current output. To avoid contact resistances, the samples are contacted by the four point method [10]. For bifacial cells a black background under the cell was chosen.

Figure 2.3 shows such a voltage sweep of a silicon thin-film tandem solar cell. Most of the important electrical characteristics of a solar cell can be derived from this measurement. As indicated in figure 2.3, the short-circuit current density (J_{sc}) is the current density at the intersection of the graph with the y-axis. Similarly, the V_{oc} value is the voltage where the graph intersects the x-axis. To determine the maximum power point (MPP) of a solar cell, one has to look for the maximum of the product of J and V as indicated by the red stroked line in figure 2.3. The values of J and V at this point are called current density at maximum power (J_{mp}) and voltage at maximum power (V_{mp}).

Measuring these four values enables the calculation of another important electrical parameter of a solar cell: the fill factor (FF). Graphically, the FF is a measure of the squareness of a solar cell and is also the area of the largest rectangle which will fit in the J-V curve.

$$\mathrm{FF} = \frac{P_{max}}{J_{sc} \cdot V_{oc}} = \frac{J_{mp} \cdot V_{mp}}{J_{sc} \cdot V_{oc}} \tag{2.1}$$

The power conversion efficiency (η) of a solar cell can be calculated using the following formula

$$\eta = \frac{P_{max}}{P_0} = \frac{J_{sc} \cdot V_{oc} \cdot FF}{P_0} \qquad (2.2)$$

To determine the R_s and the shunt resistance (R_{sh}) of a solar cell, a J-V curve like the one in figure 2.3 can be used. R_s represents an ohmic resistance equivalent to the ohmic resistance in the connections to the solar cell and all ohmic resistances within the cell stack [7: pp. 160]. It can be determined by measuring the resistance at V_{oc} (equal to the slope at this point) when the current flowing through the device equals zero.

R_{sh} can be measured the same way: The slope at J_{sc} is equal to R_{sh}. The R_{sh} is also called parallel resistance and represents not only actual ohmic shunts, but is additionally used to represent the recombination losses within the solar cell [7: pp. 161]. This does not take into account that the recombination losses depend on the photocurrent (J_{ph}) aswell [7: pp. 162].

For measuring bifacial solar cells, the recently proposed method from the Fraunhofer ISE is used [11]. The module is measured from both sides under STC conditions while covering the respective backside with a black cloth.

2.3.2 External Quantum Efficiency

The wavelength-dependent conversion efficiency of the solar cells are measured by using the external quantum efficiency (EQE) setup from RERA SOLUTIONS called SpeQuest. The setup uses xenon light for wavelength between 300 and 450 nm and a halogen lamp for wavelength between 450 and 1100 nm. The light is chopped and run through a monochromator before hitting the solar cell. To simulate real live conditions, the solar cell can be illuminated with white, infra-red, or blue bias light simultaneously. A bias voltage can be applied to measure the cell at J_{sc}. The photocurrent of each wavelength shown on the solar cell is transformed by a transimpendance amplifier and sent to a lock-in amplifier that filters the measurement for a signal with the chopper frequency. Because of the chopper in combination with the lock-in amplifier, no bias or ambient light can contribute to the signal. This way the number of charge carriers generated can be compared to the number of incident photons of a certain wavelength. Consequently, EQE values are given in percent. The measurement setup is referenced with the same Fraunhofer ISE cell as described in section 2.3.1.

2.3.3 UV-VIS Spectrometry

The ultraviolet-visible-near infrared (UV-VIS-NIR) measurement setup can be used to measure transmittance and reflection of samples in relation to the wavelength. A Cary 5000 from Varian is used. As indicated by the name, the wavelength range of this device spans from ultraviolet to near infrared (200 to 2500 nm) using a Deuterium lamp for the 200 - 350 nm and a Tungsten-halogen lamp for the wavelength range $>$ 350 nm.

A monochromator unit splits the light from the lamps into a wavelength dependent spectrum. The sample is placed into that monochromatic beam path in front of an integrating sphere that collects all transmitted light and focuses it onto a detector when measuring optical transmittance of a sample. The sample is placed at the back of the integrating sphere to collect only the reflected light from the sample for reflectance measurements.

The detector is changed at 800 nm from a photomultiplier tube to a thermostated Lead Sulphide detector. This explains a slight increase in signal noise in the measurements at wavelength around 800 nm.

The measurements are baseline corrected by measuring a polytetrafluoroethylene (PTFE) plate for 100 % reflection and dark light absorbent material for 0 % reflection. All cells are measured from the glass substrate direction.

2.3.4 Degradation Measurement

Cell degradation is performed using a ultra violet light source SOL2000 from the company Hoenle AG that can emit light in the range of 295 to 3.000 nm with intensities in excess of 1000 $\mathrm{W/m^2}$. The lamp reaches a very high irradiation efficiency (how much input power the lamp converts into light) of 44 % in the range of 295 to 780 nm and is therefore suited to mimic outdoor irradiance conditions. Solar cells are placed beneath the lamp at a distance of 50 cm in a chamber covered with reflective coating at the inside. The temperature of the cells is monitored and kept at 25 °C by modulating the airflow in and out of the degradation chamber. The solar cells are taken out of the chamber and measured with the sunsimulator (see section 2.3.1) at predefined intervals. The commonly agreed time for degradation measurements is 1000 h [12]. After this time the performance change due to the Staebler-Wronski effect is considered minimal [13].

2.3.5 Raman

The principle of raman measurements is based on inelastic interaction of light with the sample. The measurement is therefore non destructive.

When monochromatic light is shown onto a sample, the incoming photon can interact with the lattice vibrations of the crystal. The collective excitations in a periodic, elastic arrangement of atoms or molecules in condensed matter can be described as a theoretical particle which is called phonon.

The interaction between photon and phonon can result in an increase or decrease of the energy of the back-scattered photon. The resulting shift of the photon energy is displayed in the raman measurements and contains information about the crystallinity, internal stress, and material composition [14–16].

The crystalline volume fraction of a silicon alloy can be gauged by looking at the different modes of the raman signal. Figure 2.4 shows the baseline corrected measurement of an hydrogenated microcrystalline silicon germanium (μc-$Si_{1\text{-}X}Ge_X$:H) absorber layer. As indicated in the figure, the signal can be deconstructed using Gaussian peaks. The four modes fitted to the curve, are the transverse optical (TO) phonon mode at 520 cm^{-1} of microcrystalline silicon, the TO mode of the amorphous fraction at 480 cm^{-1}, the longitudinal optical (LO) mode of the amorphous fraction at 450 cm^{-1}, and a crystalline phase at 505 cm^{-1} attributed to small crystallites and interfaces [17, 18]. Using the area of the fits, a raman crystallinity ϕ_c can be calculated using the following formula:

$$\phi_c = \frac{I_{505} + I_{520}}{I_{505} + I_{520} + I_{480} + I_{450}} \tag{2.3}$$

Where I_W is the area of the Gaussian fit for each peak at the inverse wavenumber W. It is called raman crystallinity because the exact relation to the real crystalline volume fraction is still being debated.

The indicated peak position in figure 2.4 is shifted from the TO mode at 520 cm^{-1} of microcrystalline silicon to lower inverse wave numbers because of the germanium contend in the alloy. The shift occurs because of the 4 % lower lattice constant of germanium in comparison to silicon which induces stress in the lattice [19].

This shift of the crystalline peak position is linear to the germanium content in the layer for low contents (below 20 %) of germanium and can be approximated by the following formula [20–23]:

$$\omega^{\text{Si-Si}} = 520.7 - 70x_{\text{Ge}} \tag{2.4}$$

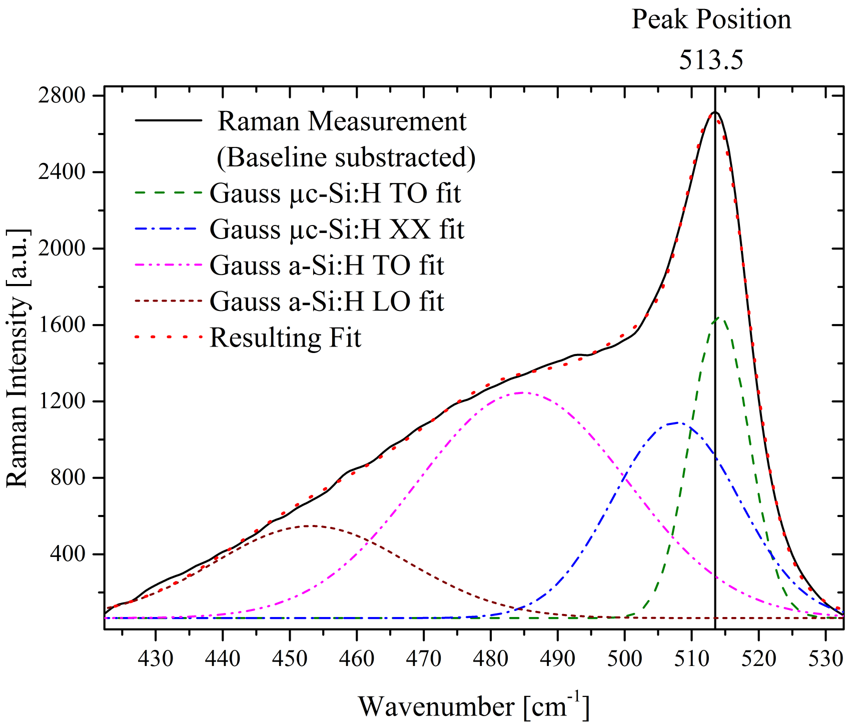

Figure 2.4: Raman signal of a µc-$Si_{1-X}Ge_X$:H absorber layer with amorphous and microcrystalline content. The different phonon modes are fitted with Gaussian peaks. The crystalline peak position is indicated at 513.5 1/cm.

Where x_{Ge} is the germanium content in the layer and $\omega^{\text{Si-Si}}$ is the position of the shifted crystalline peak. The measurements are performed using a raman spectrometer of the type Senterra from Bruker Corporation. The laser excitation frequency (488 nm, 633 nm, or 785 nm) is chosen according to the required information depth. The intensity of the laseris low enough to avoid the induction of laser crystallization.

2.3.6 Radiofrequency Pulsed Glow Discharge Time of Flight Mass Spectroscopy

To determine the composition of a material layer by layer in terms of atomic mixture is especially challenging for thin-film silicon solar cells, because of the involvement of very thin layers (down to 5 nm thickness) and very low concentrations of substances (e.g. 10^{19}cm^{-3} for boron in the p-layer [7: pp. 312]).

Some of the material of the sample is removed using glow discharge (GD). A plasma is formed on the sample surface by applying a potential in the kV range between the sample and an anode while the space between the electrodes contains a discharge gas (typical: Ar).

The gas is ionized into electrons and positive ions by the strong electric field which accelerates the ions towards the sample surface. The impact of the ions on the sample surface releases material into the gas phase where the ions can be detected. This process is called sputtering. The use of GD has the benefits of being fast (a few minutes per measurement), a very good depth resolution and low matrix effect (material matrix influencing the measurement). For samples with poor conductivity and to increase the sensitivity of the measurement, the sputtering process can be pulsed with rf. This also reduces the thermal load that needs to dissipate from the sample. The pulsed plasma can be used to utilize different phases of ionization mechanisms. The greatest sensitivity can be achieved in the afterglow region, microseconds after the pulse was turned off [24].

To detect the different particles sputtered off the sample, optical emission spectrometry (OES) can be used. This technique uses the optical emissions of the plasma to determine the atomic particles in it by their distinctive emission spectrum.

For rf-GD it has been proven feasible to use time of flight mass spectrometry (ToFMS) to analyze the composition of the sputtered material because the measurement is fast enough to keep up with the pulse intervals. ToFMS measures the flight time of particles through an electrical field reversing the flight direction. The flight time is thereby mass-dependent and can be used to determine the particle.

The instrument used consists of a rf-GD bay unit from Horiba Jobin Yvon coupled to a fast orthogonal time-of-flight mass spectrometer from TOFWERK, Switzerland, with a micro channel plate detector. The GD anode is a modified Grimm-type chamber from EMPA, Switzerland[4].

2.3.7 Meteonorm

Meteonorm is a meteorological database with diverse features for energy applications and is widely used for PV simulation [26]. Most of the data for the database is taken from the global energy balance archive (GEBA), the Swiss database compiled by MeteoSwiss, and the World Meteorological Organization Climatological Normals combining data from 8325 meteorological stations worldwide. The database includes historical data of temperature, humidity, wind speed, and precipitation for the periods 1961 - 1990 and 2000 - 2009. Solar radiation data is available for the periods 1981 -

---

[4] More details of the setup and measurement procedures can be found in [24, 25]

1990 and 1991 - 2010. The station data is enhanced by data from five geostationary satellites on a global grid with a horizontal resolution of 3 km for Europe and Northern Africa and 8 km for the rest of the world.

For locations far from a weather station in the database, Meteonorm can interpolate the data with with a 3-D inverse distance model [27] with additional North-South distance penalty [28]. The program is able to calculate hourly and daily data of all parameters using the methodology by Aguiar et al. [29] and new Markov transition matrices. The comprehensive database allows to generate a typical year based on the data of past years for all locations on the planet.

The calculation to determine the diffuse irradiance on tilted surfaces is based on the model from Perez et al. [30]. Experimental validations of the model show an error value below $1\,\mathrm{W/m^2}$ for yearly values [31][5].

---

[5] More information on the theories and the database can be found on the website [31]

3

Phosphine Doped μc-SiO:H Window Layers for Building Integrated Photovoltaic Applications

The purpose of this chapter is to show how stable n-μc-$Si_{1\text{-}X}O_X$:H layers can be used to increase the light reaching the absorber layers. These can then be used in BIPV and bifacial BIPV applications. Since using doped layers made out of n-μc-$Si_{1\text{-}X}O_X$:H is a fairly new idea in the development of thin-film silicon solar cells, there is no research on the long-term stability of those layers and no focus on BIPV application up to this date.

After an overview of current research about n-μc-$Si_{1\text{-}X}O_X$:H layers and their application in BIPV solar cells the chapter gives a short outline of the necessary experimental and theoretical background used in the following sections. In order to investigate the material properties of the phosphine doped n-μc-$Si_{1\text{-}X}O_X$:H layers, very thin tandem cells ($d < 1$ μm) feasible for BIPV modules are used. The application of n-μc-$Si_{1\text{-}X}O_X$:H layers show a distinct advantage in efficiency over the usage of conventional layers.

Different aging and material property tests are performed to understand the metastability of n-μc-$Si_{1\text{-}X}O_X$:H layers. Glow discharge measurement shows a movement of atoms in the layer that can be stopped by inserting very thin SiO_2 atom diffusion barrier layers. The rf-GD-ToFMS measurements of the tandem devices were performed by Dr. Beatriz Fernandez at the University of Oviedo in Spain.

The results of this chapter were published in [32].

3.1 μc-SiO:H

3.1.1 Overview

Thin-film silicon solar cells can be installed as semi-transparent modules with adjustable transmission for vertically installed modules on facades or noise-barrier walls. This feature makes thin-film devices superior to conventional modules build out of wafer cells because for wafer modules transparency cannot be adjusted homogeneously over the module area. In order to increase the effectiveness of thin tandem cells as BIPV building material, it is advantageous that the doping layers are as transparent as possible. Until now, only the doping layer facing the sun has been optimized for transparency. With the new challenges of BIPV application, it is necessary for the rear facing doping layer to be transparent as well. Transparent n-layers also increase the bifaciality of any vertically installed modules greatly.

In addition, one of the primary goals for thin film silicon solar cell production is the reduction of active layer material. A reduction in deposition time without performance loss leads to faster fabrication times and consequently to reduced levelized costs of electricity (LCOE). An absorber thickness reduction would also improve the device stability for a-Si:H cells and tandem devices [33, 34].

Light trapping is the main tool used to achieve high absorption of incident light in thinner absorbers [35]. This can be done by modifying the glass substrate by laser scribing [36]. A more common approach is to use a textured TCO at the front [37, 38] and a reflecting layer at the back of the cell called back reflector (BR) made out of silver, aluminum, or reflective paint. The rough texture at the front of the cell reduces the optical loss caused by reflection at the front surface, while the BR minimizes the absorption loss at the back surface of the solar cell [39]. This technique also increases the path length of incident light in the absorber material and therefore increases J_{sc}.

To achieve semi-transparent thin-film silicon solar cells, the BR has to be transparent and the n-layer has to have a good transmittance as well. This can be achieved by using n-μc-$Si_{1-X}O_X$:H layers in addition to using only a very thin silver layer ($d < 10$ nm) [40] or by perforating the silver to increase its transparency [41].

The performance of an evaporated silver layer can be enhanced by inserting a sputtered 80 nm thick aluminum-doped zinc oxide (ZnO:Al) layer in between the silver and the cell stack [42]. The disadvantage of this material combination is the extra step required due to the sputter process used for the deposition of ZnO:Al, which increases the costs. In recent years, a new material combination has gained the interest of industry and research groups alike. n-µc-$Si_{1\text{-}X}O_X$:H can be deposited either as n-type or p-type material using the doping process used for conventional doped layers. Its optical and electrical properties can be adjusted over a wide range by varying the deposition conditions.

The discovery of micro crystalline silicon as a non-degrading absorber material for tandem thin-film solar cells [43] can be described as major milestone in the increase of efficiency for silicon thin-film solar modules available on the market. The next milestone for improvement of efficiencies is the recent discovery of µc-SiO:H as material for window layers [44, 45], intermediate reflectors [46, 47], and dual function back reflectors [48, 49] leading to new record cells [50, 51].

Research on the n-µc-$Si_{1\text{-}X}O_X$:H layers started in 2010 with the development of a window layer for n-i-p solar cells [52]. The growth direction for those cells is contrary to the growth direction in p-i-n cells. Achieving a crystalline layer for the n-µc-$Si_{1\text{-}X}O_X$:H layer is therefore very difficult and strongly dependent on the front TCO type and roughness. Only a few month later, work on n-µc-$Si_{1\text{-}X}O_X$:H in p-i-n configuration was published demonstrating that the standard n-layer can be completely replaced with a performance similar to a BR in TCO/Ag configuration [53].

The n-µc-$Si_{1\text{-}X}O_X$:H layer has been applied to single junction amorphous p-i-n cells [49], tandem cells [48], and triple junction devices with initial efficiencies in excess of 16 % [50]. The n-µc-$Si_{1\text{-}X}O_X$:H layers increase the efficiency of single a-Si:H cells more than 13 % compared to standard n-layers by an enhanced EQE in the wavelength range of 550 - 750 nm [49, 53]. However, the main reason for the improvement cited in this paper is the reduction in absorption losses due to the suppression of surface plasmon polaritons at the silver metal contact [54].

The reduction in loss is not the only way n-µc-$Si_{1\text{-}X}O_X$:H can be used at the back contact to improve the performance. To increase the reflection of light into the cell, a periodic or aperiodic dielectric mirror can be fabricated using n-µc-$Si_{1\text{-}X}O_X$:H and highly hydrogen-diluted n-type a-SiO_X:H [55]. A dielectric mirror uses constructive interference of the periodically reflected waves to create a mirror. The mirror works only for wavelength close to four times the optical thickness of the layers and is therefore of relative narrow bandwidth.

The development of n-µc-$Si_{1\text{-}X}O_X$:H as a window layer for bifacial hydrogenated microcrystalline silicon (µc-Si:H) single junction cells was also presented [56]. Up to now, there has been no publication on n-µc-$Si_{1\text{-}X}O_X$:H as a window layer for bifacial tandem cells. The layer has different requirements compared to the results presented in this section because of the different band gap and surface morphology the n-µc-$Si_{1\text{-}X}O_X$:H layer has to grow on.

There have been no reports on metastability issues with n-µc-$Si_{1-X}O_X$:H layers up to this date. Therefore, the goal of this thesis is to fill that gap in research.

3.1.2 Experimental and Theoretical Background

The idea of n-µc-$Si_{1-X}O_X$:H is to fabricate a two phase material: Crystalline silicon filaments embedded in an amorphous matrix of silicon oxide [57]. The crystalline phase is mainly responsible for charge carrier transport with minimal losses, while the silicon oxide is transmitting photons with almost no impediment.

The material is only conducting well in the vertical direction because of the needle-like crystallites. In the lateral direction, the conductivity is very poor due to the silicon oxide. This anisotropy in conductivity has the benefit of reducing the negative effects of shunts and other local defects [58]. The bad lateral conductivity of n-µc-$Si_{1-X}O_X$:H reduces the negative effect of local unwanted electrical connections between front contact and back contact by reducing the travel distance in lateral direction charge carriers can move to recombine at a shunt [58].

The BR structure works very well when deposited on flat substrates. Since the before mentioned light trapping requires a textured TCO as front contact, the propagated roughness shown in figure 3.1 decreases the the reflectivity of the stack by the excitation of surface plasmon polaritons (SPP) at the interface between silver and ZnO:Al [59]. Some peaks of SPP absorption are located at 400 nm with an absorption tail reaching to the 1000 nm wavelength regime [54]. Since the main absorption range of thin film silicon solar cells is between 300 and 1100 nm, this is a loss that needs to be mitigated by the µc-SiO:H layer.

The n-µc-$Si_{1-X}O_X$:H layers are deposited on the Leybold Phoebous Lab Coater, a small size industrial deposition tool for 50 x 50 cm substrate size. To alloy µc-Si:H with oxygen, carbon dioxide (CO_2) is added to the deposition gas during the fabrication of the layer. This also adds carbon to the composition of the layer. Carbon in form of CH_4 is commonly used to increase the transparency of p-type window layers [60], therefore no adverse effect in addition to the increasing energy gap and reduced conductivity [7: pp. 312] of carbon in the n-type layers is expected.

A difficulty when depositing n-µc-$Si_{1-X}O_X$:H layers was discovered during processing. As the substrates are moved within the deposition tool using aluminum carriers, the carrier itself is covered with a n-µc-$Si_{1-X}O_X$:H layer as well. When the next deposition takes place in a chamber without oxygen, a portion of that silicon oxide is removed

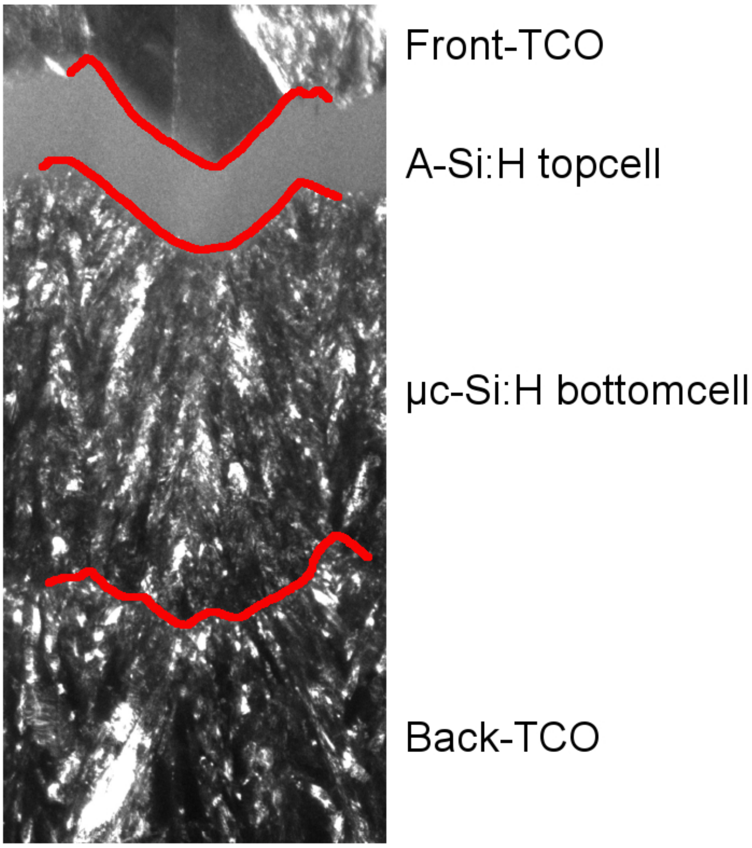

Figure 3.1: Cross section transmission electron microscope picture of a tandem thin film silicon solar cell showing the roughness propagation caused by a crystallite in the front ZnO:Al. The red lines indicate the interfaces.

from the carrier by the deposition plasma and redeposited on the substrate contaminating the layer with oxygen. To circumvent this effect, the carrier is coated with a neutral layer after every oxygen deposition. The same effect can be observed for the chamber walls. The oxygen accumulated on the chamber walls and has to be covered with amorphous silicon when a layer not containing oxygen is deposited.

In order to develop a suitable material with the before mentioned phase separation into amorphous and crystalline material, single layers and cell stacks on glass were deposited. Raman crystallinity and coplanar conductivity can be identified as key parameters for the layer.

The raman crystallinity is measured on the on the single layers using the setup described in section 2.3.5 and the 488 nm laser for shallow information depths because the single layer thickness iss only 70 nm. The single layer depositions are used to find a n-µc-$Si_{1\text{-}X}O_X$:H with enough crystallinity and to determine the deposition rate for the different deposition conditions. The transfer of insight gained with the single layer n-µc-$Si_{1\text{-}X}O_X$:H films to a n-µc-$Si_{1\text{-}X}O_X$:H layer in the device has to be done with great care because the crystallinity is very dependent on the surface morphology of the material it is deposited on [61]. Most steps in the development of the n-µc-$Si_{1\text{-}X}O_X$:H layers have to be performed in the cell stack for that reason. Raman measurements are also performed on the final cell stacks besides electrical measurements.

Publications displaying the planar conductivity found resistances for single layers that should not have been suitable for application in solar cells [62] but worked once incorporated in cell stacks. They attribute this contradiction to the differences in crystallinity caused by different substrates for single layers and cell stacks the n-µc-$Si_{1\text{-}X}O_X$:H layers grow on.

The coplanar conductivity is very difficult to measure in single layer configuration. The layer is therefore attached to the last layer of a very thin ($d < 1$ µm) tandem device. The series resistance of the device in comparison to the series resistance of the device without the n-µc-$Si_{1\text{-}X}O_X$:H layer should reflect the coplanar conductivity of the n-µc-$Si_{1\text{-}X}O_X$:H layers.

3.2 Results and Discussion

3.2.1 Phosphine Doped µc-SiO:H Layers for Thin Tandem Cells

In order to develop a n-µc-$Si_{1\text{-}X}O_X$:H material suitable for BIPV tandem cells, different flows of CO_2 and process pressures are tested for their raman crystallinity for a set of 100 nm thick n-µc-$Si_{1\text{-}X}O_X$:H single layers on float glass.

Figure 3.2 a) depicts the relation between process pressure and the raman crystallinity of the material for single layers. The raman crystallinity shows a sharp increase at pressures between 5 and 6 mbar and reaches a plateau. This is contrary to other publications [48] which show a decrease in raman crystallinity with increasing pressure. For µc-Si:H the increase of raman crystallinity with increasing pressure is well documented [63]. This increase in raman crystallinity can be explained with a favorable regime at higher pressure for the formation of crystalline material. The achieved raman crystallinity of 16 % is too low to indicate the two phase material described above. At 16 % only small sphere-shaped crystalline particles have been formed [57]. In order to reach a crystalline silicon material with particle sizes suitable for the intended purpose, the raman crystallinity should be above 25 % [57]. In pursuance to test

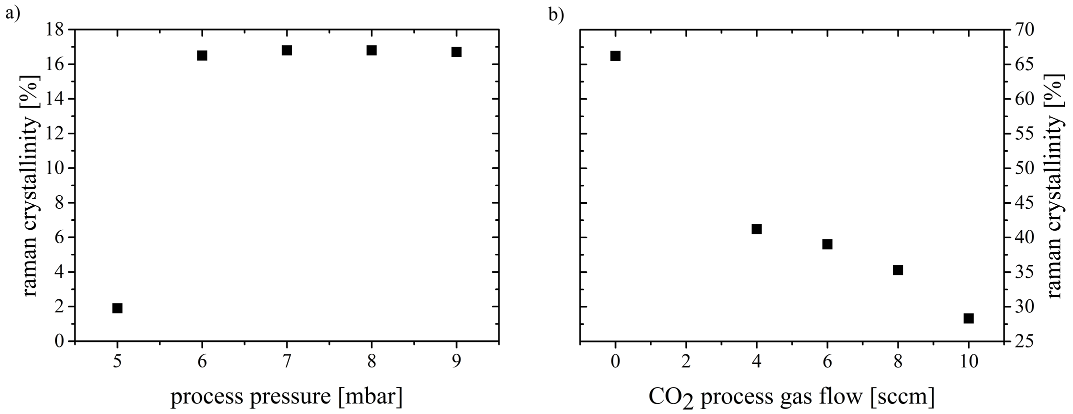

Figure 3.2: Raman crystallinity in relation to the process pressure and CO_2 flow for single layers measured with the 488 nm laser source.

the impact of adding CO_2 to the deposition gas mixture on the raman crystallinity, a crystalline layer with raman crystallinity of 67 % is alloyed with 4, 6, 8, and 10 sccm CO_2 gas during processing. The results are depicted in figure 3.2 b). The addition of carbon and oxygen to the crystalline material reduces the raman crystallinity. This behavior is expected because a reduction in crystallinity caused by oxygen contamination already has been shown for µc-Si:H depositions with leaking vacuum chambers [64].

The physics behind that phenomenon can be explained as follows: A silicon-silicon bond has an average distance of 0.235 nm [65]. In a crystal, there is no deviation from that distance in the lattice. When oxygen has to be incorporated into the lattice, the structure has to change above a certain amount of oxygen because the bond length between silicon and oxygen is only 0.162 nm in average [65]. The shorter bond length disturbs the even lattice structure, forcing the structure to become more amorphous to cope with the different bond lengths in the structure [65].

In conclusion: To get a decent crystallinity for the n-µc-$Si_{1-x}O_x$:H, the starting point has to be very crystalline in order to be able to incorporate a lot of oxygen for the transparency of the layer without loosing the crystallinity completely. This is in good accordance to work published on µc-SiO:H by other groups [53, 66]. The process pressure variation of the n-µc-$Si_{1-x}O_x$:H layer depicted in figure 3.2 a) is repeated in the cell stack to quantify the additional series resistance caused by the n-µc-$Si_{1-x}O_x$:H layer. The series resistances and cell efficiencies are shown in figure 3.3. The series resistance starts at high values of 270 Ω and drops to 14 Ω at 9 mbar process pressure

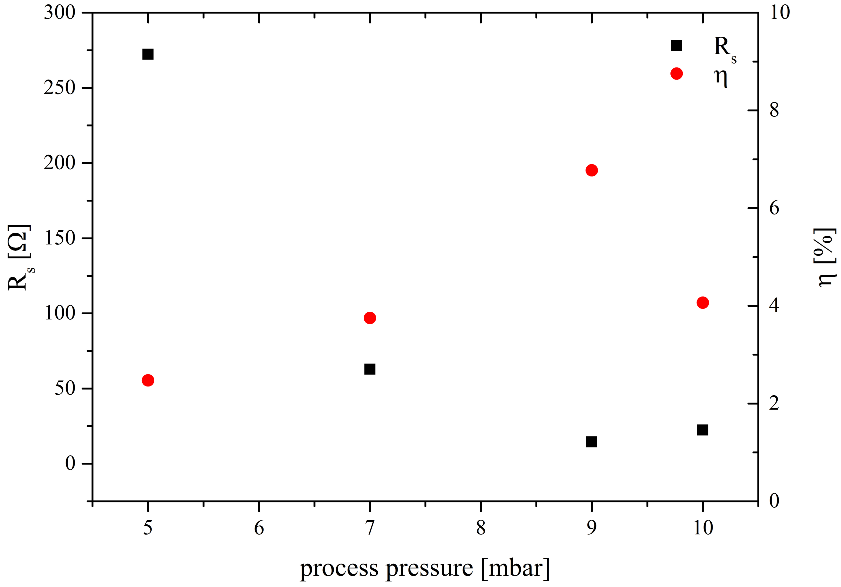

Figure 3.3: Cell stack series resistance equivalent (as described in section 2.3.1) and tandem cell efficiency in relation to the process pressure of the n-µc-$Si_{1\text{-}X}O_X$:H layer.

before raising again at 10 mbar. The process pressure plays a crucial role in reaching device grade micro-crystalline material, high pressure is needed to get a compact, void-poor material [67].

The efficiency is very low for series resistance values above 20 Ω because the FF is directly affected (see section 2.3.1). For the cell with 270 Ω for example, the FF value is only 28 %. The efficiency value for 7 mbar and 10 mbar is almost the same although the series resistance value is 3 times smaller for 10 mbar compared to 7 mbar. This fact can be explained by the very low parallel resistance for the 10 mbar sample reducing the FF value to the same quality of the 7 mbar sample. Measuring the sheet resistance of both samples with the four point needle method [68], an order of magnitude lower value for the 10 mbar sample is also measured. This can be explained by crystalline grains growing to a size at which the before mentioned phase separation in the material is not present any more. Also, the removal of internal silicon dioxide barriers hindering the in-plane conductivity can be the reason for the low parallel resistance. Other researchers found a similar behavior in their studies [45]. 9 mbar process pressure is chosen for all further n-µc-$Si_{1\text{-}X}O_X$:H layers on the basis of this experiment.

Distance:	Pressure:	Power:	SiH$_4$ Flow:	CO$_2$ Flow:	H$_2$ Flow:	PH$_3$ Flow:
10 mm	9 mbar	250 W	7 sccm	17.5 sccm	1540 sccm	23 sccm

Table 3.1: Final deposition parameters for the n-µc-Si$_{1\text{-}X}$O$_X$:H layer for the Leybold Phoebus Lab Coater.

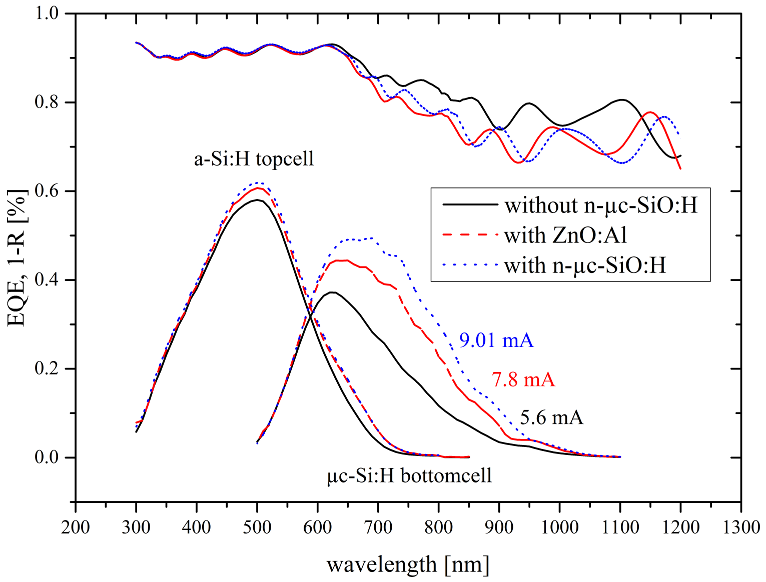

Figure 3.4: External quantum efficiency and reflectance measurements of different back layer stacks on tandem cells in comparison.

The variation of CO$_2$ flow and initial crystallinity is continued until a material with suitable properties of series resistance below 15 Ω and raman crystallinity around 35 % is found. The final deposition parameters for the n-µc-Si$_{1\text{-}X}$O$_X$:H layers can be found in table 3.1. Tandem cells without n-µc-Si$_{1\text{-}X}$O$_X$:H, with the n-µc-Si$_{1\text{-}X}$O$_X$:H layer and with a ZnO:Al layer with the same optical thickness are prepared in order to gauge the effectiveness of the n-µc-Si$_{1\text{-}X}$O$_X$:H layer.

The results are depicted in figure 3.4. The current density generated by the amorphous top cells is almost equal for all three setups and only 10 % of the light is reflected from the cells in the 300 to 600 nm wavelength regime. The area between the 1-R curve and the EQE curve is equal to the amount of light lost to internal processes. For the 300 to 450 nm wavelength regime, the main loss of light is caused by parasitic

Back Layer	$J_{sc}\left[\mathrm{mA/cm^2}\right]$	V_{oc}[mV]	FF[%]	η[%]
None	9.6	1402	71	9.6
n-μc-SiO:H	10.1	1427	71	10.2

Table 3.2: Comparison of top performance electrical values for tandem thin-film solar cells with and without n-μc-$Si_{1\text{-}X}O_X$:H back layer.

absorption in the doped p-layer [69]. Transparent p-layers using the same benefits of the μc-SiO:H mentioned above were developed for that reason [44].

The reflectance of the cells with back layer is very different from the reflectance of the cell without back layer for the wavelength regime between 600 and 1200 nm. The cell without back layer reflects far less light in the long wavelength regime without generating more current density. The loss mechanism is the before mentioned SPP generation at the silver interface caused by the propagated roughness shown in figure 3.1.

The reflectance of the cells with back layer is almost equal. Only a small shift of the reflectance peaks between the two cells with back layer can be discerned. This shift is caused by a small difference in optical thickness between the two back reflectors.

The reduction of internal loss is clearly visible by the improved current generation behavior of the bottom cell while the reflection of light with long wavelengths is also increased. This is caused by more light passing in and out of the cell without being absorbed by SPP for example.

The current generation density of both tandem cells with back layers is greatly improved. Figure 3.4 shows the current generation density calculated from the EQE curve for the bottom absorber. The cell with ZnO:Al back layer is superior to the cell without back layer and is surpassed by the cell with n-μc-$Si_{1\text{-}X}O_X$:H back layer. These findings are in good accordance to recent publications [70] where they compared ZnO:Al back layers with n-μc-$Si_{1\text{-}X}O_X$:H and MnF_2 back layers and found similar EQE results. Electrical characterizations are performed in addition to the EQE measurements. The results are displayed in table 3.2. An increase in J_{sc} and V_{oc} is visible for the cell with n-μc-$Si_{1\text{-}X}O_X$:H back layer while the FF is the same value for both configurations. The benefits of using a n-μc-$Si_{1\text{-}X}O_X$:H back layer are confirmed by the electrical characterizations although the difference in current generation density in table 3.2 is not as pronounced as in the EQE measurements in figure 3.4.

The thickness of n-μc-$Si_{1\text{-}X}O_X$:H used as back layer is different for almost every pub-

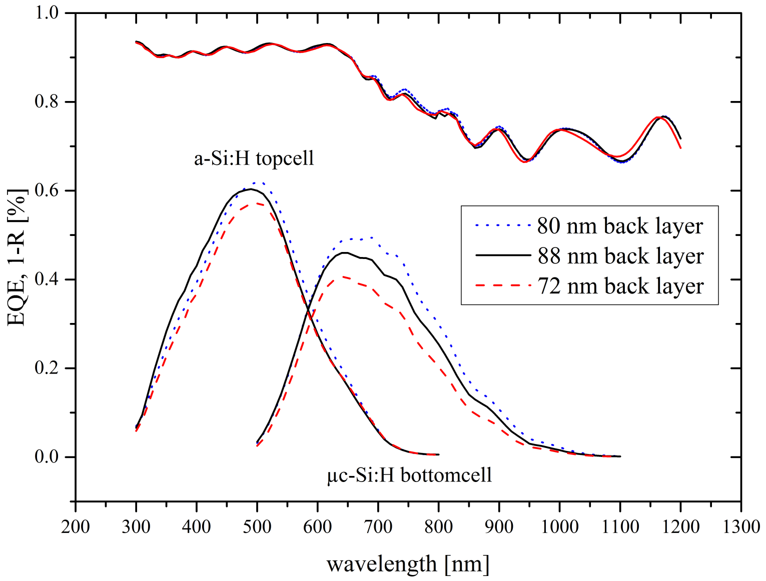

Figure 3.5: External quantum efficiency and reflectance measurements of back layer stacks with different thicknesses on tandem cells in comparison.

lication: In [70] a 30 nm thick layer is used, in [56] they used 20 nm and in [71] they used a 60 nm thick layer. First experiments result in a maximum in EQE values for 80 nm back layer thickness. Figure 3.5 shows the EQE and reflection for three different thicknesses of n-µc-$Si_{1-X}O_X$:H back layers. The reflection of the cells does not change significantly over the whole wavelength range. The EQE of the amorphous top cell absorber varies only slightly as well. The current generation density is largest for the back layer with 80 nm thickness followed by the 88 nm thick layer and smallest for the 72 nm thick back layer. Why is there an optimum in thickness? The SPP suppression at the last interface should not take such a thick layer. The answer is constructive interference: The phase shift of long wavelengths bounces light back into the bottom absorber, giving it another chance of being absorbed. This effect is highly dependent on the optical thickness.

The thickness of the n-µc-$Si_{1-X}O_X$:H layer is very different from the optimal thicknesses presented in the publications above. Because n-µc-$Si_{1-X}O_X$:H is a material that can be fabricated with different n- and k-values [44] it is very probable that the material is similar in function, but cannot be compared directly to the material in the publications in terms of optical thickness.

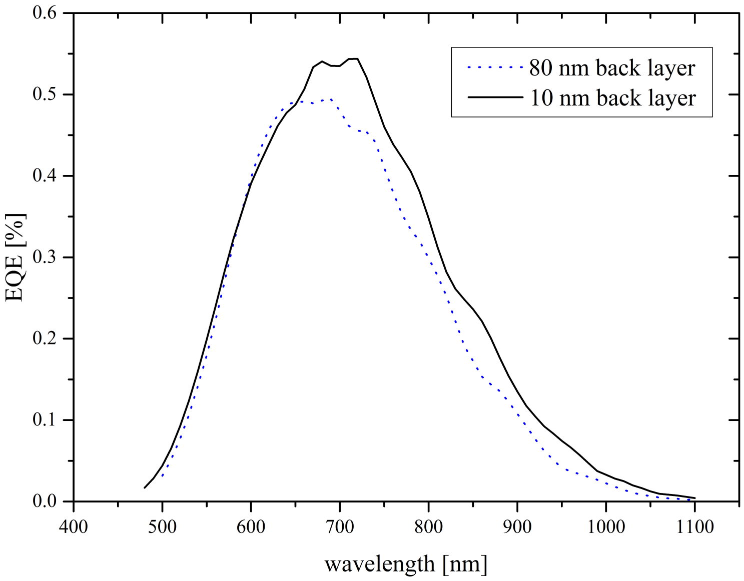

Figure 3.6: External quantum efficiency measurements of back reflector stacks with 80 nm and 10 nm on tandem cells in comparison.

In order to use the n-µc-Si$_{1\text{-}X}$O$_X$:H as a blue light transparent n-layer, the thickness has to be reduced from the 80 nm. This results in a good transparency and thereby reduced parasitic absorption in the n-layer. As can be seen in figure 3.6, the 10 nm thick n-µc-Si$_{1\text{-}X}$O$_X$:H back layer has an even better EQE performance than the 80 nm thick one. The 10 nm back layer has less parasitic absorption which overcompensates the optimization of the 80 nm thick back layer for interference reflection.

3.2.2 Metastability of Phosphine Doped Microcrystalline Silicon Oxide Layers

Detailed measurements revealed a metastable crystallinity of the bottom µc-Si:H absorber for approximately every 10 depositions: First measurements at the day of deposition and the day after sometimes resulted in measurements of bottom absorbers with bad current generation density for some tandem cells. Although the cells were tempered at 160 °C for 30 minutes directly after the back contact deposition, storage of the tandem cells exposed to air in the dark for three days cured the bad perform-

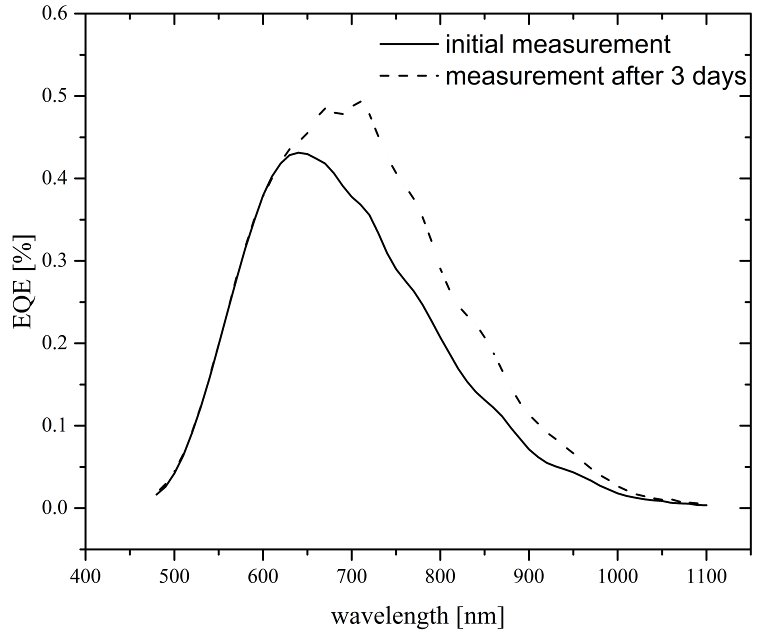

Figure 3.7: External quantum efficiency measurements of a metastable microcrystalline bottom absorber directly after deposition and after three days of dark storage on air.

ance of the bottom absorbers. The effect can be seen in figure 3.7 and the electrical measurements in table 3.3.

The EQE rises significantly after three days of storage. This is true for the µc-Si:H absorber in figure 3.4 as well. While the difference after the settling of the bottom absorber material might not be as great as before, it is still visible and confirms the data in table 3.2. The reason for the change in electrical performance and EQE can be found in the crystallinity: The raman crystallinity for the bad tandem cells is only at 32 % directly after deposition and reaches the 56 % raman crystallinity all other cells displayed after a few days.

An extensive search of literature revealed no publications relating to metastable crystallinity phases of µc-Si:H material not connected to external energy input via light. Since the change happened during storage in darkness, this is not the case here. Because a crystal is a state with lower overall system energy, it is theoretically possible that a chemical reaction with only room temperature as energy input leads to a crystallization of the µc-Si:H material.

State	$J_{sc}\left[mA/cm^2\right]$	$V_{oc}[mV]$	FF[%]	η[%]
after deposition	8.3	1383	71	8.2
3 days storage	10.1	1404	69	9.8

Table 3.3: Comparison of tandem solar cells directly after deposition and after 3 days of dark storage on air.

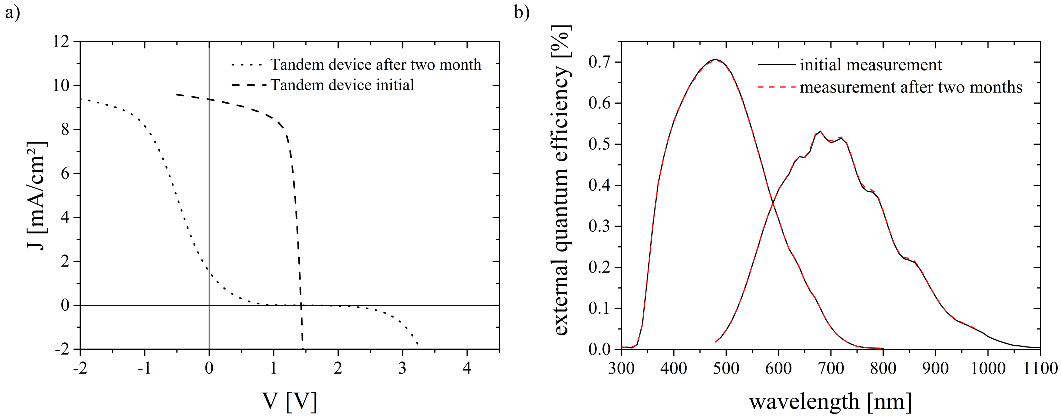

Figure 3.8: a): J-V curve of a tandem cell with n-μc-$Si_{1-X}O_X$:H back layer directly after deposition and after two months of storage in the dark on air. b): External quantum efficiency measurement of the same tandem cells directly after deposition and after two months storage in the dark on air.

This effect can be avoided completely by the use of a high-energy plasma on the back surface of the μc-Si:H absorber deposition. The cells with n-μc-$Si_{1-X}O_X$:H back layer do not show this particular metastability effect at all because of the long and with 100 mW/cm^2 very energy intensive n-μc-$Si_{1-X}O_X$:H deposition. While measuring the J-V curves of old tandem cells with n-μc-SiO:H back layers that were stored on atmosphere in the dark, an interesting discovery could be made: The performance of those cells degrades to a point where almost no power generation of the cells could be measured (see figure 3.8 a)). The measurement shows a very pronounced reversal diode which can be caused by increased series resistance originating in non-conductive barriers [72].

EQE measurements of the same cells show the same performance for both measurement times (figure 3.8 b)) without any sign of performance loss. Since the EQE measurements were performed at nearly J_{sc} conditions with almost no current flowing, this gives additional merit to the theory of a non conductive barrier. Other sources like the degradation of the contacts or aging of the TCO can be ruled out because in

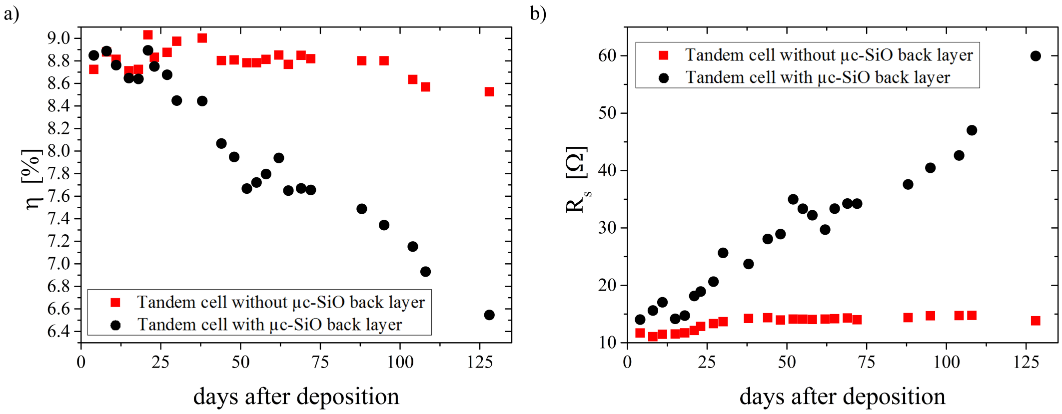

Figure 3.9: a): Tandem cell efficiency values and b): Tandem cell series resistance equivalent (as described in section 2.3.1) of a tandem cell with and without back layer in comparison related to the time after deposition.

that case, the EQE performance would have dropped as well.

Although other researchers tested n-µc-$Si_{1-x}O_x$:H layers for light induced degradation [66], no reference to metastability issues related to µc-$Si_{1-x}O_x$:H layers can be found in the literature.

A long term test with frequent J-V measurements following the deposition is performed on tandem cells with and without n-µc-SiO:H back layers to rule out a general degradation of tandem cells caused by their storage conditions. The deposition recipe and all further processing steps are the same for both cells except the addition of the n-µc-SiO:H back layer on one of the tandem cells on top of the amorphous n-layer on the back of the cell stack. The resulting performance development is plotted against the time after deposition in days in figure 3.9.

Though the efficiency of the tandem device with the n-µc-SiO:H back layer starts out higher than the efficiency of its counterpart without back layer (figure 3.9 a)) it drops below the efficiency of the cell without back layer after approximately 10 days and seems to drop almost linear with time loosing 20 % of the efficiency in 100 days. The reduction in efficiency is not caused by a reduction of V_{oc} or J_{sc} but by a reduction of FF caused by an almost linear increase in series resistance depicted in figure 3.9 b). While the series resistance of the tandem cell without n-µc-SiO:H back layer remains at a value between 10 and 15 Ω, the series resistance of the cell with n-µc-SiO:H back layer increases almost linear and reaches three times its initial value after 100 days of dark storage on air.

Both tandem cells are identical. The addition of the n-µc-SiO:H back layer adds two new interfaces: The amorphous n-layer to n-µc-SiO:H interface and the n-µc-SiO:H to silver interface. Silver is known to diffuse into silicon [73]. Since the diffusion in the amorphous n-layer and the microcrystalline absorber does not influence the performance of the tandem cell without n-µc-SiO:H back layer, only the diffusion of silver into the n-µc-SiO:H back layer could be a reason for the degradation in addition to changes in the bulk or interfaces of the n-µc-SiO:H back layer.

To rule out water vapor diffusion into the possibly very porous n-µc-SiO:H back layer, cells with a back contact completely covered with 100 nm silver and a 60 nm TCO water vapor protection layer are fabricated and measured. Laser scribing is used to define the 1 cm^2 test cell surfaces. In terms of degradation, no significant difference to cells not covered in this way can be found. Although water vapor could possibly still ingress through the laser scribes, this is unlikely to be the case, because the degradation does not change significantly in spite of the far smaller ingress area of the laser scribe. Other researchers found a slight degradation of very porous µc-Si:H when stored on air over two years [74]. They found that the degradation is dependent on the buffer layer and was caused by oxidation of the surfaces inside the pores of the crystalline material. This effect is also checked with the silver and TCO experiment because the degradation in [74] only happens when the µc-Si:H layer is directly exposed to air.

In hydrogenated amorphous silicon, incident photons of sufficient energy can cause bonds between hydrogen and silicon to split, forming an open dangling bond and increasing the defect density of the material to increase. This effect is reversible by increasing the material temperature enough to enable the bond between the hydrogen and silicon to reform. The effect is called Steabler-Wronski effect [13]. The following experiment is conducted in order to determine the relation between the degradation of the tandem cells in storage with the Steabler-Wronski effect.

The cells measured in the previous experiment (figure 3.9) were subjected to 1000 hours of light soaking (see section 2.3.4) after the measurements had been performed for that figure. The tandem cell without n-µc-SiO:H back layer shows the 10 % degradation in efficiency expected for thin film solar cells utilizing a-Si:H [13] (see figure 3.10 a)) and seems to reach a saturation at 600 to 800 hours of light soaking before seeming to degrade further at 1280 hours of light soaking. The continuation of degradation after reaching saturation can be attributed to a discoloration of the silver contacts on this particular cell. The series resistance equivalent (see figure 3.10 b)) of this cell rises by 5 Ω but stays nearly constant after that.

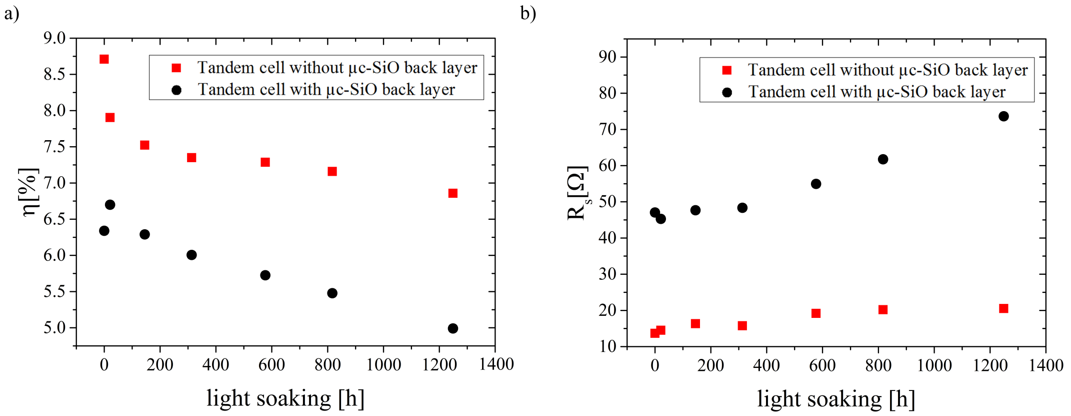

Figure 3.10: a): Tandem cell efficiency values and b): Tandem cell series resistance equivalent (as described in section 2.3.1) of a tandem cell with and without back layer in comparison during light induced degradation.

Annealing	$J_{sc}\left[mA/cm^2\right]$	$V_{oc}[mV]$	FF[%]	η[%]
0 minutes at 160 °C	5.8	1467	11	0.9
10 minutes at 160 °C	8.5	1440	25	3.1
30 minutes at 160 °C	8.4	1436	23	2.8
70 minutes at 160 °C	8.4	1438	22	2.6
20 minutes at 200 °C	7.9	1400	19	2.1

Table 3.4: Progression of electrical values for tandem thin-film solar cells with n-μc-SiO:H back layer after degradation in relation to annealing time at 160 °C.

The degradation is very pronounced in the first 100 hours of light soaking for the cell without n-μc-SiO:H back layer and almost all degradation takes place in that time interval. In contrast, the degradation for the cell with n-μc-SiO:H back layer is approximately linear over the whole time interval and even shows a small improvement after the first 10 hours of light soaking (see figure 3.10 a)). The improvement coincides with a small improvement of the series resistance equivalent while the degradation can be matched with an almost linear increase in series resistance (see figure 3.10 b)). Contrary to the rapid degradation of the sample without n-μc-SiO:H back layer, some self-healing due to the energy introduced by the irradiation takes place in the degraded sample with n-μc-SiO:H back layer before the effect of Staebler-Wronski degradation becomes larger than the self-healing effect. The Steabler-Wronski effect

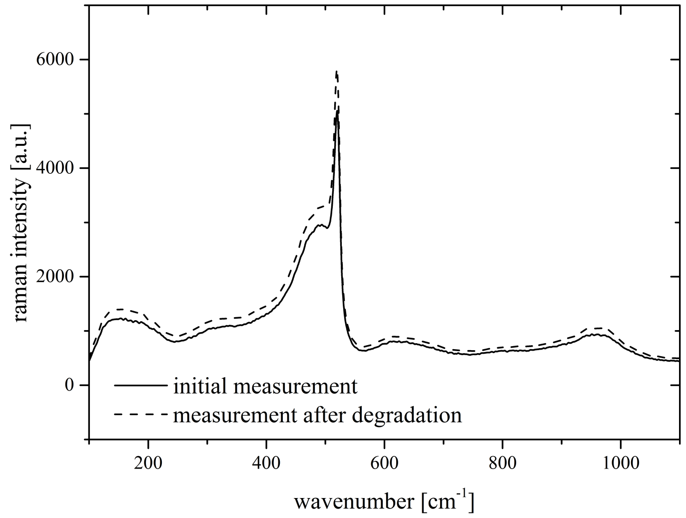

Figure 3.11: Raman measurement of a n-µc-SiO:H back layer on the back of a tandem device before and after degradation with 488 nm laser light.

can be reversed by annealing the degraded cells [13]. In order to check the metastability of the n-µc-SiO:H back layer for reversal by annealing, a tandem cell with n-µc-SiO:H back layer is stored in the dark on air for five months and then annealed at 160 °C. The results are displayed in table 3.4.

The degradation is not completely reversible by annealing. The FF of the cell improves after the first annealing to more then double its value but degrades again for each successive annealing. The results match the relation to the series resistance equivalence seen in figure 3.9 and 3.10. The degradation effect seems to only influence one value of the electrical performance, J_{sc} and V_{oc} are only indirectly influenced by the shift in the J-V curve enforcing the argument for a non-conductive barrier forming.

Raman measurements are performed on tandem cell n-µc-SiO:H back layers before and after degradation in order to determine differences in the atomic binding structure. The 488 nm laser source is chosen to use the shallow information depths of approximately 30 nm (see section 2.3.5) to get a signal dominated by the n-µc-SiO:H back layer. The results are depicted in figure 3.11. Although the intensity changes a little bit between measurements, no changes in material composition can be detected from the raman measurements. The raman crystallinity is at 50 % for both samples. Raman measurements display the symmetric vibrations of a molecule and not the

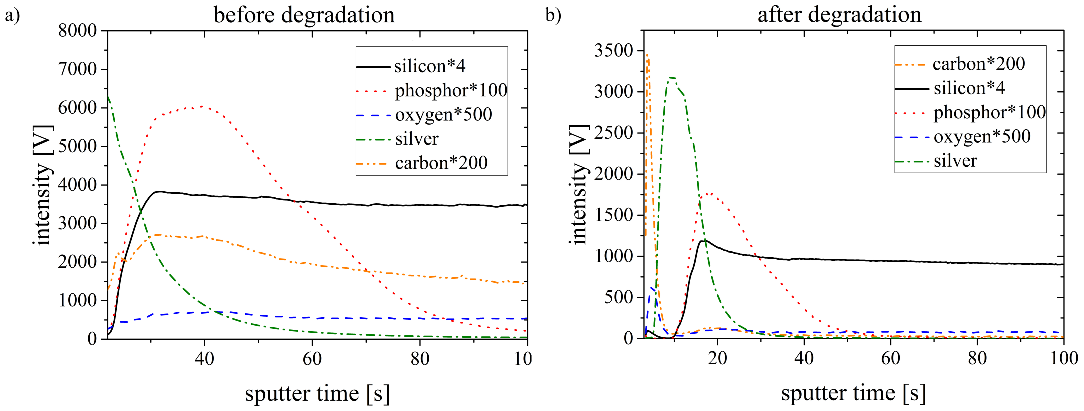

Figure 3.12: Glow discharge measurement of a n-µc-SiO:H back layer on the back of a tandem device a) before and b) after degradation. Signal magnification is indicated in the graph. Measurements for this graph were performed by Dr. Beatriz Fernandez at the University of Oviedo in Spain.

asymmetric ones because of the conservation of spin in the initial state. Fourier transform infrared spectroscopy (FTIR) can be performed to display the asymmetric vibrations of molecules in a sample. It is not possible to perform FTIR measurements because the TCO layer is not transparent for infrared light and the single layer back reflectors were not of the same material (see page 22).

Figure 3.12 shows the rf-GD-ToFMS measurement of a tandem device on a flat substrate with a n-µc-SiO:H back layer. The first layer to be sputtered is the 300 nm thick silver reflector at 0 s sputter time. Total intensity varies for both measurements but can be referenced to the silicon intensity.

The main component of the n-µc-SiO:H back layer is silicon, which indicates the beginning of the layer with a steep increase in intensity. The steepness of the signal is an indication of the roughness of the layer caused by the crystalline silicon absorber layer underneath. The silver signal does not decline with the same steepness as the silicon signal increases indicating silver ingress into the material which is a process that has already been documented [75].

The phosphor intensity follows the silicon signal with its steep increase and slowly decays when the transition to the microcrystalline absorber starts. The silicon and phosphor intensity shows no relative intensity change between initial and degraded state.

The oxygen signal is very small and does not change significantly as well. Only its intensity relative to the silicon intensity is lower in the degraded state. The carbon

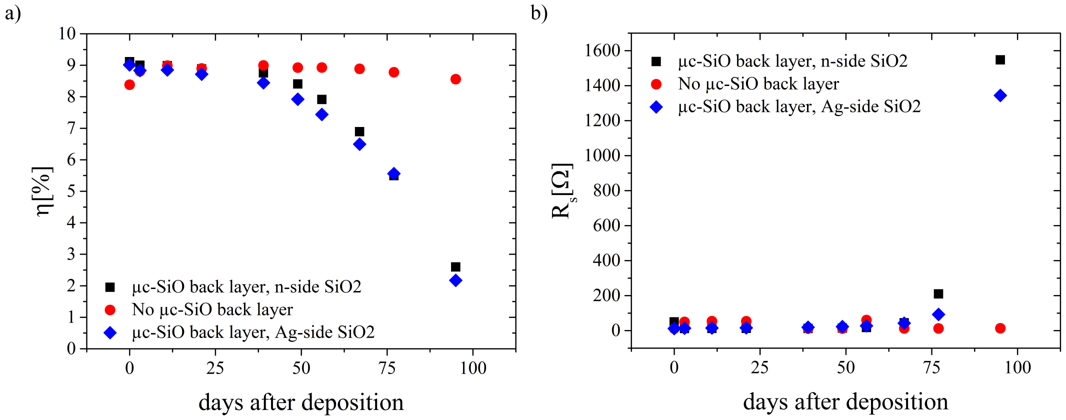

Figure 3.13: a): Tandem cell efficiency values and b): Tandem cell series resistance equivalent (as described in section 2.3.1) of a tandem cell without n-μc-SiO:H back layer in comparison to a tandem cell with n-μc-SiO:H back layer and SiO_2 buffer layer at the n-layer and Ag-layer interface in relation to the time after deposition.

content of the n-μc-SiO:H back layer in the degraded state is far lower than in the initial state. The intensity of the carbon signal is more than four times lower in comparison to the silicon signal in the degraded state compared to the initial state. When looking closely at the carbon signal in the initial state, an indication of carbon moving out of the n-μc-SiO:H back layer can be seen: There is a concentration peak of carbon at the silver layer interface before the silicon signal begins. Very thin glass layers of silicon dioxide (SiO_2) can be used to reduce the diffusion of dopants from one layer to the other [76, 77]. SiO_2 can increase the series resistance of a cell stack because undoped SiO_2 is not conductive. The thickness of the added SiO_2 layer has to be thin enough to be tunneled through by charge carriers without posing a significant hindrance. The critical thickness is determined to be below 5 nm, which is in good accordance to literature [78, 79].

5 nm thick SiO_2 layers are inserted before and after the BR into the cell stack in order to determine the direction of the carbon diffusion. The results are displayed in figure 3.13. The starting efficiency in figure 3.13 a) of the tandem cell without n-μc-SiO:H back layer is lower than the efficiency of the tandem cells with n-μc-SiO:H back layer but seems to improve with the next measurement. This could be caused by the μc-Si:H metastability described on page 29.

The efficiency of the cells with n-μc-SiO:H back layer drops significantly after a period of approximately 30 days. There is no great difference for the position of the SiO_2 layer although the tandem cell with the SiO_2 layer at the silver side degrades a little

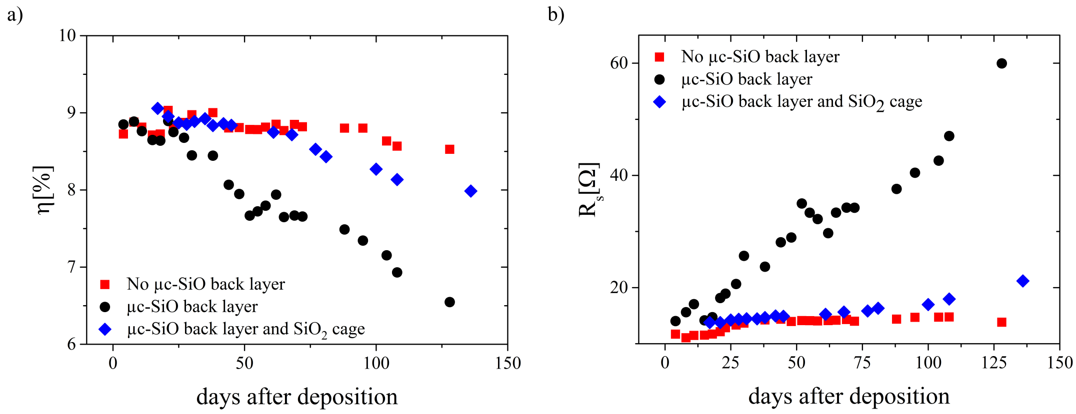

Figure 3.14: a): Tandem cell efficiency values and b): Tandem cell series resistance equivalent (as described in section 2.3.1) of a tandem cell without n-µc-SiO:H back layer in comparison to a tandem cell with n-µc-SiO:H back layer and a tandem cell with n-µc-SiO:H back layer and SiO_2 buffer layer at both interfaces in relation to the time after deposition.

faster. The series resistance equivalent displayed in figure 3.13 b) follows the same trend as in figure 3.9 b). The difference between the results in those figures being that the maximum value for the series resistance is an order of magnitude higher for the cells with SiO_2 layer. The cause for this steeper decline of the cells with SiO_2 layer is probably the greater healing effect of light and heat for the cells in figure 3.9 caused by more measurements of the cells. A tandem cell with n-µc-SiO:H back layer and SiO_2 buffer layer at both interfaces is fabricated in order to examine the possibility to stop the diffusion of carbon completely. The results are depicted in figure 3.14.

The efficiency values in figure 3.14 a) show a decay of the the tandem cells with SiO_2 layer cage compared to the tandem cell without n-µc-SiO:H back layer. In comparison to the cell with n-µc-SiO:H back layer but without SiO_2 cage the cell shows a far better performance and a decay of only 10 %.

This is mirrored in the series resistance equivalent values displayed in figure 3.14 b). The increase in series resistance for the cell with n-µc-SiO:H back layer and SiO_2 cage is far lower than the increase for the cell without SiO_2 cage and only a little higher than the reference tandem cell without oxide layers.

A SiO_2 cage is therefore a viable method to reduce the diffusion of carbon out of the n-µc-SiO:H back layer and the thereby caused degradation. The stability of the layer is improved by the application of the a SiO_2 buffer layers but needs further work to reach the same stability as the tandem cell without n-µc-SiO:H back layer.

3.3 Conclusion

This chapter demonstrated the performance enhancement of n-µc-SiO:H back layers. While the majority of the layers was used to suppress SPP at the interface to the silver reflector, a 10 nm thin n-µc-SiO:H back layer was developed that outperformed in terms of EQE.

This layer is an excellent candidate to improve thin-film silicon solar cells for the use in BIPV applications like bifacial facades. The development of a material with two different phases for two distinct tasks is a clear advantage of this material. The crystalline phase takes care of the charge carrier conductivity while the silicon oxide phase increases the transparency greatly.

In order to achieve the longevity of thin-film solar modules guaranteed by the manufacturers, new films have to be tested for their stability. A degradation of the n-µc-SiO:H layer was found for dark storage. A diffusion of carbon out of the n-µc-SiO:H layer was identified as cause for the formation of a barrier increasing the series resistance of the cell over time. This process was found to be irreversible by heat and light treatment. The carbon originates from the CO_2 gas that was used to add oxygen to the layer.

By inserting two SiO_2 buffer layers at both interfaces to the new n-µc-SiO:H layer, the degradation effect could be reduced effectively. A slight performance drop remains visible with the combination of n-µc-SiO:H and SiO_2 buffer layer. Therefore, further research is necessary to eliminate the degradation of the new layer completely.

The advantages of using n-µc-$Si_{1\text{-}X}O_X$:H as a doped layer in BIPV are a decrease in layer thickness and parasitic absorption. This results in lower LCOE because it increases the efficiency of the module. An enhanced backside transparency improves the bifaciality of a module as well. A low absorption on the n-side of the module increases the power generated by scattered light hitting the backside of a bifacial module. The longevity of the cells with n-µc-SiO:H layers can be improved by inserting SiO_2 buffer layers at the interfaces to the layer that hinders the diffusion of carbon out of the layer.

4

μc-SiGe:H as Alternative Absorber Material for BIPV Applications

The previous chapter presented how the use of novel transparent doping layers for BIPV applications can lower the LCOE. This chapter focuses on reducing the absorber thickness and therefore LCOE as well, while maintaining the same efficiency using μc-$Si_{1-X}Ge_X$:H as an alternative absorber material for thin-film silicon solar cells for BIPV applications.

Though there are publications on research about μc-$Si_{1-X}Ge_X$:H absorber layers, there are no comprehensive studies on μc-$Si_{1-X}Ge_X$:H absorbers with low germanium content in the range of 10 %. Therefore, the chapter will start with an overview of current research concerning μc-$Si_{1-X}Ge_X$:H solar cells that is followed by a short outline of the necessary experimental and theoretical background used in the following sections. Experimental deposition conditions are linked to the material properties of μc-$Si_{1-X}Ge_X$:H in order to evaluate the feasibility as absorber material for BIPV applications in single- and tandem-junction BIPV solar cells. The resulting μc-$Si_{1-X}Ge_X$:H absorber material can generate the same amount of charge carriers at a far lower thickness than its μc-Si:H counterpart. A glow discharge optical emission spectroscopy measurements was performed at the University of Oldenburg with the help of Maria Hammer to determine the amount and position of germanium. Results of this chapter are published in [80].

4.1 µc-SiGe:H

4.1.1 Overview

Typical absorber thicknesses of a-Si:H single junction solar cells are 200-400 nm having very low production costs. However, amorphous silicon degrades under illumination which is called the Steabler-Wronski effect [13] or light-induced degradation (LID) limiting the efficiency of single junction a-Si:H solar cells. Laboratory a-Si:H single junction solar cell efficiencies have reached 10.2 % after the typical 10 % LID [81].

To circumvent this effect, a-Si:H is used in tandem configurations as top cell paired with µc-Si:H as bottom cell i-layer material that does not degrade. Typical absorber thicknesses for tandem cell configurations are 200-250 nm for a-Si:H top cells and 900-1200 nm for bottom µc-Si:H bottom cells. For a-Si:H/µc-Si:H tandem cell configurations, stabilized efficiencies exceeding 12 % have already been demonstrated [82].

Because of the low absorption probability for longer wavelength light, the bottom absorber of triple junction solar cells has to be deposited very thick (in excess of 2 µm) resulting in a quite cost intensive industrial application due to corresponding long layer deposition times.

Single junction µc-Si:H cells have reached stable record cell efficiencies of 11.8 %, exceeding the efficiency of the a-Si:H single junction cells [51]. While the efficiency of the µc-Si:H solar cells might be higher than the efficiency of their a-Si:H counterpart, low deposition rates and absorber thicknesses an order of magnitude higher make them more cost intensive for industrial production as well.

There are different approaches to reduce the thickness of the absorber layer. Optimizing light trapping due to scattering structures at the front contact and thereby increasing the path length of light through the device is one of such options; using novel back reflectors at the back interface is another (see chapter 3). A different approach is to substitute conventional doped layers with more transparent oxygenated doped layers where more light reaches the absorber layer and increases the cell current densities enabling a reduced layer thickness [83].

A relatively new approach is to increase the absorption coefficient of the absorber material by alloying silicon with germanium [84]. Germanium is added to the deposition gas mix in form of germane (GeH_4) and increases the light conversion of the absorber alloy by shifting the bandgap to lower energies enabling a significant enhancement in the infrared response of the cells [85].

The mixing of silicon and germanium can be done in either amorphous or microcrystalline form. Though solar cells with hydrogenated amorphous silicon germanium (a-SiGe:H) as absorber material have been reported with high efficiencies [86], many reports claim a larger LID for a-SiGe:H compared to standard a-Si:H absorber cells [87–90].

Matsui et al. introduced the usage of microcrystalline silicon germanium alloys with increased absorption coefficient compared to μc-Si:H [85]. Like μc-Si:H, μc-$Si_{1-X}Ge_X$:H does not suffer from LID. The first mention in a scientific publication of μc-$Si_{1-X}Ge_X$:H can be tracked back to the year 1996 [91] when μc-$Si_{1-X}Ge_X$:H was proposed to be used as a bottom absorber in tandem cell configuration. Most of the scientific work on μc-$Si_{1-X}Ge_X$:H ever since has been published by the same group of scientists in Japan facilitated by Takuya Matsui and Michio Kondo. While the first application of the material was in a schottky-barrier solar cell [92], the first working p-i-n device using a μc-$Si_{1-X}Ge_X$:H absorber was presented a year later in 1998 [93]. A study from a research group in China focused on the 20 % to 40 % germanium content regime [94] studying higher germanium content than this chapter will cover.

4.1.2 Experimental and Theoretical Background

Besides the application in solar cells, extensive research on the material properties and growth mechanisms of μc-$Si_{1-X}Ge_X$:H absorbers have been performed by various researchers. It has been shown that a linear dependency exists between the germanium content in a μc-$Si_{1-X}Ge_X$:H layer and the shift of the absorption coefficient to lower energies [84] because of the before mentioned bandgap shift. The bandgap of crystalline germanium is 0.66 eV for the indirect transition and 0.8 eV for the direct transition [95] while the bandgap for μc-Si:H is at 1.1 eV [96]. Depending on the germanium content, a μc-$Si_{1-X}Ge_X$:H absorber layer will therefore have a bandgap between 0.8 and 1.1 eV.

As mentioned in 2.3.5, the difference in lattice constants between silicon and germanium, with germanium having a 4 % lower lattice constant than silicon, induces stress in the material [19] and can be measured with raman spectroscopy. This is also a method to measure the germanium content in a crystalline silicon layer because the amount of stress in the material is linear in relation to the amount of germanium in the layer for low contents of germanium [19].

The stress caused by the addition of germanium will also cause the material to shift from an initially (without germanium) crystalline state to an amorphous state because the addition of atoms with different bond-lengths will cause disorder in the material.

In a perfect diamond cubic structure, each silicon atom would have four silicon neighbors. With the addition of a germanium atom with a shorter bond-length in such a lattice the germanium atom might only end up with three silicon neighbors and one open bond. This is called a germanium dangling bond. The dangling bond defect can be used by charge carriers to recombine without reaching the contacts and should therefore be avoided if possible. An increase in dangling bond density also reduces the fill factor value of the resulting solar cell [97]. The impact of dangling bond density on V_{oc} values is comparably small, fill factor deterioration due to dangling bonds is rather caused by conductivity modulations that impact the series and parallel resistivity of the cell stack [97].

Depending on the deposition conditions, microcrystalline material can be either compact or porous. A porous material has a lot of inner surfaces and voids where the silicon or germanium atoms have dangling bonds that can be connected to hydrogen or nothing at all. Porous material has the tendency to absorb moisture and oxygen [98] and has a high defect density leading to bad solar cell performance [94]. Therefore, a compact, void free material is preferred for solar cells.

The lower bandgap of the μc-$Si_{1-X}Ge_X$:H absorber compared to the bandgap of a conventional μc-Si:H absorber leads to a significantly enhanced external quantum efficiency for μc-$Si_{1-X}Ge_X$:H layers with x smaller than 0.2 [99]. The reason for the maximum content of germanium of 20 % can be traced to the electrical properties of the alloy. While the optical properties are enhanced by the addition of germanium, hole concentration and and defects (dangling-bonds) induced by germanium in the lattice increase up to five times compared to a μc-Si:H alloy [84, 99, 100].

For a germanium contend above 20 %, an injection dependent charge carrier recombination at the p - i interface can be observed [100, 101]. This leads to a negative space charge and a strong reverse field in the intrinsic layer resulting in a reduced carrier mobility with increasing germanium content [101].

Because of these negative effects, the gain of additional infrared response of the layer are over-negated for germanium concentrations greater than 20 % [102]. Therefore, the following work is restricted to μc-$Si_{1-X}Ge_X$:H alloys with a contend below 12 %.

Being able to shift the bandgap of a material to lower energies has the great benefit of being able to absorb photons with lower energies. However, it lowers the V_{oc} as well [103]. Therefore, the gain in J_{sc} caused by being able to convert photons of longer wavelengths has to surpass the loss in V_{oc} caused by higher thermalization losses by the smaller bandgap.

4.2 Absorber and Deposition Properties of Silicon-Germanium Cells

4.2.1 Crystalline Silicon-Germanium Absorbers

This section will address the challenges in creating an absorber material capable of replacing an absorber in single- or multi-junction thin-film solar cells for BIPV applications. The explicit goal is to use the enhanced absorption of germanium to reduce the thickness and therefore deposition time of the absorber layer while maintaining the generated current density. While replacing silicon absorbers with germanium absorbers was done before [84, 86, 99, 102], no one has tried it with BIPV applications in mind.

To this end, a comprehensive study on the effects process parameters of the intrinsic layer in a single μc-$Si_{1\text{-}X}Ge_X$:H cell have on the material properties is presented. Focus of the material properties is the germanium content and crystallinity while linking them to the electrical device performance. A similar study was published in 2006 by a group in Japan [99], with the key difference being the germanium concentration in the layer. This work focuses on low germanium concentration layers (content below 10 %) while the group in Japan focused on layers with a germanium content of about 20 % [99].

Since the structure and crystallinity is strongly dependent on the substrate surface [7: pp. 105], only characterizations of the final functioning device are performed. Early experiments show great variations in raman crystallinity between μc-$Si_{1\text{-}X}Ge_X$:H single layers on wafer or glass (even with 50 nm a-Si:H buffer layers) compared to the same layer in the final device. For that reason, no single layer characterizations are performed. This dissimilarity of single layer depositions in contrast to the solar cell stack depositions was also recognized by researchers in the context of research on n-μc-$Si_{1\text{-}X}O_X$:H layers [45] and is caused by the stark relation between crystalline growth, roughness, and surface composition. A crystalline layer preferably starts growing at sharp structures of the substrate [104]. This is the reason why a very thin layer of very crystalline material is inserted before the growth of a crystalline layer to start the crystal growth uniformly [104]. This layer is therefore called seed layer.

The μc-$Si_{1\text{-}X}Ge_X$:H single junction cells are deposited on commercially available glass covered with rough ZnO:Al from Nippon Sheet Glas[1]. The cells consist of a 50 nm thick microcrystalline p-layer, a 5 nm thick seed layer, a 1.2 µm thick μc-$Si_{1\text{-}X}Ge_X$:H

---

[1] http://www.nsg.com/

Plate Distance:	Pressure:	Power:	SiH_4 Flow:	GeH_4 Flow:	H_2 Flow:
10 mm	11 mbar	450 W	22.5 - 24 sccm	1.4 sccm	2900 sccm

Table 4.1: Deposition parameters for the µc-$Si_{1-X}Ge_X$:H reference absorber layer for the Leybold Phoebus Lab Coater.

absorber, and a 40 nm thick a-Si:H n-layer. A schematic of the cell stack can be seen in figure 2.1b). The cell area of 1 cm x 1 cm is determined by evaporating silver pads. This procedure to define the measurement area is commonly chosen by researchers for small cell areas [46, 53, 76, 93] and is used here as well in order to increase comparability. The parameters for the deposition of the µc-$Si_{1-X}Ge_X$:H reference absorber can be found in table 4.1. To gain a better understanding of the relation between the process parameters and the performance of the µc-$Si_{1-X}Ge_X$:H absorber, different process parameters are varied and the impact on IV cell performance, germanium content, and crystallinity is evaluated. Four different variations are performed independent of each other while keeping all other parameters constant:

1. germane flow variation
2. silane flow variation
3. hydrogen dilution variation
4. pressure variation

These four parameters were identified as crucial while studying the literature about µc-$Si_{1-X}Ge_X$:H absorbers [84, 86, 99, 102]. Germanium content and crystallinity are determined using the method described in section 2.3.5 using a laser with a wavelength of 633 nm.

4.2.1.1 Germane Flow Variation

In the first experiment, the germane flow of the µc-$Si_{1-X}Ge_X$:H absorber is varied from 1.0 standard cubic centimeter per minute (sccm) to 1.6 sccm in steps of 0.1 sccm while all other parameters are kept constant.

As can be seen in figure 4.1 a), the increased flow of germane leads to an almost linear increase in germanium content in the absorber by a factor of 6.3 %/sccm. This steep increase can be attributed to the high gas utilization because of the lower dissociation

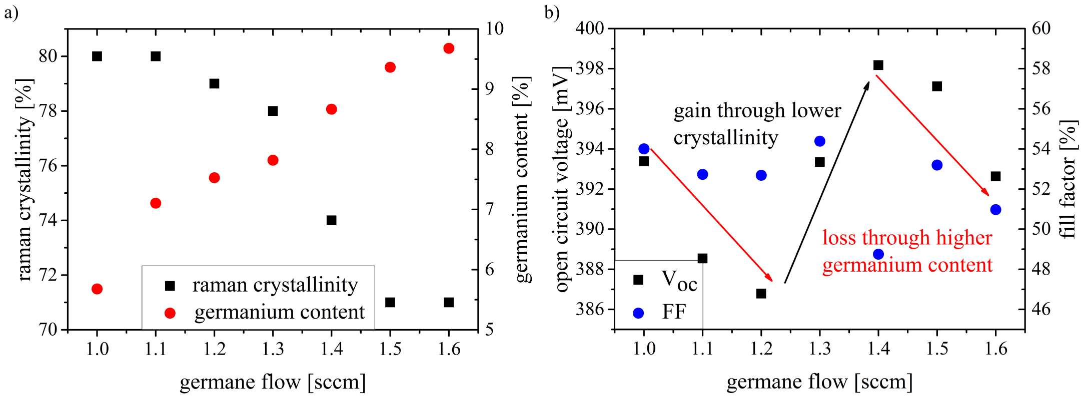

Figure 4.1: Raman crystallinity, germanium content, fill factor and V_{oc} values in relation to the germane flow of single μc-$Si_{1\text{-}x}Ge_x$:H cells.

energy of germane molecules compared to silane molecules. This effect was also described in [99] where the researchers found a nonlinear relation between germane flow and germanium content. In contrast to this experiment, they varied the flow over a larger range. A variation of the germane flow over a larger range might have resulted in the same behavior. At the same time, the germanium content in the layer increases and the crystallinity decreases from 80 % to 71 %. When increasing the germane flow, the increased germanium content introduces stress into the lattice because of the different bond lengths (see section 4.1.2) and thereby reduces the crystallinity. While the germanium content in relation to the germane flow is covered in the literature, the relation to the crystallinity in μc-$Si_{1\text{-}x}Ge_x$:H layers has not been addressed by other groups.

Looking at the V_{oc} values of the cells in figure 4.1 b), one can see three distinct sections: a decrease in V_{oc} for a germanium flow up to 1.2 sccm (section 1), an increase in V_{oc} for a germanium flow between 1.2 and 1.4 sccm (section 2), and a decrease in V_{oc} for a germanium flow from 1.4 to 1.6 sccm (section 3). The crystallinity stays nearly constant in section 1 and 3 (red lines), but the germanium content increases.

As alloying of μc-Si:H with germanium narrows the band gap and increases the carrier recombination rate, it is responsible for the change in V_{oc}. This is confirmed by other researchers that found similar behaviors [85, 99].

The very steep change in crystallinity in section 2 (black line) accounts for the increase in V_{oc} values. A shift to a more amorphous phase and thus higher band gap over-compensates the effect of V_{oc} loss due to higher germanium content. With high and low germane flows the reverse happens: Raman-crystallinity stays constant, ger-

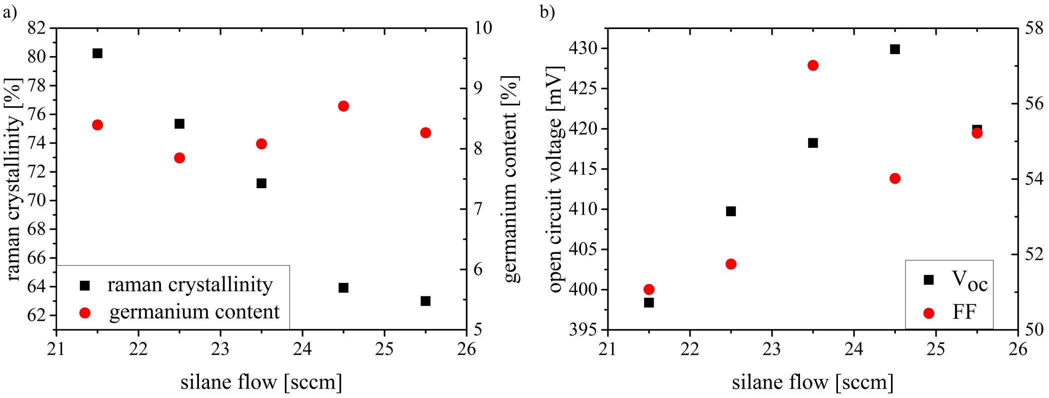

Figure 4.2: Raman crystallinity, germanium content, fill factor, and V_{oc} values in relation to the silane flow of single µc-$Si_{1-X}Ge_X$:H cells.

manium content increases, and the V_{oc} values drop (section 1 and 3, red lines).
Since state of the art µc-Si:H single junction cells exhibit V_{oc} values of 500 mV or more, V_{oc} values for the µc-$Si_{1-X}Ge_X$:H absorbers have to be optimized with other process parameter variations in order to build efficient bifacial single junction cells with a µc-$Si_{1-X}Ge_X$:H absorber. As stated in [85], developing a µc-$Si_{1-X}Ge_X$:H is a constant struggle of loss of V_{oc} and FF versus the gain in J_{sc} and therefore thinner layers.

4.2.1.2 Silane Flow Variation

Increasing the silane flow from 21.5 sccm to 25.5 sccm (while keeping all other parameters constant) reduces the raman crystallinity from 80 % to 62 % due to a larger amorphous volume fraction in the absorber.
Comparing figure 4.2 a) and figure 4.1 a), the difference is that changing the germane flow has a similar effect on the crystallinity but changing the silane flow does not have the same effect on the germanium content of the layer. The reason for the almost constant germanium content despite changes in crystallinity might be found in the low dissociation energy of germane. Splitting two hydrogen atoms from silane takes twice the energy compared to splitting two hydrogen atoms from germane [105]. Because of the high energy plasma used in microcrystalline depositions, all available germane is dissociated and deposited. Therefore, all germanium in the deposition gas will be incorporated with a very high probability [106]. Changing the relation between hydrogen and silane in the plasma alters the crystallinity while still incorporating all

germanium. The germanium in the deposition gas will be always depleted and a change in silane to germane ratio in the deposition gas composition will not change the germanium content in the layer. These results match the results obtained in the publication about the composition of crystalline layers from germanium and silicon [106].

The linear decrease in crystallinity depicted in figure 4.2 a) leads to a linear increase in V_{oc} values in figure 4.2 b). The higher amorphous volume fraction shifts the band gap to higher energies without the additional influence of a great variation in germanium content. Similar to the fill factor values of the germane flow variation (figure 4.1 b)), the fill factor values do not change with increasing silane flow (as can bee seen in figure 4.2 b)) and remain around 52 %.

The low value can be explained by the presence of germanium dangling bonds that act as acceptor-like states as explained in section 4.1.2. Since the presented values are deposited with a not optimized p-layer, part of the low values can also be attributed to a reduced interface quality and insufficient internal field. The challenge of reduction of the FF values when adding germanium was noticed by other researchers as well [85] and needs to be taken into account when evaluating the performance of μc-$Si_{1\text{-}X}Ge_X$:H absorbers.

4.2.1.3 Hydrogen Dilution Variation

To determine the influence of the hydrogen dilution during deposition on the raman crystallinity, germanium content, and electrical performance, the H_2 flow is varied from 2700 sccm to 3300 sccm in steps of 200 sccm. As expected from prior experiments with μc-Si:H, an increase in dilution with hydrogen deceases the raman crystallinity of the absorber. Similar to the germane and silane variation in figures 4.1 a) and 4.2 a) respectively, the germanim content in the layer stays almost constant (see figure 4.3 a)).

Comparing figure 4.2 b) and figure 4.3, one can see a decline of fill factor and V_{oc} values after a plateau at a dilution of 2900 sccm H_2 flow which is congruent with the behavior of the silane flow variation in reverse.

The increase in raman crystallinity leads to a more porous material with voids and points of recombination, decreasing the fill factor. The higher crystalline volume fraction of the material leads to a bandgap shift in the opposite direction compared to the silane flow variation. These results are in line with publications about the crystallinity of pure μc-Si:H cells without germanium [107]. The addition of germanium

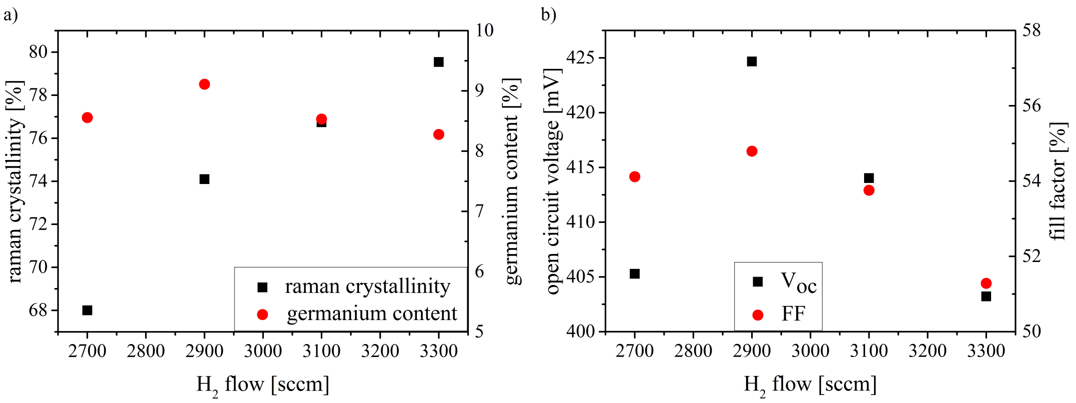

Figure 4.3: Raman crystallinity, germanium content, fill factor, and V_{oc} values in relation to the hydrogen dilution during deposition of single μc-$Si_{1-x}Ge_x$:H cells.

at the level of below 15 % does not change the behavior of crystalline silicon in respect to hydrogen dilution, it only shifts it to a lower crystallinity because of the above mentioned reasons.

4.2.1.4 Pressure Variation

In addition to the germane and silane flow, the process pressure is a key parameter in μc-$Si_{1-x}Ge_x$:H depositions because it significantly influences the material quality [99]. As can be seen in figure 4.4 a), the pressure is varied from 8.5 to 11 mbar. The germanium content is almost constant and varies only slightly between 8.3 and 8.7 %. As the pressure increases, the crystallinity declines from 77 to 61 %.

Comparing figure 4.2 a) and figure 4.4 a) one can see that increasing the silane flow shows the same effect on crystallinity and germanium content as increasing the pressure: Crystallinity decreases but the germanium content stays constant. The reduction of crystallinity has an enhancing effect on the open circuit voltage. Because bad material quality influences the shunt and series resistance (see section 4.1.2), fill factor values are a good gauge to estimate the material quality. Figure 4.4 b) shows a linear increase of fill factor values with increasing process pressure. Similar to the silane flow variation, this parameter does not change the germanium content in the absorber. Comparing figure 4.2 b) and figure 4.4 b), one can see that changes in the crystallinity due to process pressure variations are crucial to good fill factor values while a change in crystallinity through variation in the silane flow has no impact. The increased pressure leads to a compact material with a reduced defect density of germanium

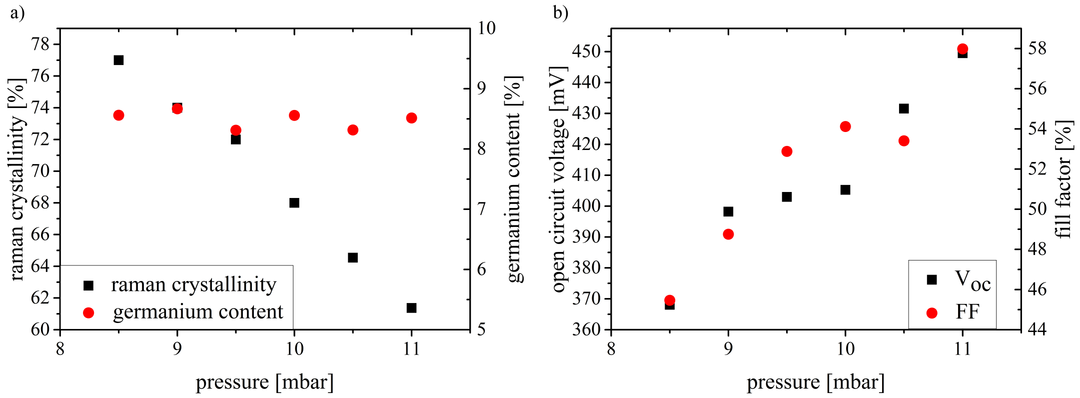

Figure 4.4: Raman crystallinity, germanium content, fill factor, and V_{oc} values in relation to the process pressure of single μc-Si$_{1-X}$Ge$_X$:H cells.

Material:	$J_{sc}\left[mA/cm^2\right]$	V_{oc}[mV]	FF[%]	η[%]
μc-Si:H	17.7	512	65	5.9
μc-Si$_{1-X}$Ge$_X$:H	18.9	463	62	5.4

Table 4.2: Comparison of top performance electrical values for μc-Si:H and μc-Si$_{1-X}$Ge$_X$:H absorber materials for BIPV applications.

dangling bonds [94]. This is similar to the results obtained by other researchers for other μc-Si$_{1-X}$Ge$_X$:H deposition regimes [85, 94] and shows that pressure is a key parameter for high quality absorber material even for low concentrations of germanium in the absorber.

4.2.1.5 Application in Single and Multijunction Cells

In order to compare the performance of the μc-Si$_{1-X}$Ge$_X$:H absorber layers to standard μc-Si:H absorbers, two single cells are deposited on the same substrate mentioned before. They are deposited with a thickness of 1200 nm and only the absorber recipe is different. The results of the comparison can be seen in table 5.2. Comparing the two absorber layers, the benefit of using germanium in the layer is directly visible: The short-circuit current of the absorber with germanium inside is 1.2 mA/cm^2 higher. This is illustrated in figure 4.5. Although there is a slight difference between the calculated values in the EQE measurement and the IV measurements, the trend and the distance is the same. The improvement of the spectral response of the μc-Si$_{1-X}$Ge$_X$:H

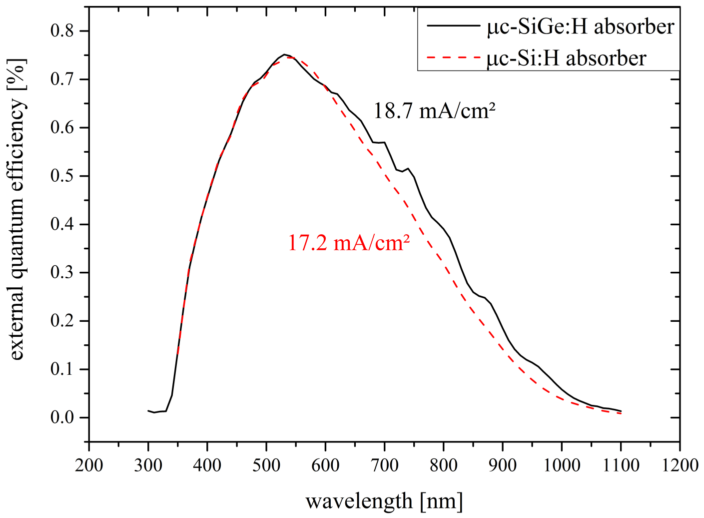

Figure 4.5: External quantum efficiency for microcrystalline silicon and silicon germanium absorbers of 1200 nm thick absorbers with calculated short circuit current density.

absorber layer is mainly in the red region of the spectrum because the blue part of the spectrum is mainly determined by the parasitic absorption of light in the p-layer which is the same in both cell stacks. The increase of the absorption of the μc-$Si_{1\text{-}X}Ge_X$:H layer is comparable to what can be found in the literature [85, 99] for higher concentrations of germanium in the layer. Looking at the infrared part of the μc-$Si_{1\text{-}X}Ge_X$:H layer quantum efficiency in figure 4.5, no absorption past the bandgap for pure μc-Si:H is visible. Therefore, the bandgap of the μc-$Si_{1\text{-}X}Ge_X$:H layer is only slightly different than the bandgap of the μc-Si:H absorber because of the low concentration of germanium. With higher germanium concentration a shift of the bandgap and an increased absorption should be visible (see section 4.1.2). Looking at the V_{oc} and FF values in table 4.2, the same trend mentioned before is visible: Both values are lower for the μc-$Si_{1\text{-}X}Ge_X$:H absorber compared to the μc-Si:H absorber. This is similar to the results in [85, 99]. Because of the higher defect density, FF is lower and V_{oc} drops because of the bandgap shift.

For BIPV applications, a single junction cell has some advantages for special transparent applications. This topic will be explored in detail in the following chapter. For all applications that are not transparent, a high efficiency solar cell makes more sense. In order to increase the efficiency of silicon-thin film solar cells, the industry switched

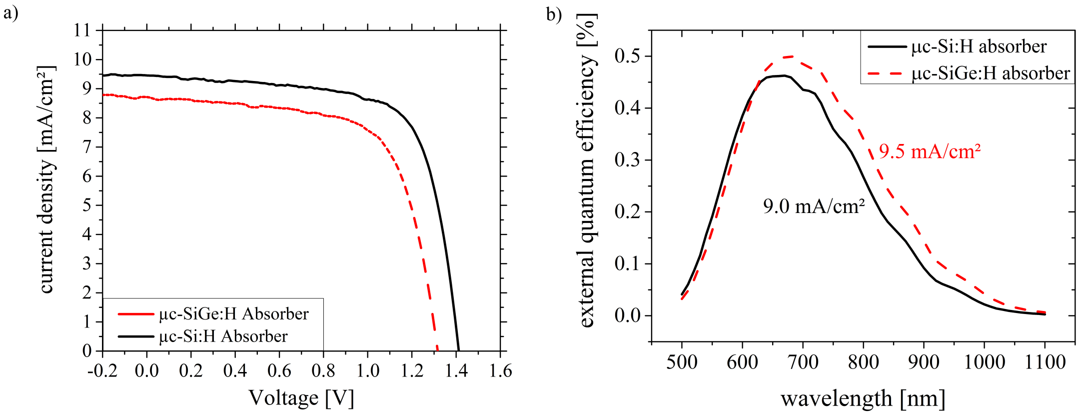

Figure 4.6: a) I-V measurements and b) External quantum efficiency for microcrystalline silicon and silicon germanium bottom absorbers of thin (720 nm) tandem cell bottom absorbers with calculated short circuit current density.

Material:	$J_{sc}\left[mA/cm^2\right]$	$V_{oc}[mV]$	FF[%]	$\eta[\%]$
µc-Si:H	9.4	1.41	70	9.3
µc-Si$_{1-X}$Ge$_X$:H	8.7	1.27	67	7.4

Table 4.3: Comparison of top performance electrical values for different thin (720 nm) bottom absorber materials in tandem solar cells for BIPV applications.

from single to tandem and in some cases even triple junction cells [12, 108]. Therefore, it makes sense to test the thickness reduction potential of the µc-Si$_{1-X}$Ge$_X$:H absorber in tandem and triple-junction configuration. Even if the efficiency of the resulting stack with µc-Si$_{1-X}$Ge$_X$:H absorber is slightly lower compared to its µc-Si:H counterpart, it might make sense for the industry to produce it because of the lower production time. A solar cell that can be produced in a faster process would be cheaper for the manufacturer to produce because a big part of the costs are fixed and do not scale with throughput. Counteracting that is the high price of germane that would drop with increasing demand. The electrical performance of the tandem cell with µc-Si$_{1-X}$Ge$_X$:H is lower than the performance of the tandem solar cell without germanium in the bottom absorber displayed in table 4.3. The lower V_{oc} and FF that are also visible in figure 4.6 a) are expected. As mentioned before, because of the higher defect density, FF is lower and V_{oc} drops because of the bandgap shift. These results are similar to publications of germanium bottom absorbers in tandem cells with a higher concentration of 17 % germanium [85]: They managed to obtain a

Material:	$J_{sc}\left[mA/cm^2\right]$	V_{oc}[mV]	FF[%]	η[%]	d_i [μm]
μc-Si:H	8.4	1.8	73	11.0	4.4
μc-Si$_{1\text{-}X}$Ge$_X$:H	8.4	1.7	65	9.2	2.25

Table 4.4: Comparison of top performance electrical values and thickness d_i of the combined absorber layers for different bottom absorber materials in triple solar cells for BIPV applications.

drop in V_{oc} of only 0.1 V compared to our 0.14 V and maintained FF and J_{sc}. To put the results in perspective: Our cell stack is not optimized, uses no special coatings, and is fabricated on a commercial substrate with a small scale industrial tool.

The EQE measurements in figure 4.6 b) show that the drop in J_{sc} is not caused by an insufficient energy conversion in the μc-Si$_{1\text{-}X}$Ge$_X$:H absorber. In fact, it shows that the μc-Si$_{1\text{-}X}$Ge$_X$:H absorber has a higher current generation density compared to the μc-Si:H absorber layer. The optimum μc-Si$_{1\text{-}X}$Ge$_X$:H tandem cell could therefore have a thinner absorber layer and the lower overall J_{sc} is not caused by the μc-Si$_{1\text{-}X}$Ge$_X$:H absorber layer.

To demonstrate the thickness reduction potential of a μc-Si$_{1\text{-}X}$Ge$_X$:H absorber, it is applied to a triple junction stack as the bottom most absorber. The stack is the same as in figure 2.1 c) with an additional p-i-n layer at the bottom of the cell before the back TCO contact. Silicon thin-film triple junction cells have been demonstrated with an initial efficiency of up to 16.3 % [50]. The high efficiency makes them ideal candidates for BIPV projects because of their high energy yields. The disadvantage of those cells is the thickness. The cell in [50], for example, has an overall absorber thickness of 4 μm. The thick layers lead to long production time which in turn increases the production costs. A way to avoid this problem is to use a bottom absorber with increased absorption. Therefore, a standard triple junction cell with one amorphous top absorber and two μc-Si:H bottom absorbers is used as a benchmark. The lowermost μc-Si:H absorber is then switched out with our μc-Si$_{1\text{-}X}$Ge$_X$:H absorber and the thickness of the absorbers is varied in order to reach the same J_{sc} for both cell stacks and all absorbers. Looking at table 4.4 and figure 4.7 a), one can see the thickness reduction potential. Both stacks have the same J_{sc} of 8.4 mA/cm^2 despite the fact that the cell with μc-Si$_{1\text{-}X}$Ge$_X$:H bottom absorber layer has only half of the total absorber layer thickness compared to the benchmark triple junction cell. The EQE measurement in figure 4.7 b) confirms that the current generation density in the bottom absorber is the same despite the thickness difference. The fact that the simulated short circuit

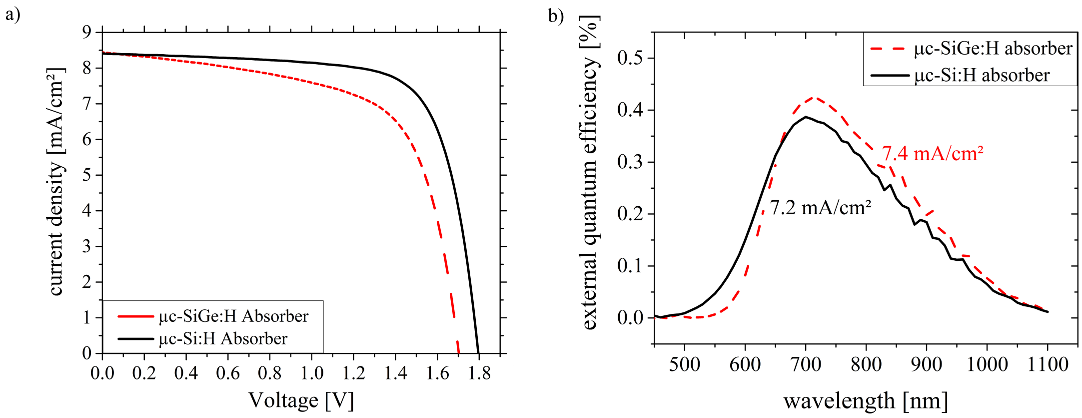

Figure 4.7: a) I-V measurements and b) External quantum efficiency for microcrystalline silicon and silicon germanium bottom absorbers of triple cell bottom absorbers with calculated short circuit current density.

current density from the EQE of 7.4 and 7.2 mA/cm^2 is rather far away from the measured 8.4 mA/cm^2 hints at the possibility of an inaccurate EQE measurement. The reason can be found in the difficulty of measuring triple junction cells. Flooding the two topmost cells with bias light in order to measure the bottom absorber performance independently is no easy task. Even if the total error of the EQE measurement seems to be quite high the relative error between the two measurements should be less because both cells are measured with the same procedure.

Comparing the rest of the electrical characteristics, a difference of 0.1 V in V_{oc} is visible. This value is 0.04 V better than the performance difference of the tandem cell comparison. The big difference in performance can be seen in the FF which is 8 % lower for the cell stack with μc-$Si_{1-X}Ge_X$:H absorber. This can be caused by a high defect density and reduced bandgap or a better current matching of the three cells [83]. Literature on triple junction cells with μc-$Si_{1-X}Ge_X$:H bottom absorber of similar composition and thickness show an even lower FF value of 63 % [109] and a similar efficiency of 9.3 %. With an a-SiGe:H middle absorber they reached a maximum efficiency of 12 %. The performance reached with our absorber is therefore comparable to the performance reached by other researchers. Especially for BIPV modules, a thin module with a short production time is very attractive.

Material:	$J_{sc}\left[\mathrm{mA/cm^2}\right]$	V_{oc}[mV]	FF[%]	η[%]
a-Si:H	11.7	929	65	7.0
μc-Si:H	17.7	512	65	5.9
μc-$Si_{1\text{-}X}Ge_X$:H	18.9	463	62	5.4

Table 4.5: Comparison of top performance electrical values for different absorber materials for bifacial thin-film solar cells.

4.2.2 Amorphous Silicon-Germanium Absorbers

Comparing the different initial electrical characteristics of all the single cell absorber materials a-Si:H, μc-Si:H, and μc-$Si_{1\text{-}X}Ge_X$:H in table 4.5 with absorber thicknesses of 250 nm, 1200 nm, and 1200 nm respectively, advantages and disadvantages of the different absorbers for bifacial applications can be determined. Why only single cells are feasible for bifacial applications will be elaborated in the next chapter. The benefit of using a μc-$Si_{1\text{-}X}Ge_X$:H absorber instead of a pristine microcrystalline silicon absorber can be seen in the increase of J_{sc} of more than 1 mA/cm^2 which confirms the measurements in figure 4.7. The before mentioned bandgap shift is also visible in the 49 mV lower V_{oc} value as well as the increase in germanium dangling bonds causing lower material quality and therefore a lower FF value.

Looking at the efficiency of those absorber materials, the μc-Si:H has a clear advantage over the μc-$Si_{1\text{-}X}Ge_X$:H absorber at this stage of development. Taking into account that germanium is a rare and therefore expensive material with a price approximately 30 times that of silane [110], leads to the conclusion that the μc-$Si_{1\text{-}X}Ge_X$:H absorber material is no alternative as a bifacial absorber material at this state of development. Comparing the a-Si:H and the μc-Si:H absorber and taking the 10 % degradation of the a-Si:H absorber into account, the a-Si:H has a clear advantage because of its faster deposition time and therefore lower production costs.

As mentioned before, there is a fourth option: a-SiGe:H absorber incorporate up to 30 % germanium but have poorer performance and stability compared to their a-Si:H counterpart [111].

While depositing a-Si:H/μc-Si:H tandem cells in between the experiments with the μc-$Si_{1\text{-}X}Ge_X$:H solar cells, an increase in current generation density for the a-Si:H top cell is discovered. Since the bottom absorber could limit the J_{sc} of the device, J_{sc} calculated from EQE measurements are depicted in figure 4.8. The mean value of calculated J_{sc} values is approximately 0.8 mA/cm^2 higher for tandem depositions after

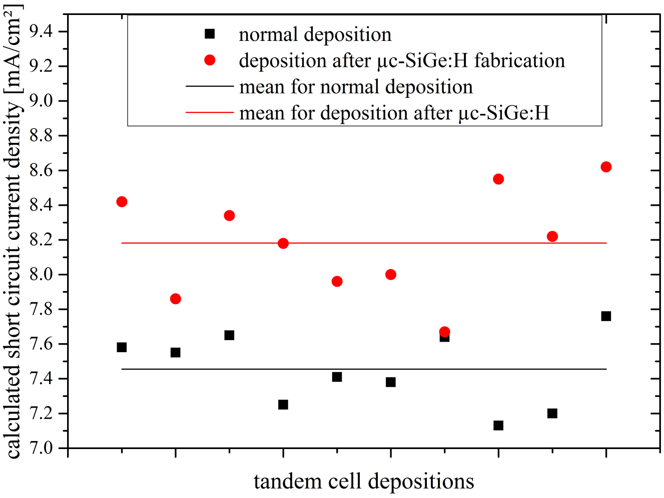

Figure 4.8: Calculated J_{sc} values for a-Si:H tandem top cell absorbers from EQE measurements for normal depositions and for depositions following the fabrication of µc-$Si_{1\text{-}X}Ge_X$:H absorbers. Lines are mean values of the data points.

a µc-$Si_{1\text{-}X}Ge_X$:H deposition. Since the accumulation and redeposition of germanium inside the deposition chamber was anticipated, blind depositions in excess of 300 nm are performed after each deposition of µc-$Si_{1\text{-}X}Ge_X$:H.

To determine the composition of the amorphous absorber after a deposition of µc-$Si_{1\text{-}X}Ge_X$:H and blind deposition, samples are measured with rf GD ToFMS. The results are depicted in figure 4.9. To determine the position of the amorphous top cell i-layer in the tandem pin/pin structure, the boron intensity is plotted as well (intensity magnified 10000 times). Since the amorphous i-layer (and the top cell n-layer) is sandwiched between two p-layers, its position is between two boron intensity spikes. Because the measurement is performed reverse to the deposition process, the first p-layer (top of the cell stack) is on the right hand side of the graph.

Although the germanium intensity is magnified by 400 times compared to the silicon intensity, the presence of germanium content in the absorber can be verified. The doping of silicon in the p-layer with boron leads to a boron signal 10000 times smaller than the silicon signal. It is therefore ambiguous to speak of doping when referring to the 400 times smaller germanium signal. The absorber composition of the µc-$Si_{1\text{-}X}Ge_X$:H absorber layers with a germanium content of 10 % were called alloy in the previous section. Since the germanium content in the layer is far below 1 %, it will be referred

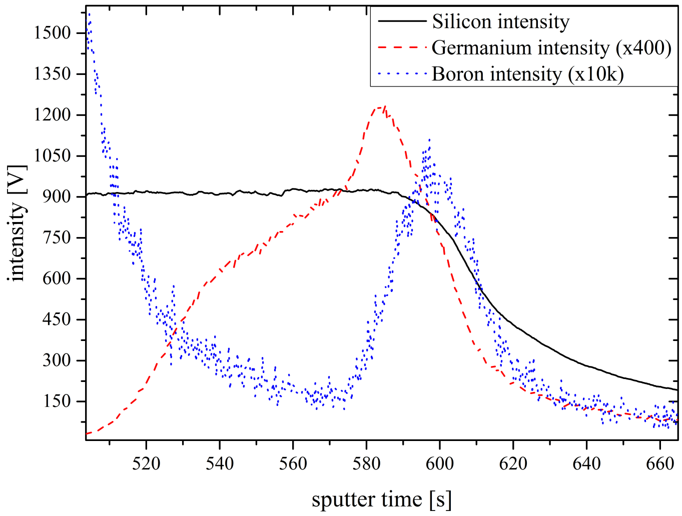

Figure 4.9: Glow discharge measurement of germanium doping of amorphous top cell absorbers by residual chamber redeposition of germanium. Boron concentration is depicted for locational purposes. Measurement was done with the support of Maria Hammer in the facilities of the Labor für Chalkogenid-Photovoltaik at the University of Oldenburg

to as traced with germanium.

The tracing of the absorber with germanium is clearly visible in figure 4.9. There seems to be a higher concentration of germanium near or at the p-i interface of the amorphous absorber. Because a chamber preconditioning with 1.2 µm of µc-$Si_{1-X}Ge_X$:H followed by 300 nm a-Si:H is no feasible method to increase the current generation density of an absorber, the following experiments are designed to recreate the tracing of an a-Si:H absorber with germanium:

1. Duration of the germane tracing
2. Position of germane tracing
3. Frequency of the germane tracing

The process parameters are the same as reported in section 5.3 and 5.4 except that the absorber thickness is fixed at 150 nm to create a thin and fast process attractive for industrial applications. An additional advantage of the small absorber thickness is a lower degradation because of the stronger internal electrical field in the absorber layer [33: p. 212]

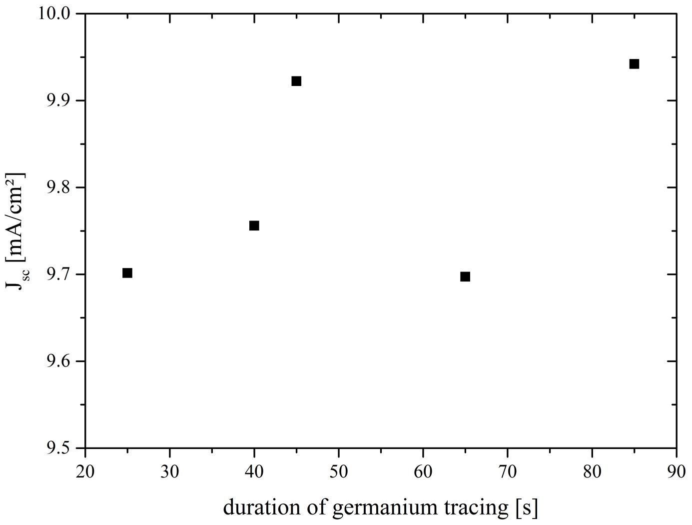

Figure 4.10: Variation in the germane gas addition duration during processing of an amorphous silicon absorber to achieve a germanium tracing for increased current generation.

4.2.2.1 Duration of the Germane Tracing

In order to recreate the very low germanium amount available in the deposition chamber, the amorphous absorber depositions are stopped at the middle of the fabrication. During the stop, the smallest amount of germane possible (0.25 sccm) for the mass flow controller was added to the gas mix in the process chamber. The absorber deposition prior and after this addition is made without germane in the deposition gas mix. The duration of this tracing of the deposition gas with germane is varied in this experiment. The results are depicted in figure 4.10. Because the first half of the absorber is already deposited when the germanium tracing takes place, germanium is only traced into the second half of the absorber. The short circuit current generation density increases with the amount of germane pumped during the brake of the absorber deposition.

The chamber walls and the electrode are covered with intrinsic amorphous silicon in between depositions to increase the comparability of the experiments. The level of short circuit current density generation increase of the tandem cells is not achieved by this tracing experiment and reaches only an increase of approximately 0.3 mA/cm^2.

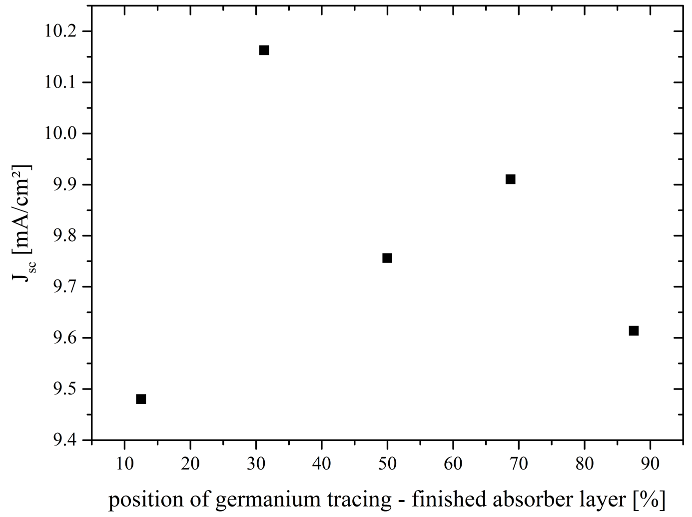

Figure 4.11: Variation in the germane gas addition position during processing of an amorphous silicon absorber to achieve a germanium tracing for increased current generation.

4.2.2.2 Position of Germane Tracing

Figure 4.9 showes a spike of germanium concentration at the p-i interface. A series of depositions are performed in which the position of the before mentioned germane addition to the process gas and therefore the break in the deposition of the absorber is moved from the beginning of the deposition to the end. Figure 4.11 shows the results of this variation. The tracing of the absorber with germanium at the p-i interface (at the very beginning of the deposition) results in the lowest increase of short circuit current density. The interface between these layers is crucial to the performance of the device [112] and might suffer from too much germanium content too close to it.

The other interface position at the end of the deposition between i- and n-layer does not show a great increase as well. The interface seems not to suffer from the addition of germanium since there is almost no absorber deposition left at this point and the increase in current density is higher compared to the addition at the beginning.

The introduction of germanium in the first third of the deposition leads to the greatest increase of 0.7 mA/cm^2 reaching nearly the level of the increased generation caused by the tracing caused by prior μc-Si$_{1\text{-}X}$Ge$_X$:H depositions. EQE measurements show

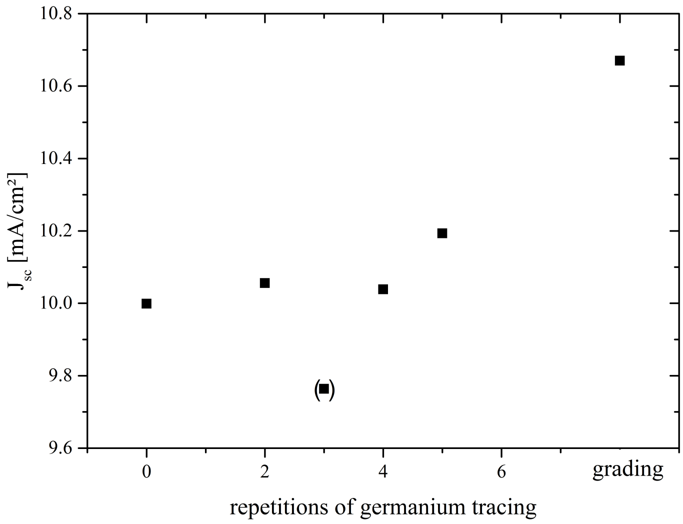

Figure 4.12: Variation in the germane gas addition frequency during processing of an amorphous silicon absorber to achieve a germanium tracing for increased current generation.

an increase over the whole spectrum, so no bandgap shift is visible. This is expected for such a small amount of germanium in the absorber.

4.2.2.3 Frequency of Germane Tracing

The germane inlet phases in this variation are spaced with equidistant timing during the deposition of the absorber layer. Based on the results from figure 4.10, the optimum gas inlet time of 45 s is chosen.

The last deposition on the right in figure 4.12 was fabricated with a grading of germanium tracing: Four breaks with germane gas inlets at shorter time intervals at the beginning of the absorber depositions and less to the end in order to take the different position effects of figure 4.11 into account. Only a small relation between repetitions and current density generation increase can be discerned. The data point of 3 repetitions is excluded as an outlier because errors during the p-layer depositions were discovered in hindsight. In order to compare the performance of the system at that time to the improvement by the germanium tracing, the data point of 0 repetitions is the reference cell without tracing.

With the optimum combination of gas inlet time and gas inlet grading with a focus on the beginning of the absorber deposition, the effect of germanium tracing of the absorber can be recreated and an increase of more than 0.7 mA/cm^2 is achieved. The tracing with germane has no influence on the light induced degradation performance. Both cells degrade the same amount as the cells shown in figure 3.10.

There is no mention in the literature of this effect, so no comparison can be drawn.

4.3 Conclusion

Highly efficient and stable thin film silicon solar cells are still in the focus of different research groups all over the globe [113]. Improving the performance of thin-film silicon solar cells without increasing the cost will lower the LCOE and increase the competitiveness of the technology. Since BIPV elements are already expensive, it is important to keep the expenses of adding solar to a minimum. In order to use high efficiency cells in industrial production, improvements to the deposition time caused by the very thick μc-Si:H bottom absorber have to be made. One way to achieve this goal is to replace the bottom absorber with μc-$Si_{1\text{-}X}Ge_X$:H using the smaller bandgap to utilize more of the solar spectrum.

In order to reach good material quality, there has to be a special focus on the pressure, power, and the crystallinity of the material. High pressure and power leads to a compact material reducing the count of germanium dangling bonds present in the material.

While the material quality reached in this work does not surpass the performance of μc-Si:H or a-Si:H absorbers, the feasibility and thickness reduction potential of up to 50 % reduced absorber thickness is demonstrated. A fast deposition process would enable tandem-junction cells to become more cost effective for market production and would boost the application of those modules for BIPV applications.

In addition, a way to enhance the performance of single a-Si:H cells has been developed: Tracing the deposition of a-Si:H absorbers with low amounts of germanium can lead to an increase in short-circuit current density generation of up to 10 %.

While the original tracing with germanium was caused by a contamination of the chamber walls by μc-$Si_{1\text{-}X}Ge_X$:H depositions, the effect could be recreated using minimal amounts of germane.

To sum up this chapter, μc-$Si_{1\text{-}X}Ge_X$:H as absorber material has the benefit of using more of the light spectrum compared to μc-Si:H absorbers. Therefore, thinner absorbers in tandem-junction cells can be used reducing the overall thickness and deposition time.

In order to increase the material quality of μc-$Si_{1\text{-}X}Ge_X$:H absorbers, a special focus has to be set on fabricating a compact material using high pressure and power, reducing the germanium dangling bonds in the material.

The a-Si:H absorbers traced with germanium are an excellent candidate for the use in bifacial cells. It is very quick to deposit and has enhanced absorption properties with using only a minimal amount of the expensive germane. A detailed analysis of bifacial thin-film silicon cells will be presented in the next chapter.

5

Amorphous Single-Junction Bifacial Cells for Building Integrated Photovoltaic

Thin-film silicon solar cells are an ideal candidate for application in bifacial BIPV modules for several reasons, as for example, tunable and homogeneous transparency. In this chapter, the concept of bifacial solar cells is introduced. The former chapters concentrated on enhancing thin-film silicon solar cells for BIPV applications while this chapter will give an example of how to use the advantages of thin-film silicon solar cells for a specific BIPV application: Bifacial modules.

An overview of current research concerning bifacial solar cells is followed by a s short outline of the necessary experimental and theoretical background used in the following sections. Simulated irradiance on different planes of orientations and tilts is shown in order to understand the different requirements for BIPV installed on facades or fences. State-of-the-art silicon thin-film solar cells in tandem-junction configuration are elaborated in terms of their feasibility for bifacial BIPV applications.

This chapter will outline the definition of bifaciality and the standards for measuring. A simulation is used to demonstrate how the vertical installment of bifacial solar cells can change the current generation profiles for northern Germany. A vertically installed bifacial module can receive even more radiation than a conventional module in optimum orientation. Depending on the orientation, it is able to shift the power generation profile to the early and late hours of day and even increase the generation in winter times. In order to determine the best cell stack for bifacial cells, tandem-junction cells are also considered for these bifacial applications. It turns out, tandem-junction cells are not feasible as bifacial modules because shifting illumination conditions make current matching almost impossible. Finally, the chapter investigates

how the bifaciality of amorphous single-junction thin-film solar cells can be increased by reducing the thickness and adding oxygen to the layer.
Benedikt Hanke helped with his Meteonorm related programming and Clemens Feser supported with the measurements on tandem-junction bifacial modules. Results of this chapter are published in [114].

5.1 Bifaciality

5.1.1 Overview

A bifacial solar cell is called bifacial instead of monofacial if a solar cell is able to absorb light from both sides or faces. Most solar cells in production use a metallic or foil light reflector on the backside. The idea of a back reflector is to reflect unabsorbed light passing through the solar cell back into it. Solar cells with a back reflector are therefore always monofacial. The most commonly used material is polyvinylfluorid (PVF) called Tedlar from the company DuPont [115].
The factor between the electrical performance of a solar cell illuminated perpendicular from the front side under STC and the performance when illuminated from the back side under the same conditions is called bifaciality. Bifaciality values are often given in rear side efficiency percentage of the front side efficiency [116].
This leads to a challenge concerning the characterization of bifacial solar cells: The standard testing conditions do not define the reflectance of the measurement block on which the cell is placed for characterization. STC measurements of bifacial solar cells may therefore differ from measurement facility to measurement facility. The research community is addressing this problem by proposing additions to the standard test conditions to address the measurement of bifacial cells [117].
In case solar modules are installed in a way that light scattered from objects behind them can reach the rear side of the module, using bifacial instead of monofacial solar cells can help to reduce the LCOE because those modules generate additional power in relation to their STC rating. The reflectivity of objects near solar modules is characterized by the albedo value. The albedo value is defined as the ratio of irradiance reflected from a surface to the irradiance received and refers to the entire spectrum. For green grass, the corresponding albedo value is 0.2 [118] and can reach up to 0.9 for snow, resulting in up to 90 % of the solar irradiance being reflected onto the backside of a solar module in winter.
Depending on the type of installation, various experimental tests and simulations show

Figure 5.1: The first Canadian photovoltaic system combining SANYO's heterojunction with intrinsic thin-layer (HIT) double bifacial solar PV modules and DuROCK TIOCOAT reflective roof membrane at DuROCK Alfacing International Ltd.'s headquarters in Woodbridge[119].

an increase of annual output power of 10 to 20 % when switching from monofacial to bifacial modules [120, 121]. This value is dependent on the local conditions. A mirror-like surface, like a lake surface behind modules floating on water [122], scatters mostly direct. Although the reflectivity is very high, the albedo value is therefore considered to be low. Foam and waves on the water increase the albedo value. A diffuse scattering material like titanium dioxide (white paint) or snow and chalk scatters the light more efficiently to the backside of the module. How much light reaches the backside of the module from the diffuse scattering background also depends on the inclination and orientation of the module and the sun. Under optimal circumstances, the increase in output power can reach up to 50 % [123]. Figure 5.1 depicts an installation making use of the back scattered light from the white rooftop by using bifacial modules, increasing the outputpower by 30 %, and keeping the building itself cooler [119].

As with STC for monofacial modules already, calculating the output power of a bifacial solar module for a given site is quite challenging: In addition to performance deviations caused by temperatures not equal to 25 °C and solar irradiation not equal to AM1.5G illumination with $1000\,\mathrm{W/m^2}$, one has to take the (annually shifting) albedo of the surrounding surfaces into account.

Research on bifacial photovoltaic solar modules has been performed since the 1960s [124]. It started with a moderate 7 % conversion efficiency for bifacial solar cells [125] and has reached 21 % conversion efficiency with a bifaciality of 80 % in industrial production [116]. Those experiments and products were all based on wafer based solar

Figure 5.2: Bifacial solar modules as noise barrier on the LSW Würmbrücke Munich [128].

modules.

Besides the conventional installation of bifacial modules mentioned above and the usage as road material mentioned in chapter 1, vertical BIPV are of key interest for the research community. Patents filed as recently as the beginning of 2015 [126] and research showing the value of vertical installation of photovoltaic for Japan [127] demonstrate the interest for vertical installation of bifacial modules. An Austrian company already demonstrated the feasibility of vertically installed bifacial modules as noise barriers. Figure 5.2 shows an example near Munich. Although dye-sensitized solar cell technology is suited for bifacial solar applications [129], most of the bifacial cell designs are based on silicon wafer technology. There are reports on bifacial cells for most fabrication methods, such as crystalline silicon (c-Si) bifacial cells in n-type, p-type, monocrystalline, and polycrystalline configuration [130–132]. HIT cell technology, which is a combination of a wafer with thin-film silicon to passivate the silicon wafer surface, shows good bifaciality values as well [133].

The bifacial cell technologies mentioned above are assembled into modules by sandwiching the cells between two sheets of glass. Modules with glass in the front and glass in the back are called glass-glass modules. Because of the relatively high costs of solar-grade glass, most c-Si based (monofacial) solar modules are sold with a white foil backsheet in glass-backsheet configuration. The industry is slowly switching the focus to the glass-glass modules to avoid long-term stability issues caused by the stress induced by the different coefficients of thermal expansion of the backsheet and the glass [134].

Since silicon thin-film solar modules are fabricated as glass-glass modules anyway, they are especially suited as bifacial modules. So far, very few researchers have focused on the topic of using thin-film silicon solar cells in bifacial configuration [56].

Despite the advantages mentioned in chapter 1, to this date no demonstrator using bifacial silicon thin-film modules in vertical installation has been installed anywhere.

5.1.2 Experimental and Theoretical Background

The illumination of objects by the sun follows certain physical laws. The amount of light hitting an object like a solar module depends strongly on its orientation in relation to the sun. The amount of particles (photons) intersecting a unit area is also called fluence. The physical relation between angle of orientation and the fluence of photons on the solar module is the cosinus:

$$\mathrm{H}_{\mathrm{module}} = \cos(\alpha) * \mathrm{H}_{\mathrm{sun}} \tag{5.1}$$

With α the angle of the normal vector of the plane to the sun, $\mathrm{H}_{\mathrm{sun}}$ the fluence coming from the sun, and $\mathrm{H}_{\mathrm{module}}$ the fluence through the module plane. This formula is applicable for both turning directions of the plane.

When turning the irradiated plane away from the position in which the normal vector of the plane points directly at the sun, the shadow cast by that plane will be reduced in size depending on the angle. The size of the shadow cast by the plane is equal to the fluence through the plane area. This is important because most of the solar modules are stationary and do not track the sun. Therefore, the angle between the sun and the solar module will change over the time of day and year because of the movement of the earth. For that reason, most solar modules that are not tracking the sun are installed to generate the most amount of power during a year. This leads to low fluences in wintertime for example because the sun is very low on the horizon and the angle α is very large.

Apart from the fluence relation, which cannot be avoided without tracking the sun, there is a second relation that impacts the performance of solar modules. When the angle α is very large, a phenomena called total reflexion takes place. Light does not pass through the module but is reflected off the surface of the glass. Depending on the surface of the solar module (which is glass most of the time) the total reflexion angle is approximately 40 °. Therefore, most solar modules are equipped with an anti reflection coating (ARC) that reduces the effect of total reflexion by modifying the optical interface between the air and the glass of the solar module.

Another way for sunlight to illuminate a solar module is being reflected from objects around the solar module. When the module is surrounded by white objects, the amount of light reflected on it in addition to the direct sunlight can be high. To characterize the reflectivity of the surrounding area, a value called albedo is used. The value ranges between 0 and 1. A very reflective surface like white paint has an albedo value close to 1 while black paint has an albedo value close to 0.

5.2 Simulation of Irradiance on Vertical Planes in Germany

Using a conventional wafer based solar cell in vertical configuration has the disadvantage of using only one half space and therefore only a reduced part of the incoming sunlight. The efficiency characterization of solar modules is dependent on the solar spectrum. The solar spectrum can be divided into three parts: The direct, indirect (diffuse), and reflected solar irradiance. The direct sunlight reaches the module surface after crossing the atmosphere with no further changes. Indirect sunlight is scattered on clouds or particles and far away objects before reaching the solar modules. The reflected part of the irradiation spectra results from the reflection of the near environment and back scattered sunlight of the ground. As mentioned in section 5.1.2, the corresponding value is called albedo.

For the behavior of ordinary modules, the reflected sunlight does not have any influence. Figure 5.3 depicts the composition of those parts for three German cities. Even the southernmost city Munich has an indirect solar irradiance of over 50 % in average over the year although the direct part of the sunlight is the highest compared to the other cities in the graph. A high percentage of indirect irradiance is the case for the northern European area in general. To get a deeper understanding, in which way the mounting orientation affects the power generation, the irradiance on a plane is calculated in relation to the angle of tilt and orientation. Data for this simulation is extracted from meteonorm [31]. The results are depicted in figure 5.4a). To understand this figure better, it helps to think of the simulation as a hemisphere on which an irradiance measurement plane of $1\,\mathrm{m}^2$ was placed for a year. The color coding shows the measurement value for planes placed on each normal vector on the hemisphere in percentage of the maximum. The black lines represent places where the yearly output

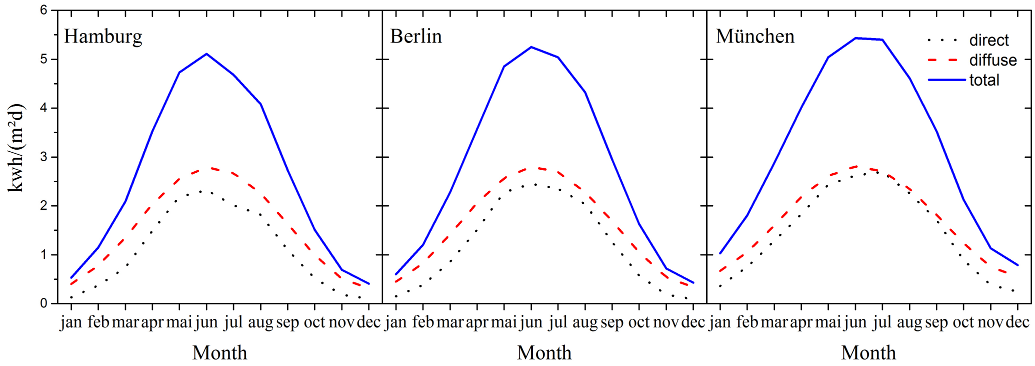

Figure 5.3: Composition of the solar spectrum in terms of direct and indirect irradiance for three German cities.

is the same, regardless of placement of the measurement plane.

To get the optimum yield in the yearly average for a conventional one sided module in Oldenburg Germany, it would have to face to the south and slightly to the west. In this optimum tilt, the average irradiance would reach 1137 kWh/m^2/a. The values are calculated with the irradiance going only through the front side of the measurement plane. For the albedo value surrounding the measurement plane, 0.25 was chosen. This is a conservative choice since typical albedo values of urban areas range between 0.3 and 0.45 [135]. The same calculation can be done for a vertical plane facing east, south, west, and north. Because of the before mentioned diffuse irradiation, the average irradiance on those vertical planes per year is still very high. The results of the calculations can be seen in figure 5.4b). A vertical one-sided module facing south would generate the highest average yearly yield with an irradiance of 844 kWh/m^2/a, which is 74 % of the irradiance of the optimum tilted installation. These figures also correspond to four points in figure 5.4a), the values directly adjacent to the letters N, E, S and W.

Bifacial modules in vertical installation are able to use both half spaces of the light hitting the back and the front side of the module and are able to compensate the negative effect of partial shadowing to a certain extent. Furthermore, the vertical installation increases the naturally occurring cleaning effects and reduces the negative soiling problems caused by leaves, bird drops, and similar impurities.

Thinking about noise barrier walls lining the motorways and railways going from north to south, we can use the data of figure 5.4b) to calculate the irradiance a bifacial module (100 % bifaciality) could convert to power in vertical installation facing east and

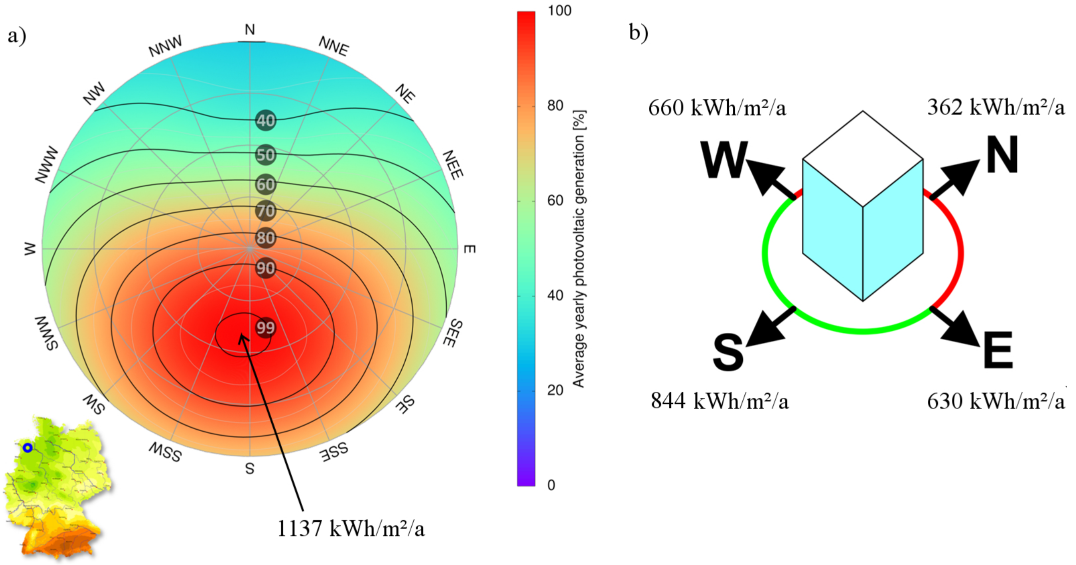

Figure 5.4: a): Tilt in relation to average yearly photovoltaic irradiance for Oldenburg, Germany. Black lines represent the isoline in percentage from the maximum irradiance. Gray lines can be used to measure degrees of tilt and orientation. Every gray circle represents 45 degrees of tilt and every gray line 22.5 degrees of orientation. b): Photovoltaic yearly average irradiance for vertical planes facing north, east, south, and west in Oldenburg with an albedo of 0.25. Both graphs are based on coding and graphs done by Benedikt Hanke.

west by adding the numbers. In yearly average, it would face 1290 kWh/m^2/a, which is 113 % a conventional module in the optimum tilt position would face. Even for vertical installations facing the module north and south, the yearly average irradiance would still be higher than for the modules in optimum tilt position (1206 kWh/m^2/a versus 1137 kWh/m^2/a). When using modules in vertical installation, the daily generation profile also changes. To give an example, irradiance date is used to to simulate the irradiance on different planes of orientation and tilt on an average day in July. The results are depicted in figure 5.5.

Using bifacial solar cells in vertical installation can shift the daily power generation peaks to the morning and evening hours, especially when the bifacial module is facing east and west (red dashes). But even the module facing north and south (black line) has increased production in the morning and evening hours compared to the monofacial module (blue dots), because in the summer the sun's arch is up to 240 ° and illuminates the bifacial cell from the north side at early morning and late evening. In the winter months, the sun's arch only covers 120 ° (calculated for 49 ° north) and does not illuminate the north side. This effect can reduce the demand for power

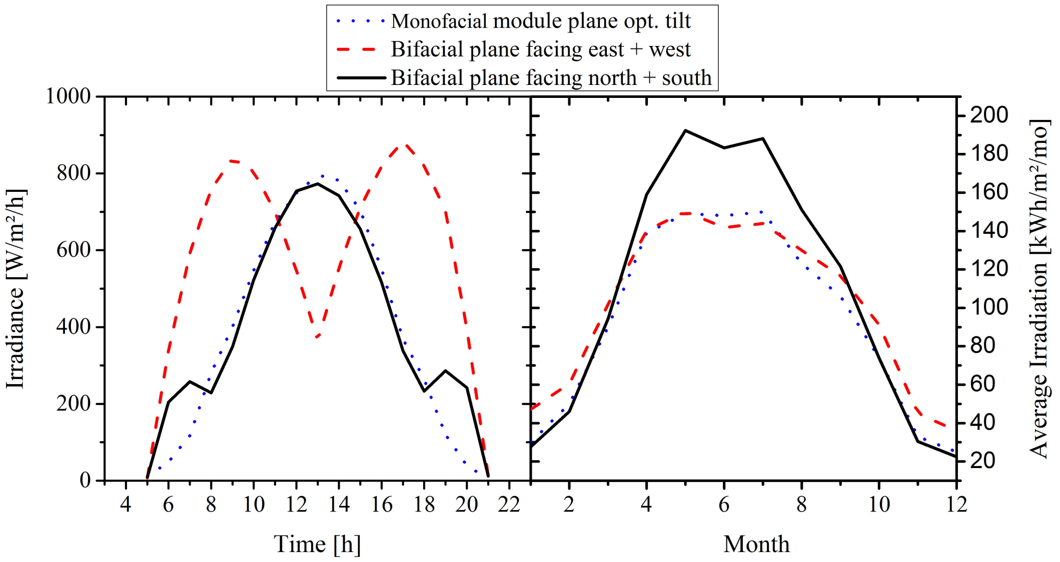

Figure 5.5: Left: Simulated irradiance of a random day in July in Oldenburg for different tilts and orientations of the module plane. Right: Monthly irradiance on the same planes. Data for this graph was extracted from Meteonorm using code from Benedikt Hanke.

storage and increase the self-consumption rate since the demand profile for northern European regions is not dominated by air conditioning [136].

The shift in the irradiance profile exists also on a yearly timescale. Using the same irradiance data, the same graph is calculated for these tilts and orientations on a monthly timescale. The results are shown in figure 5.5 on the right side. Bifacial cells facing in north/south direction have the benefit of being able to generate more power in the winter months because of the sun being lower in the sky. In contrast, bifacial modules facing east and west can generate more power in the sunny months compared to conventional tilted modules.

The simulation results match experimental results collected in Japan [127]. Though vertical installation possibilities of bifacial modules with no shading from either side might be infrequent, a clear benefit in terms of generation profile shift can be gained.

5.3 Multi-Junction Bifacial Solar Cells

Thin-film silicon solar modules can be fabricated in single-, tandem-, or triple-junction stacks. In order to determine the best stack for bifacial modules, the following tests are carried out. As a reference for the studies on multi-junction bifacial solar cells, a single

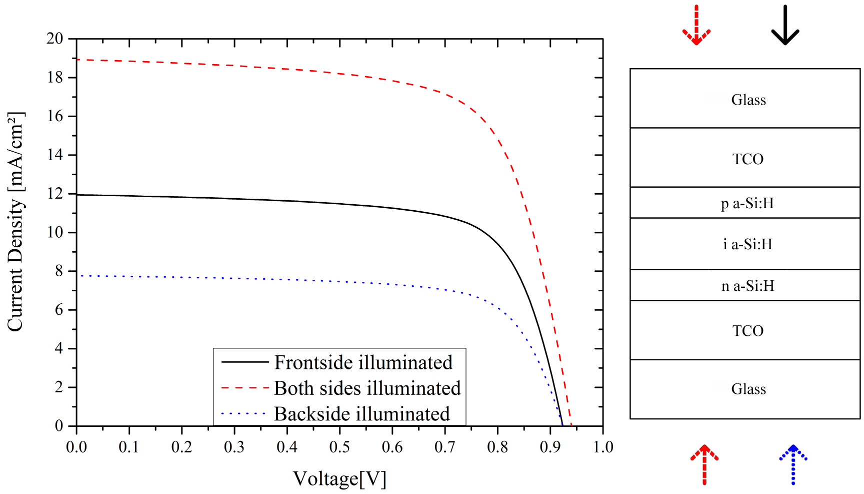

Figure 5.6: Structure and JV-characteristic of a bifacial a-Si:H thin-film solar cell (Z-002) under illumination from the front-, back, and both sides simultaneously. The measurements for this graph were done in collaboration with Clemens Feser.

junction cell is deposited (labeled Z-002). As depicted in figure 5.6, the cell consists of an amorphous cell sandwiched between two glass-TCO layers. The cell is illuminated from the front side, backside, and both sides simultaneously to determine the output characteristics when used in vertical installation. To measure the illumination from both sides simultaneously, a mirror array was constructed for the sun simulator (see chapter 2.3.1). The solar cell can be placed vertically under the device and two mirrors with a 45° angle to the solar cell reflect the light from both sides into it. This setup is similar to the setup that has later been suggested by the Fraunhofer ISE [11] to be used when measuring bifacial cells. As can bee seen in figure 5.6, J_{sc} of the reference cell when illuminated from the backside is far lower than the J_{sc} when illuminated from the front side (blue, dotted line versus the black, compact line). The bifaciality of this cell can be calculated with the following formula:

$$\frac{J_{sc,rear} * 100}{J_{sc,front}} = \text{Bifaciality } [\%] \tag{5.2}$$

Normally, the bifaciality would be calculated for the efficiency. In this case FF and V_{oc} do not change with illumination direction. Therefore, calculating the bifaciality for the short-circuit current is the same as calculating it for the efficiency. Using the formula above to calculate the bifaciality of the reference cell Z-002, results in a bifaciality of 66 %. Chapter 5.4 will address the challenge of how to increase the bifaciality and

Sample:	Tunnel Junction:
T-003	n μc-Si:H/p μc-Si:H
T-004	n μc-Si:H/p μc-SiO:H
T-005	n μc-Si:H/OMO/p a-Si:H
T-006	n a-Si:H/TCO/p a-Si:H

Table 5.1: Overview of the different tunnel junction stacks used to optimize the tunneling contact in bifacial a-Si:H tandem cells.

thereby achieve a maximum overlap of the blue, dotted line and the black, compact line.

The V_{oc} does not change in relation to the illumination direction but increases slightly when the cell is illuminated from both sides. This change in V_{oc} is expected since the distribution of charge carriers and therefore current density is changed by the photon injection from both sides. In a solar cell illuminated from only one side, the highest current density is at the p-layer [137] because most of the high energy small wavelength light is absorbed there. In a cell illuminated from both sides, the current generation density is highest at two points, at the p-layer and the n-layer. In case of a bifacial cell illuminated with a mirror from both sides simultaneously, high energy small wavelength light also hits the backside of the cell.

The J_{sc} of the cell illuminated from both sides can be approximated by the addition of the short circuit current densities of front and back illumination:

$$J_{\mathrm{sc,both}} = J_{\mathrm{sc,front}} + J_{\mathrm{sc,rear}} \tag{5.3}$$

To determine the value of multi-junction bifacial solar cells, different stacks of a-Si:H/ a-Si:H thin-film tandem solar cells are deposited on glass and compared to the single junction reference cell.

All the samples are prepared with an indium tin oxide (ITO) back contact which has the same function as a ZnO:Al back contact but is more expensive to deposit because of the indium. The cell stack is displayed in the top half of figure 5.7. The tunnel junction layers of the tandem devices are varied according to table 5.1. Because of the before mentioned injection of photons from both sides of the multi junction stack, the tunnel junction plays an important role and is crucial to the performance of the multi-junction cell. The results of this optimization can be seen in the bottom half of figure 5.7. The IV characteristics are displayed in relation to the single bifacial solar cell Z-002 illuminated from the front, in order to show the benefits of multi-junction bifacial cells in relation to their single junction counterpart under different illumination schemes.

The first data point is the single junction a-Si:H bifacial cell (Z-002) to compare the single, and multi-junction structure in different illumination setups. T-003 consists of two cells similar to Z-002 separated by a µc-Si-n/p tunnel junction. This multi-junction cell has a higher V_{oc} than the single cell counterpart. Because the contact between the cells is not optimized, FF and J_{sc} values are significantly lower than their single cell counterpart resulting in a lower efficiency.

Through the optimization of the tunnel junction depicted in table 5.1, it is possible to increase the V_{oc} to 193 % compared to the single cell structure while keeping the FF constant and reducing losses in J_{sc} to 35 %, so that the efficiency increases to 122 % when illuminated from both sides. A fully optimized, matched tandem junction cell should be able to reach 200 % output power because a tandem cell illuminated from both sides should basically be the same as two single-junction cells illuminated from only one side. The performance of the tandem cells when illuminated from only one side is very bad, reaching only 20 % of the efficiency of the single cell illuminated from the front side. Looking at figure 5.8 the reason can be identified:

The series connection of the sub cells limits the overall current density to the smallest value in the system. There is no difference in the current density for illumination by rear or front because of the current-density limiting bottom sub-cell (bottom sub-cell meaning the bottom cell seen from the illumination direction at that point). For an optimal performance of the multi-junction bifacial cell, both sub-cells have to generate the same amount of current density which is called current matching.

To keep the cells matched in real life conditions, the relation between the irradiance on the front side and the irradiance on the back side have to be maintained at all times and have to be matched to the current generation relation of the sub-cells. For a stationary module installation, this is not possible. Only tracking the sun with the solar cell would make this possible. Since the tracking and mounting of a solar cell is very expensive [138], combining it with a cell with low efficiencies makes no economic sense.

Therefore, using multi-junction cells for bifacial applications is not a feasible option. This result can be generalized to be applicable to all types of multi-junction solar cells because current-matching has to be done for all serially connected power generating devices. Removing the back reflecting layer of any multi-junction solar cell to

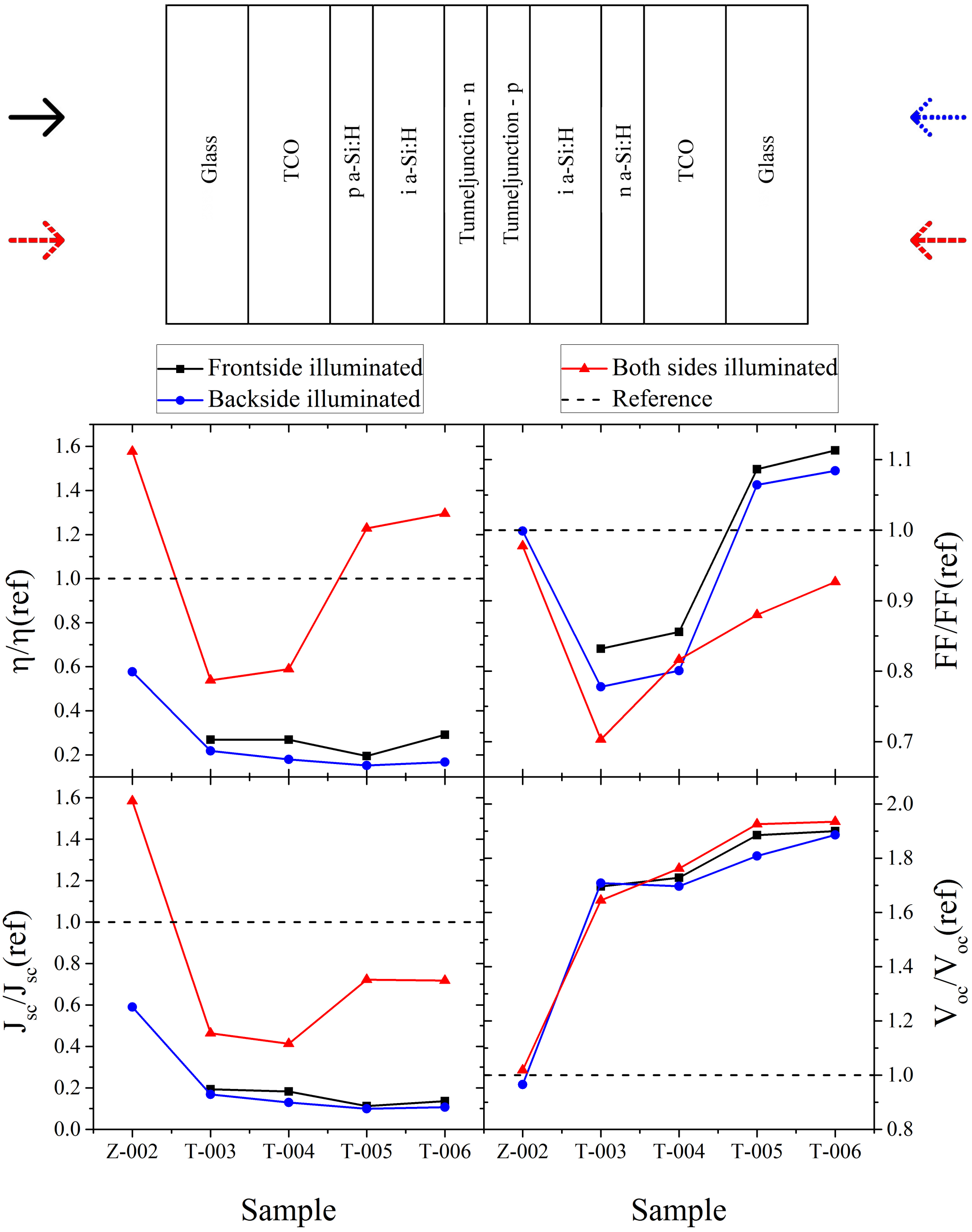

Figure 5.7: Structure and JV-characteristic of different tunnel junctions layers in bifacial a-Si:H thin-film tandem solar cells under illumination from the front, back, and both sides simultaneously in relation to the reference single cell illuminated from the front side only(Z-002).

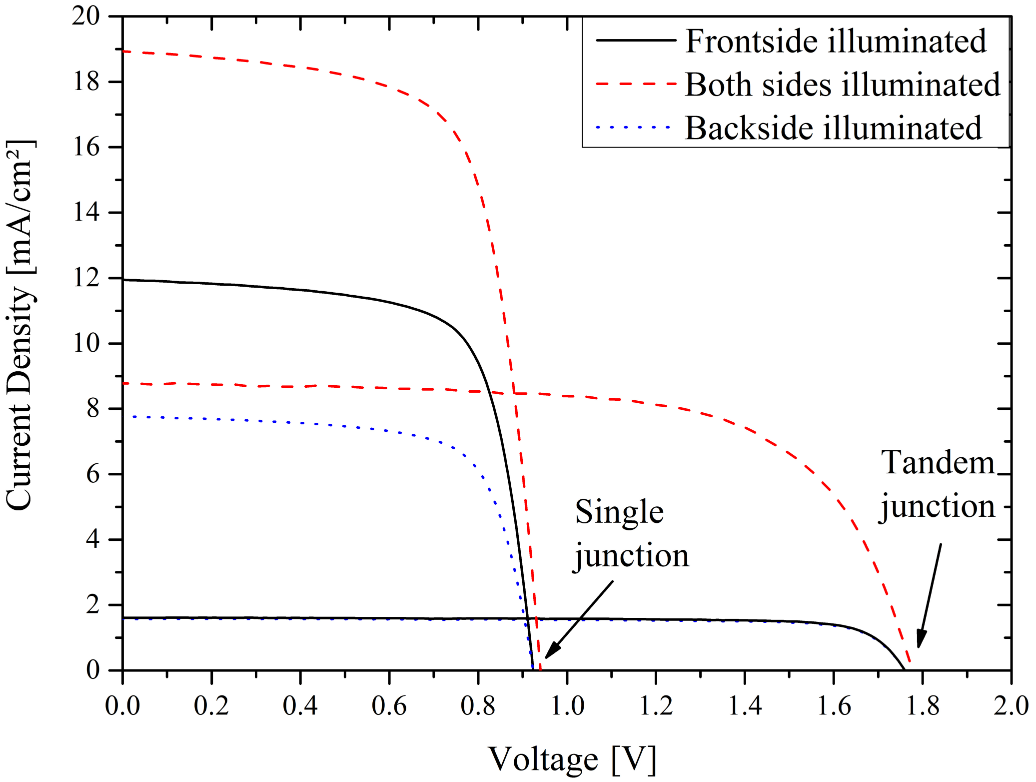

Figure 5.8: JV-characteristics of a single junction cell (Z-002) illuminated from the front, back, and both sides simultaneously in comparison to a bifacial tandem cell with optimized tunnel-junction (T-006).

gain bifaciality by collecting sunlight (direct or indirect) on the backside reduces the performance in almost all conditions and should be avoided.

5.4 Increasing the Bifaciality of Single Junction Amorphous Solar Cells

In the previous section 5.3, a bifaciality of 50 % was reached by using a standard process for the deposition of single a-Si:H thin film solar cells in combination with a transparent back contact. The i-layer thickness was fixed at 250 nm and showed the expected light induced degradation of 8 % in average (1000 h, @STC). No further optimizations where done. To improve the bifaciality of single junction amorphous solar cells the key element for high bifaciality was identified: The n-layer of the cell-stack.

In superstrate pin configuration, amorphous silicon thin film solar cells see light only from the p-side. Therefore, there has never been a need for blue wavelengths transparent n-layers. In the situation of a high bifaciality, the n-layer has to fulfill the same requirements as the p-layer. This means, a high transparency, high doping, less surface recombination, and good enough cross conductivity [83].
To improve the transmittance of the amorphous n-layer for low wavelengths, a variation of the following n-layer deposition parameters is carried out independent of each other:

1. the CO_2 concentration
2. the layer thickness
3. the doping concentration

An amorphous n-layer is chosen instead of the commonly used n-μc-$Si_{1\text{-}X}O_X$:H layer [48] because a better long term stability of highly doped amorphous n-layers compared to highly doped n-μc-$Si_{1\text{-}X}O_X$:H layers (see chapter 3) is expected. Furthermore, the process stability is better because the oxygen of the n-μc-$Si_{1\text{-}X}O_X$:H depositions accumulates very fast on the chamber walls of the deposition chamber and makes elaborate cleaning/blind-depositions necessary.

5.4.1 CO_2 Variation

To increase the transparency of the n-layer, especially in the 300 to 500 nm wavelength regime, a common approach is to alloy the layer by adding CO_2 to the deposition gas mixture [48]. When adding too much CO_2 gas to the mixture, a decrease of the n-conductivity can be observed [83]. To prevent such an effect, the CO_2 flow is increased in small steps until a gas flow of 10 sccm iss reached.
As shown in figure 5.9a), the addition of CO_2 did not change the behavior of the cell when illuminated from the p-side. Therefore we conclude that the used max gas flow of 10 sccm is small enough to neglect the influence on the n-layer conductivity. In contrast to the results of the p-side illumination, the short circuit current density increases slightly with the increasing gas flow. As expected, an increase of the transparency of the n-layer can be observed by increasing the oxygen content in the n-layer. The maximum benefit of 0.6 mA/cm is reached by adding a flow of 10 sccm CO_2 to the deposition gas mixture.
To show where the additional current is generated, the external quantum efficiency

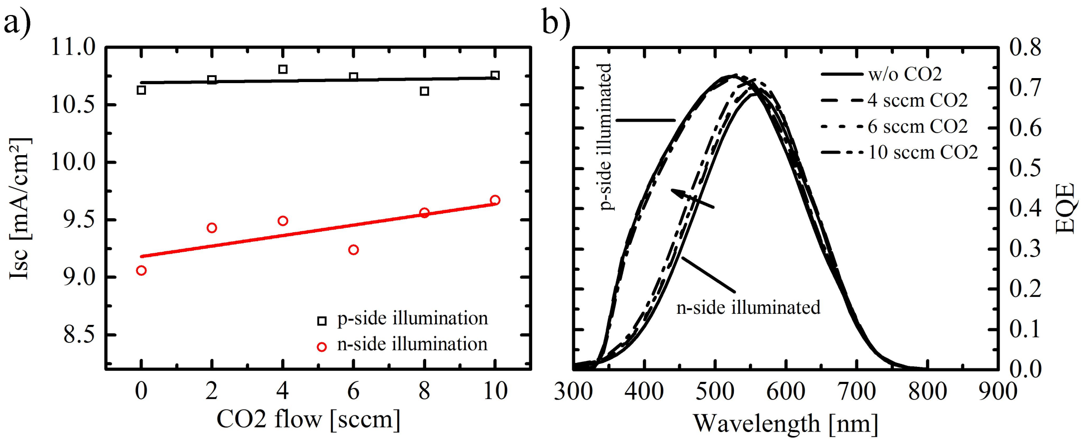

Figure 5.9: a): Short circuit current density of amorphous single junction cells with oxygenated n-layers. Lines are fits of the measurement points. b): External quantum efficiency measurement of bifacial amorphous single junction cells with CO_2 doping in the n-layer. The arrow indicates the tendency.

is measured and the results are depicted in figure 5.9b). The reflectance does not change measurably for all samples because the surface reflection can be attributed to the ITO and glas layer, which are the same for all depositions. This is proven in figure 5.12b), where the reflectance is plotted for the measured EQE range. Since only the n-layer is changed from deposition to deposition, the EQE measurements from the n-side are actually equal to transmission measurements with the i-layer functioning as a detector.

While the addition of CO_2 to the n-layer does not change the behavior, a distinct increase of conversion efficiency in the wavelength area between 400 and 600 nm can be observed (indicated by the arrow) when the cells are illuminated from the n-side. This can be attributed to the increased transparency due to the incorporation of oxygen and/or carbon into the layer. V_{oc} is not affected by the variation and remains nearly constant at an average of 920 mV for p-side illumination and 900 for n-side illumination.

5.4.2 Thickness Variation

Besides mixing the n-layer deposition gas with CO_2 to increase its transparency, a thickness variation without the addition of CO_2 to the n-layer is performed to investigate the influence of the n-layer thickness on the absorption behavior, cell efficiency, and the bifaciality. The standard p-layer used in the cells is between 5 to 10 nm thick, whereas the default n-layer is 20 to 30 nm thick to ensure a strong built in field for the improved carrier extraction and the homogeneity of the field.

Figure 5.10a) depicts the V_{oc} values of the series, proving that the used n-layer of approximately 10 nm is thick enough to conserve the strong built in field. As shown in figure 5.10b), the decreasing thickness of the n-layer does not influence the current generation density when the cell is illuminated from the p-side. In case of the illumination from the n-side, an increase in J_{sc} generation can be observed, reaching a short circuit current generation bifaciality value of 96 % for the cell with an n-layer of approximately 10 nm thickness.

As demonstrated in figure 5.10c), the additional current generated originates from the short wavelength regime. Compared to the CO_2 variation and the doping gas variation, the thickness variation shows the highest impact on the transparency for small wavelength. The observed improvement in conversion efficiency for light from the high energy regime is caused by a reduced absorption in the n-layer. Light absorbed in the n-layer does not contribute to the photocurrent. By reducing the thickness, more high energy light passes the n-layer to reach the i-layer where it is absorbed and converted into photocurrent.

5.4.3 Doping Variation

Because a variation of the thickness of the n-layer might reduce the strength of the built-in field generated by the phosphorus doping, the bifacial a-Si:H cells are doped with an increasing amount of phosphine (PH_3) doping gas. For the sake of a better comparability to the other experiments, the same n-layer as in section 5.4.2 is used.

The results of the doping variation are depicted in figure 5.11. With n-side illumination, an increase in the short circuit current density of 0.4 mA/cm2 can be seen when an additional gas flow of 5 sccm is added to the deposition gas mixture. The short circuit current when illuminated form the p-side does not show such a relation.

The V_{oc} is not affected by the variation and remains constant at an average of 925 mV for p-side illumination and 900 for n-side illumination, respectively. This asymmetric behavior is in good accordance with theory: The built in field of amorphous silicon thin-film cells largely originates from the boundary between i-layer and adjacent doped layer. Free charge carriers excited by absorption of light at the i-layer are forced towards the contacts by the built in field (p for holes, n for electrons). Because of their lower mobility, free holes have a higher recombination probability in the i-layer compared to electrons [7: pp. 192].

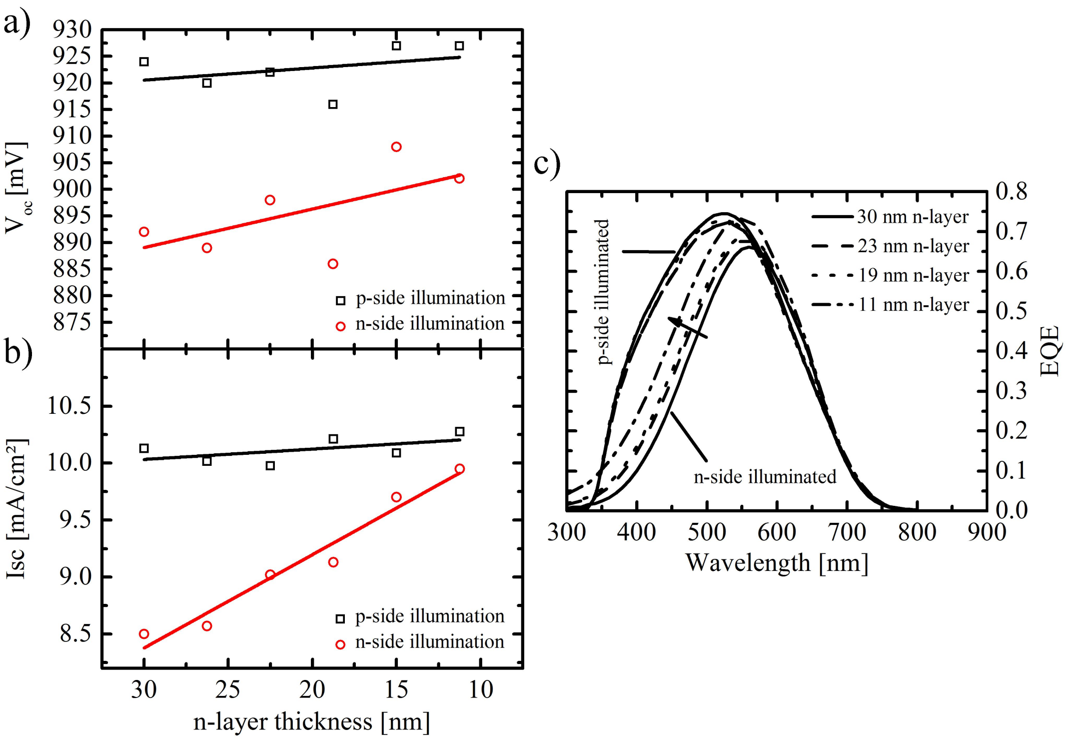

Figure 5.10: a): V_{oc} values of bifacial amorphous single junction cells with decreased n-layer thickness. Lines are fits of the measurement points. b): J_{sc} values of bifacial amorphous single junction cells with decreased n-layer thickness. Lines are fits of the measurement points. c): EQE measurement values of bifacial a-Si:H with reduced n-layer thickness. The arrow indicates the tendency.

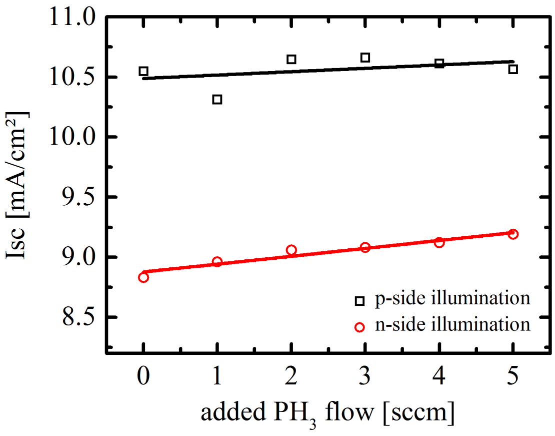

Figure 5.11: Short circuit current density of bifacial amorphous single junction cells with increased doping gas flow. Lines are fits of the measurement points.

This is why conventional a-Si:H modules are built in superstrat configuration, where the light enters the cell through the p-layer and the high density of exited holes on the first few nanometers can reach the contact before recombining.
The depicted n-doping increase in figure 5.11 influences mainly the hole transport in the area of the n-i junction. This is why only the short circuit current generation under n-side illumination increases. A faster excited charge transport has the additional benefit of removing the holes faster from the area where the highest concentration of free carriers is located in case of illumination from the n-side. This improved charge separation behavior and therefore reduced recombination probability results in an improved FF for the cells in this variation.

5.4.4 Combination of Variations

The reference cell at the start of the investigations had a bifaciality in short circuit current generation of only 77 %. Due to a combination of the discussed improvements, a bifacial amorphous single junction cell with improved bifaciality could be fabricated. This cell incorporates a 40 % thinner n-layer, an increased PH_3 and CO_2 deposition gas flow rate, and was deposited on rough etched commercial ZnO:Al substrates. With this n-layer, a bifaciality of 98 % for short circuit current density and 99 % for open circuit voltage could be reached.
The EQE in figure 5.12a) depicts the spectra of the optimized and the reference cell. The optimization leads to an increased conversion efficiency up to a wavelength of 650 nm when illuminated from the n-side while maintaining the performance when illuminated from the p-side.
The increase of conversion efficiency due to the increased performance of the n-layer can be attributed solely to an increase in transparency because the reflection does not change (figure 5.12b)) in the wavelength range from 300 to 650 nm where the improvement in the EQE are visible. The electrical characteristics of the produced cells are depicted in table 5.2. When looking at the improvement of light scattering through a rough TCO [7: pp. 317] in the monofacial reference cells, an increase of 0.6 mA/cm^2 is visible for J_{sc}. This improvement is mitigated by the higher FF of the cell on a flat TCO. It is therefore possible to reach the same power generation with flat TCO which would reduce the LCOE of the solar cells since the industry would require one less processing step, not needing to texture the TCO.
Turning a monofacial solar cell into a bifacial solar cell has a similar result: The J_{sc} drops because of the light lost due to the missing back reflector while the FF

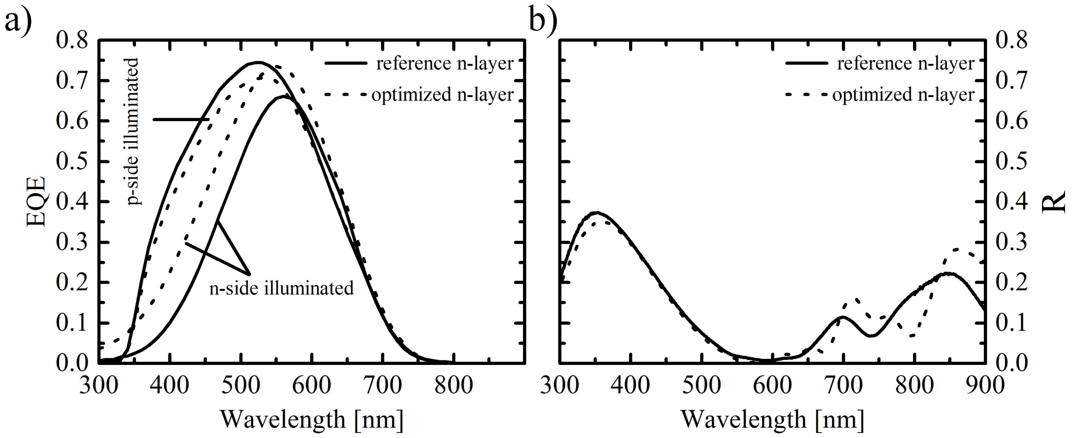

Figure 5.12: a): External quantum efficiency measurements of bifacial amorphous single junction cells with reference and optimized n-layer. b): Reflectance measurement of the same cells from the n-side.

	$J_{sc}\left[mA/cm^2\right]$	V_{oc}[mV]	FF[%]	η[%]
Ref, mono, rough, p	11.7	929	65	7.0
Ref, mono, flat, p	11.1	922	69	7.0
Ref, bif, rough, p/n	11.1/8.5	914/895	75/67	7.6/5.1
Opt, bif, rough, p/n	10.5/10.3	912/905	78/69	7.4/6.4

Table 5.2: Exemplary electrical values for the reference and optimized bifacial solar cells at STC. Illumination is indicated by mono for monofacial or bif for bifacial illumination. In order to compare textured and flat TCO the type is also indicated by rough or flat. Illumination direction is indicated by p for illumination through the p-layer and n for illumination through the n-layer.

improves. The bifacial cell illuminated from the n-layer has a slightly lower FF because of the lower hole mobility mentioned in section 5.4.3. Since the deposition time of the final n-layer is less than half of the deposition time of the reference layer and the only additional gas is cheap CO_2, the new n-layer would cost even less in industrial production than the reference n-layer.

The cells shown here are not optimized and only demonstrate the way in which the bifaciality of a single junction silicon thin film solar cell can be improved. With ARC, optimized cell stack, and state-of-the-art front and back contact, the bifacial single junction cells could reach high efficiencies of up to 10 % for both sides.

5.5 Conclusion

A lot of people have taken interest in bifacial solar cells. Different standards and applications are being developed to enable the comparability of all activities on bifacial solar power generation. Depending on the intended purpose, a big benefit can be achieved without an increase in production costs, lowering the cost for shading elements with solar for example.

Simulating the irradiance on different planes, it was demonstrated that bifacial modules in freestanding vertical installation face more irradiance than monofacial modules in optimum tilt and orientation, regardless of the modules facing east-west or north-south. The only solar modules feasible for bifaciality are single-junction solar cells because the current matching of multi-junction bifacial modules cannot be maintained under shifting illumination conditions. It could be shown that a slight tuning of the n-layer of a standard amorphous single junction cell in combination with the removal of the reflecting layer (Ag/white light reflector) can produce a cell with a bifaciality of 98 %.

The improved bifacial amorphous single junction solar cells show the same efficiency as the conventional cells under STC. Due to their bifacial nature this could lead to twice the output power generated under optimum conditions. They could reach approximately 40 % to 70 % improved power generation in a yearly average compared to monofacial solar cells under real life conditions.

To sum up this chapter, bifaciality is the difference (percentage) in performance of a solar cell depending on illumination from the front and back side. There are no standards for measuring yet, although the community is addressing the problem.

Even in northern Germany, bifacial solar cells in vertical installation are able to generate more power than conventionally installed monofacial modules. Using bifacial solar cells in vertical installation could shift the power generation peaks to the morning and evening hours of day and to the winter months of the year.

The bifaciality of amorphous single-junction thin-film solar cells can be increased by modifying the n-layer for greater transparency of blue light by reducing its thickness and using oxygen in the deposition process.

6

Summary and Outlook

The growing amount of installed photovoltaic power and the resulting increased effort to create more building integrated projects with photovoltaic creates a demand for versatile and novel solar technology. This work shows that thin-film silicon solar cells can be a prime candidate for many BIPV applications.

Homogeneous esthetics and a tunable transparency are only two of its advantages over many competing solar cell technologies. The investigation of doped silicon oxide layers in this work shows that they can improve thin-film silicon solar cells for BIPV applications by increasing transparency of those layers and therefore reducing parasitic absorption. They have to be stabilized in order to work long term because they degrade over time. This can be achieved by inserting thin SiO_2 atom diffusion barrier layers into the stack. These SiO_2 atom diffusion barrier layers can be made transparent for charge carriers if they are sufficiently thin enough to be tunneled through.

In order to reduce the production time of single- and tandem-junction cells for BIPV applications, the absorption of the silicon absorber material can be enhanced by adding germanium. The trick is to use the high absorption of germanium and the advantages of a band-gap reduced by the addition of germanium to enable the absorption of light with a longer wavelength. μc-$Si_{1\text{-}X}Ge_X$:H absorbers were investigated showing the same efficiency as the μc-Si:H absorbers but with reduced thickness. Although germane is more expensive than silane, the increased throughput would reduce the costs for manufacturers producing multi-junction silicon thin-film BIPV products.

An example of a special BIPV product was investigated in this project: For certain applications like fences and noise-barriers, it can be very advantageous for a photovoltaic module to be able to collect sunlight from both sides. These types of modules are called bifacial modules. Different planes of orientation and tilt were simulated in terms of irradiance for bifacial modules. It was found that even for Oldenburg, vertical installed and free standing modules with high bifaciality can receive more irradiance than monofacial modules with optimum tilt and orientation because the irradiance profile in Germany includes more indirect light than direct light. This is irrespective of the orientation of the vertical and bifacial module. The east-west orientation of the vertical modules can shift the generation profile of each day to the early and late hours of day, matching the demand profile better than conventionally installed modules. North-south orientation of the modules can shift the yearly generation profile to the winter month because of the very low standing sun.

Since there are no bifacial thin-film silicon modules available on the market, a way to turn single-junction monofacial modules into bifacial modules with high bifaciality was investigated. A focus was set on single-junciton modules because tandem-junction thin-film silicon solar cells are disadvantaged by the current matching problem of shifting irradiation conditions. It was found that a bifaciality of over 95 % can be achieved for single junction cells by redesigning the n-layer for high energy light transparency. This can be done by reducing its thickness and increasing the transparency by alloying the material with carbon and oxygen. As a result, a tunable semi transparent bifacial solar module perfect for many BIPV applications and especially vertical installation in noise barriers and fences is produced.

On the scientific side, bifacial thin-film solar cells are a research topic that could be investigated further. For example, illuminating a cell from both sides simultaneously changes the charge carrier concentration distribution drastically compared to a monofacial cell. Results from a deep understanding of the changed concentration profile could be used to further increase the bifaciality of these cells.

Combining the improvements to the transparency of the doped layers from Chapter 3 with the advanced absorber material from Chapter 4 and an intelligent and modular laser pattering scheme should be tested next in order to create a highly efficient but modular product for BIPV applications. Customizable shapes are one of the key requirements for BIPV products.

The next steps could be using the steps described in the last chapter to create some larger scale prototypes of these bifacial thin-film silicon modules. These could then be installed on a noise barrier near to a train track or a highway to be tested in terms of performance, self-cleaning, and shading resistance. Judging by the publicity generated by the solar road described in section 1, this can also be used to raise public awareness of BIPV and might even convince the government to order all new noise barriers build in Germany to incorporate photovoltaic. This would be far more effective than using the photovoltaic as road material because the irradiance on the area is higher and cleaning and traction are not a problem.

Bibliography

[1] "global-solar-demand-monitor-q1-2018, Accessed 20.06.2018." [Online]. Available: https://www.greentechmedia.com/research/report/global-solar-demand-monitor-q1-2018

[2] "Gigafactory Rooftop Array, Accessed 20.06.2018." [Online]. Available: https://www.ecowatch.com/tesla-solar-gigafactory-2543158034.html

[3] F. MACDONALD, "The solar road in the Netherlands is working even better than expected, Accessed 15.07.2016," 2015. [Online]. Available: http://www.sciencealert.com/solar-roads-in-the-netherlands-are-working-even-better-than-expected

[4] F. Guerrini, "France Wants To Install 1,000 Km Of Solar Roadways Over The Next Five Years, Accessed 15.07.2016," 2016. [Online]. Available: http://www.forbes.com/sites/federicoguerrini/2016/02/07/france-wants-to-install-1000-km-of-solar-roadways-over-the-next-five-years/

[5] P. Capezzuto and A. Madan, *Plasma deposition of amorphous silicon-based materials.* Academic Press, 1995. [Online]. Available: https://books.google.de/books?hl=de&lr=&id=kIMVkF8Emu0C&oi=fnd&pg=PP2&dq=Plasma+Deposition+of+Amorphous+Silicon-+Based+Materials.+Plasma-Materials+Interactions.&ots=zlWzVmchPy&sig=4XFr5hzhZoruqG_3nwswEUFYC9g

[6] R. Caballero, C. Kaufmann, T. Eisenbarth, M. Cancela, R. Hesse, T. Unold, A. Eicke, R. Klenk, and H. Schock, "The influence of Na on low temperature growth of CIGS thin film solar cells on polyimide substrates," *Thin Solid Films*, vol. 517, no. 7, pp. 2187–2190, 2009. [Online]. Available: http://dx.doi.org/10.1016/j.tsf.2008.10.085

[7] A. Shah, *Thin-Film Silicon Solar Cells.* EPFL Press, 2010. [Online]. Available: https://books.google.com/books?hl=de&lr=&id=DBSkX6w0rFMC&pgis=1

[8] A. Araújo, R. Barros, T. Mateus, D. Gaspar, N. Neves, A. Vicente, S. A. Filonovich, P. Barquinha, E. Fortunato, A. M. Ferraria, A. M. Botelho do Rego, A. Bicho, H. Águas, and R. Martins, "Role of a disperse carbon interlayer on the performances of tandem a-Si solar cells," *Science and Technology of Advanced Materials*, vol. 14, no. 4, p. 045009, mar 2013. [Online]. Available: http://www.tandfonline.com/doi/full/10.1088/1468-6996/14/4/045009

[9] M. Vukadinovic, F. Smole, M. Topic, R. E. I. Schropp, and F. A. Rubinelli, "Transport in tunneling recombination junctions: A combined computer simulation study," *Journal of Applied Physics*, vol. 96, no. 12, p. 7289, dec 2004. [Online]. Available: http://scitation.aip.org/content/aip/journal/jap/96/12/10.1063/1.1811375

[10] F. M. Smits, "Measurement of Sheet Resistivities with the Four-Point Probe," *Bell System Technical Journal*, vol. 37, no. 3, pp. 711–718, may 1958. [Online]. Available: http://ieeexplore.ieee.org/lpdocs/epic03/wrapper.htm?arnumber=6773368

[11] U. Kräling, G. Baarah, G. Dülger, and A. Schmid, "IV Measurement of Bifacial Modules: Bifacial vs. Monofacial Illumination," *33rd European Photovoltaic Solar Energy Conference and Exhibition*, pp. 1624–1627, 2017. [Online]. Available: https://www.ise.fraunhofer.de/content/dam/ise/de/documents/publications/conference-paper/33-eupvsec-2017/Schmid_5BV432.pdf

[12] M. Stuckelberger, M. Despeisse, G. Bugnon, J.-W. Schüttauf, F.-J. Haug, and C. Ballif, "Comparison of amorphous silicon absorber materials: Light-induced degradation and solar cell efficiency," *Journal of Applied Physics*, vol. 114, no. 15, p. 154509, oct 2013. [Online]. Available: http://scitation.aip.org/content/aip/journal/jap/114/15/10.1063/1.4824813

[13] D. L. Staebler and C. R. Wronski, "Reversible conductivity changes in discharge-produced amorphous Si," *Applied Physics Letters*, vol. 31, no. 4, p. 292, aug 1977. [Online]. Available: http://scitation.aip.org/content/aip/journal/apl/31/4/10.1063/1.89674

[14] R. Tsu, "Critical volume fraction of crystallinity for conductivity percolation in phosphorus-doped Si:F:H alloys," *Applied Physics Letters*, vol. 40, no. 6, p. 534, mar 1982. [Online]. Available: http://scitation.aip.org/content/aip/journal/apl/40/6/10.1063/1.93133

[15] E. Bustarret, M. A. Hachicha, and M. Brunel, "Experimental determination of the nanocrystalline volume fraction in silicon thin films from Raman spectroscopy," *Applied Physics Letters*, vol. 52, no. 20, p. 1675, may 1988. [Online]. Available: http://scitation.aip.org/content/aip/journal/apl/52/20/10.1063/1.99054

[16] O. Pagès, J. Souhabi, V. J. B. Torres, A. V. Postnikov, and K. C. Rustagi, "Re-examination of the SiGe Raman spectra: Percolation/one-dimensional-cluster scheme and ab initio calculations," *Physical Review B*, vol. 86, no. 4, p. 045201, jul 2012. [Online]. Available: http://journals.aps.org/prb/abstract/10.1103/PhysRevB.86.045201

[17] M. N. Islam and S. Kumar, "Influence of crystallite size distribution on the micro-Raman analysis of porous Si," *Applied Physics Letters*, vol. 78, no. 6, p. 715, feb 2001. [Online]. Available: http://scitation.aip.org/content/aip/journal/apl/78/6/10.1063/1.1343494

[18] H. Xia, Y. L. He, L. C. Wang, W. Zhang, X. N. Liu, X. K. Zhang, D. Feng, and H. E. Jackson, "Phonon mode study of Si nanocrystals using micro-Raman spectroscopy," *Journal of Applied Physics*, vol. 78, no. 11, p. 6705, dec 1995. [Online]. Available: http://scitation.aip.org/content/aip/journal/jap/78/11/10.1063/1.360494

[19] M. Krause, "Materialien und Bauelemente auf der Basis von mikrokristallinen SiGe:H und amorphen SiC:H Legierungen - Detektion des nahen infraroten und ultravioletten Spektralbereichs," Ph.D. dissertation, Heinrich-Heine-Universität Düsseldorf, 2007. [Online]. Available: http://docserv.uni-duesseldorf.de/servlets/DocumentServlet?id=2182

[20] M. I. Alonso and K. Winer, "Raman spectra of c-SiGe alloys," *Physical Review B*, vol. 39, no. 14, pp. 10 056–10 062, may 1989. [Online]. Available: http://journals.aps.org/prb/abstract/10.1103/PhysRevB.39.10056

[21] C.-W. Chang, M.-H. Hong, W.-F. Lee, K.-C. Lee, S.-M. Yang, M.-S. Tsai, Y. Chuang, Y.-T. Fan, N. Hasuike, H. Harima, T. Ueda, T. Ishigaki, K. Kang, and W. S. Yoo, "In-line Si1-xGex epitaxial process monitoring and diagnostics using multiwavelength high resolution micro-Raman spectroscopy," *AIP Advances*, vol. 2, no. 2, p. 022117, apr 2012. [Online]. Available: http://scitation.aip.org/content/aip/journal/adva/2/2/10.1063/1.4711043

[22] J. C. Tsang, P. M. Mooney, F. Dacol, and J. O. Chu, “Measurements of alloy composition and strain in thin GeSi layers,” *Journal of Applied Physics*, vol. 75, no. 12, p. 8098, jun 1994. [Online]. Available: http://scitation.aip.org/content/aip/journal/jap/75/12/10.1063/1.356554

[23] T. S. Perova, J. Wasyluk, K. Lyutovich, E. Kasper, M. Oehme, K. Rode, and A. Waldron, “Composition and strain in thin SiGe virtual substrates measured by micro Raman spectroscopy and x ray diffraction,” *Journal of Applied Physics*, vol. 109, no. 3, p. 033502, feb 2011. [Online]. Available: http://scitation.aip.org/content/aip/journal/jap/109/3/10.1063/1.3536508

[24] A. Alvarez-Toral, P. Sanchez, A. Menéndez, R. Pereiro, A. Sanz-Medel, and B. Fernández, “Depth Profile Analysis of Amorphous Silicon Thin Film Solar Cells by Pulsed Radiofrequency Glow Discharge Time of Flight Mass Spectrometry.” *Journal of the American Society for Mass Spectrometry*, 2014. [Online]. Available: http://www.ncbi.nlm.nih.gov/pubmed/25404156

[25] L. Lobo, B. Fernandez, R. Pereiro, N. Bordel, E. Demenev, D. Giubertoni, M. Bersani, P. Honicke, B. Beckhoff, and A. Sanz-Medel, “Quantitative depth profiling of boron and arsenic ultra low energy implants by pulsed rf-GD-ToFMS,” *J. Anal. At. Spectrom.*, vol. 26, no. 3, pp. 542–549, 2011. [Online]. Available: http://xlink.rsc.org/?DOI=C0JA00197J

[26] S. Müller and J. Remund, “Solar Radiation and Uncertainty Information of Meteonorm 7,” *26th European Photovoltaic Solar Energy Conference and Exhibition*, pp. 4388–4390, oct 2011. [Online]. Available: http://www.eupvsec-proceedings.com/proceedings?paper=13317

[27] A. Zelenka, G. Czeplak, and V. D’Agostino, “Techniques for supplementing solar radiation network data,” *Report IEA Task*, 1992. [Online]. Available: http://archive.iea-shc.org/publications/downloads/Task9_Vol1_Sept1992.pdf

[28] L. Wald and M. Lefèvre, “Interpolation schemes-Profile Method (a process-based distance for interpolation schemes),” *SoDa Deliverable D5-1-1. Internal document*, 2001. [Online]. Available: https://hal.archives-ouvertes.fr/hal-00465570/document

[29] R. Aguiar, M. Collares-Pereira, and J. Conde, “Simple procedure for generating sequences of daily radiation values using a library of Markov transition

matrices," *Solar Energy*, vol. 40, no. 3, pp. 269–279, 1988. [Online]. Available: http://www.sciencedirect.com/science/article/pii/0038092X88900497

[30] R. Perez, R. Seals, P. Ineichen, R. Stewart, and D. Menicucci, "A new simplified version of the perez diffuse irradiance model for tilted surfaces," *Solar Energy*, vol. 39, no. 3, pp. 221–231, 1987. [Online]. Available: http://www.sciencedirect.com/science/article/pii/S0038092X87800312

[31] Meteonorm. Accessed 2016-02-04., "Einstrahlungsdaten für jeden Ort des Planeten." [Online]. Available: http://www.meteonorm.com/

[32] B. Fernandez, L. Lobo, N. Reininghaus, R. Pereiro, and A. Sanz-Medel, "Characterization of thin film tandem solar cells by radiofrequency pulsed glow discharge – Time of flight mass spectrometry," *Talanta*, vol. 165, pp. 289–296, 2017.

[33] J. Poortmans and V. Arkhipov, *Thin Film Solar Cells: Fabrication, Characterization and Applications.* John Wiley & Sons, 2006. [Online]. Available: https://books.google.com/books?id=SvVYBK6YAxAC&pgis=1

[34] S. Schicho, D. Hrunski, R. van Aubel, and A. Gordijn, "High potential of thin a-Si: H/muc-Si:H tandem solar cells," *Progress in Photovoltaics: Research and Applications*, vol. 18, no. 2, pp. 83–89, mar 2010. [Online]. Available: http://doi.wiley.com/10.1002/pip.929

[35] J. Müller, B. Rech, J. Springer, and M. Vanecek, "TCO and light trapping in silicon thin film solar cells," *Solar Energy*, vol. 77, no. 6, pp. 917–930, 2004.

[36] K. Chakanga, O. Siepmann, O. Sergeev, S. Geißendörfer, K. von Maydell, and C. Agert, "Laser textured substrates for light in-coupling in thin-film solar cells," *Journal of Photonics for Energy*, vol. 4, no. 1, p. 044598, oct 2014. [Online]. Available: http://photonicsforenergy.spiedigitallibrary.org/article.aspx?articleid=1915164

[37] M. Berginski, J. Hüpkes, M. Schulte, G. Schöpe, H. Stiebig, B. Rech, and M. Wuttig, "The effect of front ZnO:Al surface texture and optical transparency on efficient light trapping in silicon thin-film solar cells," *Journal of Applied Physics*, vol. 101, no. 7, p. 074903, apr 2007. [Online]. Available: http://scitation.aip.org/content/aip/journal/jap/101/7/10.1063/1.2715554

[38] M. Kambe, T. Matsui, H. Sai, N. Taneda, K. Masumo, A. Takahashi, T. Ikeda, T. Oyama, M. Kondo, and K. Sato, "Improved light-trapping effect in a-Si:H muC-Si:H tandem solar cells by using high haze SnO2:F thin films," in *2009 34th IEEE Photovoltaic Specialists Conference (PVSC)*. IEEE, jun 2009, pp. 001 663–001 666. [Online]. Available: http://ieeexplore.ieee.org/lpdocs/epic03/wrapper.htm?arnumber=5411411

[39] J. Springer, "Light trapping and optical losses in microcrystalline silicon pin solar cells deposited on surface-textured glass/ZnO substrates," *Solar Energy Materials and Solar Cells*, vol. 85, no. 1, pp. 1–11, apr 2004. [Online]. Available: http://www.sciencedirect.com/science/article/pii/S0927024804001175

[40] M. Theuring, M. Vehse, K. von Maydell, and C. Agert, "AZO-Ag-AZO transparent electrode for amorphous silicon solar cells," *Thin Solid Films*, vol. 558, pp. 294–297, may 2014. [Online]. Available: http://linkinghub.elsevier.com/retrieve/pii/S0040609014001771

[41] M. Theuring, V. Steenhoff, S. Geißendörfer, M. Vehse, K. von Maydell, and C. Agert, "Laser perforated ultrathin metal films for transparent electrode applications," *Optics Express*, vol. 23, no. 7, p. A254, apr 2015. [Online]. Available: https://www.osapublishing.org/abstract.cfm?URI=oe-23-7-A254

[42] C. Kothandaraman, T. Tonon, C. Huang, and A. E. Delahoy, "Improvement of a-Si:H P-I-N Devices using Zinc Oxide based Back-Reflectors," *MRS Proceedings*, vol. 219, p. 475, feb 2011. [Online]. Available: http://journals.cambridge.org/abstract_S1946427400397044

[43] O. Vetterl, F. Finger, R. Carius, P. Hapke, L. Houben, O. Kluth, A. Lambertz, A. Mück, B. Rech, and H. Wagner, "Intrinsic microcrystalline silicon: A new material for photovoltaics," *Solar Energy Materials and Solar Cells*, vol. 62, no. 1-2, pp. 97–108, apr 2000. [Online]. Available: http://www.sciencedirect.com/science/article/pii/S0927024899001403

[44] P. Cuony, M. Marending, D. T. L. Alexander, M. Boccard, G. Bugnon, M. Despeisse, and C. Ballif, "Mixed-phase p-type silicon oxide containing silicon nanocrystals and its role in thin-film silicon solar cells," *Applied Physics Letters*, vol. 97, no. 21, p. 213502, 2010. [Online]. Available: http://link.aip.org/link/APPLAB/v97/i21/p213502/s1&Agg=doi

[45] P. Cuony, D. T. Alexander, L. Löfgren, M. Krumrey, M. Marending, M. Despeisse, and C. Ballif, "Mixed phase silicon oxide layers for thin-film silicon solar cells," *MRS Proceedings*, vol. 1321, pp. mrss11–1321–a12–02, jun 2011. [Online]. Available: http://journals.cambridge.org/abstract_S194642741100813X

[46] P. Buehlmann, J. Bailat, D. Dominé, A. Billet, F. Meillaud, A. Feltrin, and C. Ballif, "In situ silicon oxide based intermediate reflector for thin film silicon micromorph solar cells," *Applied Physics Letters*, vol. 91, no. 14, p. 143505, 2007. [Online]. Available: http://link.aip.org/link/APPLAB/v91/i14/p143505/s1&Agg=doi

[47] S. Fahr, C. Rockstuhl, and F. Lederer, "The interplay of intermediate reflectors and randomly textured surfaces in tandem solar cells," *Applied Physics Letters*, vol. 97, no. 17, p. 173510, 2010. [Online]. Available: http://link.aip.org/link/APPLAB/v97/i17/p173510/s1&Agg=doi

[48] P. D. Veneri, L. V. Mercaldo, and I. Usatii, "Improved micromorph solar cells by means of mixed-phase n-doped silicon oxide layers," *Progress in Photovoltaics: Research and Applications*, vol. 21, no. 2, pp. 148–155, mar 2011. [Online]. Available: http://doi.wiley.com/10.1002/pip.1168

[49] X. Zhang, Q. Yue, X. Zheng, X. Geng, and Y. Zhao, "Plasma deposition of n-SiOx nanocrystalline thin film for enhancing the performance of silicon thin film solar cells," *Thin Solid Films*, vol. 520, no. 2, pp. 684–688, nov 2011. [Online]. Available: http://linkinghub.elsevier.com/retrieve/pii/S0040609011013459

[50] B. Yan, G. Yue, L. Sivec, J. Yang, S. Guha, and C.-S. Jiang, "Innovative dual function nc-SiOx:H layer leading to a 16% efficient multi-junction thin-film silicon solar cell," *Applied Physics Letters*, vol. 99, no. 11, p. 113512, 2011. [Online]. Available: http://link.aip.org/link/APPLAB/v99/i11/p113512/s1&Agg=doi

[51] H. Sai, K. Maejima, T. Matsui, T. Koida, M. Kondo, S. Nakao, Y. Takeuchi, H. Katayama, and I. Yoshida, "High-efficiency microcrystalline silicon solar cells on honeycomb textured substrates grown with high-rate VHF plasma-enhanced chemical vapor deposition," *Japanese Journal of Applied Physics*, vol. 54, no. 8S1, p. 08KB05, aug 2015. [Online]. Available: http://iopscience.iop.org/article/10.7567/JJAP.54.08KB05

[52] V. Smirnov, W. Böttler, A. Lambertz, H. Wang, R. Carius, and F. Finger, "Microcrystalline silicon n-i-p solar cells prepared with microcrystalline silicon oxide (uc-SiO x :H) n-layer," *Physica Status Solidi (C)*, vol. 1056, no. 3, pp. NA–NA, feb 2010. [Online]. Available: http://doi.wiley.com/10.1002/pssc.200982830

[53] P. Delli Veneri, L. V. Mercaldo, and I. Usatii, "Silicon oxide based n-doped layer for improved performance of thin film silicon solar cells," *Applied Physics Letters*, vol. 97, no. 2, p. 023512, jul 2010. [Online]. Available: http://scitation.aip.org/content/aip/journal/apl/97/2/10.1063/1.3463457

[54] J. Springer, "Absorption loss at nanorough silver back reflector of thin-film silicon solar cells," *Journal of Applied Physics*, vol. 95, no. 3, p. 1427, jan 2004. [Online]. Available: http://scitation.aip.org/content/aip/journal/jap/95/3/10.1063/1.1633652

[55] S. Y. Myong and L. S. Jeon, "Improved light trapping in thin-film silicon solar cells via alternated n-type silicon oxide reflectors," *Solar Energy Materials and Solar Cells*, vol. 119, pp. 77–83, dec 2013. [Online]. Available: http://www.sciencedirect.com/science/article/pii/S0927024813002547

[56] V. Smirnov, a. Lambertz, and F. Finger, "Bifacial microcrystalline silicon solar cells with improved performance due to μc-SiO x :H doped layers 1," *Canadian Journal of Physics*, vol. 92, no. 7/8, pp. 913–916, 2014. [Online]. Available: http://www.nrcresearchpress.com/doi/abs/10.1139/cjp-2013-0617

[57] P. Cuony, D. T. L. Alexander, I. Perez-Wurfl, M. Despeisse, G. Bugnon, M. Boccard, T. Söderström, A. Hessler-Wyser, C. Hébert, and C. Ballif, "Silicon filaments in silicon oxide for next-generation photovoltaics." *Advanced materials (Deerfield Beach, Fla.)*, vol. 24, no. 9, pp. 1182–6, mar 2012. [Online]. Available: http://www.ncbi.nlm.nih.gov/pubmed/22290779

[58] M. Despeisse, G. Bugnon, A. Feltrin, M. Stueckelberger, P. Cuony, F. Meillaud, A. Billet, and C. Ballif, "Resistive interlayer for improved performance of thin film silicon solar cells on highly textured substrate," *Applied Physics Letters*, vol. 96, no. 7, p. 073507, feb 2010. [Online]. Available: http://scitation.aip.org/content/aip/journal/apl/96/7/10.1063/1.3324704

[59] F.-J. Haug and C. Ballif, "Light management in thin film silicon solar cells,"

Energy Environ. Sci., vol. 8, no. 3, pp. 824–837, 2015. [Online]. Available: http://xlink.rsc.org/?DOI=C4EE03346A

[60] F. Finger, O. Astakhov, T. Bronger, R. Carius, T. Chen, A. Dasgupta, A. Gordijn, L. Houben, Y. Huang, S. Klein, M. Luysberg, H. Wang, and L. Xiao, "Microcrystalline silicon carbide alloys prepared with HWCVD as highly transparent and conductive window layers for thin film solar cells," *Thin Solid Films*, vol. 517, no. 12, pp. 3507–3512, apr 2009. [Online]. Available: http://www.sciencedirect.com/science/article/pii/S0040609009000571

[61] P. Roca i Cabarrocas, N. Layadi, T. Heitz, B. Drevillon, and I. Solomon, "Substrate selectivity in the formation of microcrystalline silicon: Mechanisms and technological consequences," *Applied Physics Letters*, vol. 66, no. 26, p. 3609, jun 1995. [Online]. Available: http://scitation.aip.org/content/aip/journal/apl/66/26/10.1063/1.113803

[62] T. Grundler, A. Lambertz, and F. Finger, "N-type hydrogenated amorphous silicon oxide containing a microcrystalline silicon phase as an intermediate reflector in silicon thin film solar cells," *Physica Status Solidi (C)*, vol. 7, no. 3-4, pp. 1085–1088, mar 2010. [Online]. Available: http://doi.wiley.com/10.1002/pssc.200982872

[63] M. Fukawa, S. Suzuki, L. Guo, M. Kondo, and A. Matsuda, "High rate growth of microcrystalline silicon using a high-pressure depletion method with VHF plasma," *Solar Energy Materials and Solar Cells*, vol. 66, no. 1-4, pp. 217–223, feb 2001. [Online]. Available: http://www.sciencedirect.com/science/article/pii/S0927024800001768

[64] A. Gordijn, J. K. Rath, and R. E. I. Schropp, "High efficiency uc Si solar cells made by very high-frequency plasma enhanced chemical vapor deposition," *Progress in Photovoltaics: Research and Applications*, vol. 14, no. 4, pp. 305–311, jun 2006. [Online]. Available: http://doi.wiley.com/10.1002/pip.673

[65] T. S. Chu, R. Q. Zhang, and H. F. Cheung, "Geometric and Electronic Structures of Silicon Oxide Clusters," *J. Phys. Chem. B*, vol. 105, no. 9, pp. 1705–1709, 2001. [Online]. Available: http://pubs.acs.org/doi/abs/10.1021/jp002046k

[66] V. Smirnov, A. Lambertz, and F. Finger, "Application of p- and n-Type Microcrystalline Silicon Oxide (µc-SiOx:H) Alloys in Thin Film

Silicon Single and Tandem Junction Solar Cells," 2014. [Online]. Available: http://juser.fz-juelich.de/record/173140/?ln=de

[67] S. Suzuki, M. Kondo, and A. Matsuda, "Growth of device grade μc-Si film at over 50Å/s using PECVD," *Solar Energy Materials and Solar Cells*, vol. 74, no. 1-4, pp. 489–495, oct 2002. [Online]. Available: http://linkinghub.elsevier.com/retrieve/pii/S0927024802001071

[68] D. S. Perloff, "Four Point Sheet Resistance Measurements of Semiconductor Doping Uniformity," *Journal of The Electrochemical Society*, vol. 124, no. 4, p. 582, apr 1977. [Online]. Available: http://jes.ecsdl.org/content/124/4/582.abstract

[69] M. Berginski, J. Hüpkes, A. Gordijn, W. Reetz, T. Wätjen, B. Rech, and M. Wuttig, "Experimental studies and limitations of the light trapping and optical losses in microcrystalline silicon solar cells," *Solar Energy Materials and Solar Cells*, vol. 92, no. 9, pp. 1037–1042, sep 2008. [Online]. Available: http://linkinghub.elsevier.com/retrieve/pii/S0927024808001025

[70] L. Mercaldo, I. Usatii, E. Bobeico, F. Russo, L. Lancellotti, and P. D. Veneri, "Optical Performance of Ag-based Back Reflectors with different Spacers in Thin Film Si Solar Cells," *Energy Procedia*, vol. 84, no. April 2016, pp. 221–227, 2015. [Online]. Available: http://linkinghub.elsevier.com/retrieve/pii/S1876610215029823

[71] M. Boccard, C. Battaglia, S. Hänni, K. Söderström, J. Escarré, S. Nicolay, F. Meillaud, M. Despeisse, and C. Ballif, "Multiscale Transparent Electrode Architecture for Efficient Light Management and Carrier Collection in Solar Cells," *Nano Letters*, vol. 12, no. 3, pp. 1344–1348, mar 2012. [Online]. Available: http://pubs.acs.org/doi/abs/10.1021/nl203909u

[72] A. Dagamseh, B. Vet, F. Tichelaar, P. Suttac, and M. Zeman, "ZnO:Al films prepared by rf magnetron sputtering applied as back reflectors in thin-film silicon solar cells," *Thin Solid Films*, vol. 516, no. 21, pp. 7844–7850, 2008. [Online]. Available: https://www.sciencedirect.com/science/article/pii/S0040609008005452?via{%}253Dihub

[73] F. Rollert, N. A. Stolwijk, and H. Mehrer, "Solubility, diffusion and thermodynamic properties of silver in silicon," *Journal of Physics*

D: Applied Physics, vol. 20, no. 9, pp. 1148–1155, sep 1987. [Online]. Available: http://stacks.iop.org/0022-3727/20/i=9/a=010?key=crossref.797dbf22beb1fc42c20f17cee456043a

[74] Y. Wang, X. Geng, H. Stiebig, and F. Finger, "Stability of microcrystalline silicon solar cells with HWCVD buffer layer," *Thin Solid Films*, vol. 516, no. 5, pp. 733–735, 2008. [Online]. Available: http://www.sciencedirect.com/science/article/pii/S0040609007009637

[75] T. C. Nason, G.-R. Yang, K.-H. Park, and T.-M. Lu, "Study of silver diffusion into Si(111) and SiO2 at moderate temperatures," *Journal of Applied Physics*, vol. 70, no. 3, p. 1392, 1991. [Online]. Available: http://scitation.aip.org/content/aip/journal/jap/70/3/10.1063/1.349547

[76] G. Bugnon, G. Parascandolo, S. Hänni, M. Stuckelberger, M. Charrière, M. Despeisse, F. Meillaud, and C. Ballif, "Silicon oxide buffer layer at the p-i interface in amorphous and microcrystalline silicon solar cells," *Solar Energy Materials and Solar Cells*, vol. 120, no. PART A, pp. 143–150, 2014. [Online]. Available: http://dx.doi.org/10.1016/j.solmat.2013.08.034

[77] J. Fang, Z. Chen, N. Wang, L. Bai, G. Hou, X. Chen, C. Wei, G. Wang, J. Sun, Y. Zhao, and X. Zhang, "Improvement in performance of hydrogenated amorphous silicon solar cells with hydrogenated intrinsic amorphous silicon oxide p/i buffer layers," *Solar Energy Materials and Solar Cells*, vol. 128, pp. 394–398, 2014. [Online]. Available: http://dx.doi.org/10.1016/j.solmat.2014.06.012

[78] B. Brar, G. D. Wilk, and A. C. Seabaugh, "Direct extraction of the electron tunneling effective mass in ultrathin SiO2," *Applied Physics Letters*, vol. 69, no. 18, p. 2728, 1996. [Online]. Available: http://scitation.aip.org/content/aip/journal/apl/69/18/10.1063/1.117692

[79] P. Punchaipetch, K. Ichikawa, Y. Uraoka, T. Fuyuki, E. Takahashi, T. Hayashi, and K. Ogata, "Effect of SiO2 Tunnel Oxide Thickness on Electron Tunneling Mechanism in Si Nanocrystal Dots Floating-Gate Memories," *Japanese Journal of Applied Physics*, vol. 45, no. 5A, pp. 3997–3999, may 2006. [Online]. Available: http://stacks.iop.org/1347-4065/45/3997

[80] N. Reininghaus, M. Kellermann, K. von Maydell, and C. Agert, "Effects of process parameters on uc-SiGe:H solar cells performance and material

properties," *EPJ Photovoltaics*, vol. 6, p. 65301, feb 2015. [Online]. Available: http://www.epj-pv.org/10.1051/epjpv/2015002

[81] T. Matsui, A. Bidiville, K. Maejima, H. Sai, T. Koida, T. Suezaki, M. Matsumoto, K. Saito, I. Yoshida, and M. Kondo, "High-efficiency amorphous silicon solar cells: Impact of deposition rate on metastability," *Applied Physics Letters*, vol. 106, no. 5, 2015. [Online]. Available: http://dx.doi.org/10.1063/1.4907001

[82] B. Stannowski, O. Gabriel, S. Calnan, T. Frijnts, A. Heidelberg, S. Neubert, S. Kirner, S. Ring, M. Zelt, B. Rau, J.-H. Zollondz, H. Bloess, R. Schlatmann, and B. Rech, "Achievements and challenges in thin film silicon module production," *Solar Energy Materials and Solar Cells*, vol. 119, pp. 196–203, dec 2013. [Online]. Available: http://www.sciencedirect.com/science/article/pii/S0927024813003383

[83] P. Cuony, "Optical Layers for Thin-film Silicon Solar Cells," Ph.D. dissertation, EPFL, 2011. [Online]. Available: http://infoscience.epfl.ch/record/168644/files/EPFL_TH5190.pdf

[84] T. Matsui, M. Kondo, K. Ogata, T. Ozawa, and M. Isomura, "Influence of alloy composition on carrier transport and solar cell properties of hydrogenated microcrystalline silicon germanium thin films," *Applied Physics Letters*, vol. 89, no. 14, p. 142115, oct 2006. [Online]. Available: http://scitation.aip.org/content/aip/journal/apl/89/14/10.1063/1.2358318

[85] T. Matsui, H. Jia, and M. Kondo, "Thin film solar cells incorporating microcrystalline SiGe as efficient infrared absorber: an application to double junction tandem solar cells," *Progress in Photovoltaics: Research and Applications*, vol. 18, no. 1, pp. 48–53, jan 2010. [Online]. Available: http://doi.wiley.com/10.1002/pip.922

[86] J.-W. Schüttauf, B. Niesen, L. Löfgren, M. Bonnet-Eymard, M. Stuckelberger, S. Hänni, M. Boccard, G. Bugnon, M. Despeisse, F.-J. Haug, F. Meillaud, and C. Ballif, "Amorphous silicon-germanium for triple and quadruple junction thin-film silicon based solar cells," *Solar Energy Materials and Solar Cells*, vol. 133, pp. 163–169, feb 2015. [Online]. Available: http://www.sciencedirect.com/science/article/pii/S0927024814005868

[87] G. Nakamura, K. Sato, and Y. Yukimoto, "Staebler-Wronski effects in hydrogenated amorphous SiGe," *Solar Cells*, vol. 9, no. 1-2, pp. 75–84, jun 1983. [Online]. Available: http://www.sciencedirect.com/science/article/pii/0379678783900777

[88] T. Unold, J. D. Cohen, and C. M. Fortmann, "Electronic mobility gap structure and deep defects in amorphous silicon-germanium alloys," *Applied Physics Letters*, vol. 64, no. 13, p. 1714, mar 1994. [Online]. Available: http://scitation.aip.org/content/aip/journal/apl/64/13/10.1063/1.111814

[89] J. David Cohen, "Light-induced defects in hydrogenated amorphous silicon germanium alloys," *Solar Energy Materials and Solar Cells*, vol. 78, no. 1-4, pp. 399–424, jul 2003. [Online]. Available: http://www.sciencedirect.com/science/article/pii/S0927024802004452

[90] M. Günes, M. E. D. Yavas, J. Klomfass, and F. Finger, "The effects of native and light induced defects on optoelectronic properties of hydrogenated amorphous silicon–germanium (a-SiGe:H) alloy thin films," *Journal of Materials Science: Materials in Electronics*, vol. 21, no. 2, pp. 153–159, 2009. [Online]. Available: http://dx.doi.org/10.1007/s10854-009-9886-3

[91] G. Ganguly, T. Ikeda, T. Nishimiya, K. Saitoh, M. Kondo, and A. Matsuda, "Hydrogenated microcrystalline silicon germanium: A bottom cell material for amorphous silicon based tandem solar cells," *Applied Physics Letters*, vol. 69, no. 27, p. 4224, dec 1996. [Online]. Available: http://scitation.aip.org/content/aip/journal/apl/69/27/10.1063/1.116993

[92] G. Ganguly, T. Ikeda, K. Kajiwara, and A. Matsuda, "Microcrystalline Silicon Germanium: An Attractive Bottom Cell Material for Thin-Film Silicon-Based Tandem Solar Cells," *MRS Proceedings*, vol. 467, p. 681, feb 1997. [Online]. Available: http://journals.cambridge.org/abstract_S1946427400317730

[93] R. Carius, J. Fölsch, D. Lundszien, L. Houben, and F. Finger, "Microcrystalline Silicon-Germanium Alloys for Absorption Layers in Thin Film Solar Cells," *MRS Proceedings*, vol. 507, p. 813, feb 1998. [Online]. Available: http://journals.cambridge.org/abstract_S1946427400254316

[94] T.-w. Li, J.-j. Zhang, Y. Cao, Z.-h. Huang, J. Ma, J. Ni, and Y. Zhao, "Optical absorption enhancement of uc SiGe:H films deposited via high pressure and

high power," *Optoelectronics Letters*, vol. 10, no. 3, pp. 202–205, 2014. [Online]. Available: http://link.springer.com/10.1007/s11801-014-4007-9

[95] J. C. Phillips, "Band Structure of Silicon, Germanium, and Related Semiconductors," *Physical Review*, vol. 125, no. 6, pp. 1931–1936, mar 1962. [Online]. Available: https://link.aps.org/doi/10.1103/PhysRev.125.1931

[96] A. Shah, J. Meier, E. Vallat-Sauvain, N. Wyrsch, U. Kroll, C. Droz, and U. Graf, "Material and solar cell research in microcrystalline silicon," *Solar Energy Materials and Solar Cells*, vol. 78, no. 1-4, pp. 469–491, 2003. [Online]. Available: http://www.sciencedirect.com/science/article/pii/S0927024802004488

[97] S. R. Dhariwal and M. Smirty, "On the sensitivity of open-circuit voltage and fill factor on dangling bond density and Fermi level position in amorphous silicon p–i–n solar cell," *Solar Energy Materials and Solar Cells*, vol. 90, no. 9, pp. 1254–1272, 2006. [Online]. Available: http://www.sciencedirect.com/science/article/pii/S092702480500245X

[98] S. K. Persheyev, V. Smirnov, K. A. O'Neill, S. Reynolds, and M. J. Rose, "Atmospheric adsorption effects in hot-wire chemical-vapor-deposition microcrystalline silicon films with different electrode configurations," *Semiconductors*, vol. 39, no. 3, pp. 343–346, mar 2005. [Online]. Available: http://link.springer.com/10.1134/1.1882798

[99] T. Matsui, K. Ogata, M. Isomura, and M. Kondo, "Microcrystalline silicon germanium alloys for solar cell application: Growth and material properties," *Journal of Non-Crystalline Solids*, vol. 352, no. 9-20, pp. 1255–1258, jun 2006. [Online]. Available: http://www.sciencedirect.com/science/article/pii/S0022309306002845

[100] T. Matsui, K. Ogata, C. Chang, M. Isomura, and M. Kondo, "Carrier collection characteristics of microcrystalline silicon germanium p i n junction solar cells," *Journal of Non-Crystalline Solids*, vol. 354, no. 19-25, pp. 2468–2471, may 2008. [Online]. Available: http://www.sciencedirect.com/science/article/pii/S002230930701469X

[101] T. Matsui, C.-W. Chang, M. Kondo, K. Ogata, and M. Isomura, "Effect of illumination induced space charge on photocarrier transport in hydrogenated microcrystalline SiGe p i n solar cells," *Applied Physics*

Letters, vol. 91, no. 10, p. 102111, sep 2007. [Online]. Available: http://scitation.aip.org/content/aip/journal/apl/91/10/10.1063/1.2779928

[102] T. Matsui, C.-W. Chang, T. Takada, M. Isomura, H. Fujiwara, and M. Kondo, "Microcrystalline Si Ge Solar Cells Exhibiting Enhanced Infrared Response with Reduced Absorber Thickness," *Applied Physics Express*, vol. 1, no. 3, p. 031501, mar 2008. [Online]. Available: http://iopscience.iop.org/article/10.1143/APEX.1.031501

[103] W. Shockley and H. J. Queisser, "Detailed Balance Limit of Efficiency of pn Junction Solar Cells," *Journal of Applied Physics*, vol. 32, no. 3, pp. 510–519, mar 1961. [Online]. Available: http://aip.scitation.org/doi/10.1063/1.1736034

[104] M. Tzolov, F. Finger, R. Carius, P. Hapke, C. Scholten, L. Houben, M. Luysberg, A. Mück, B. Rech, H. Wagner, H. Ehmann, E. Dunlop, P. Giannoulès, and J. Koehler, "Optical and transport studies on thin microcrystalline silicon films prepared by very high frequency glow discharge for solar cell applications," *Journal of Applied Physics*, vol. 81, no. 11, pp. 7376–7385, jun 1997. [Online]. Available: http://aip.scitation.org/doi/10.1063/1.365354

[105] C. Boehme, "Quantenchemische Berechnungen von Übergangsmetallkomplexen mit Liganden aus den ersten vier Hauptgruppen," Ph.D. dissertation, Philipps-Universität Marburg, 1998. [Online]. Available: http://archiv.ub.uni-marburg.de/diss/z1998/0346/pdf/dcb.pdf

[106] P. Klement, C. Feser, B. Hanke, K. v. Maydell, and C. Agert, "Correlation between optical emission spectroscopy of hydrogen/germane plasma and the Raman crystallinity factor of germanium layers," *Applied Physics Letters*, vol. 102, no. 15, p. 152109, apr 2013. [Online]. Available: http://aip.scitation.org/doi/10.1063/1.4802028

[107] M. Luysberg, P. Hapke, R. Carius, and F. Finger, "Structure and growth of hydrogenated microcrystalline silicon: Investigation by transmission electron microscopy and Raman spectroscopy of films grown at different plasma excitation frequencies," *Philosophical Magazine A*, vol. 75, no. 1, pp. 31–47, jan 1997. [Online]. Available: http://www.tandfonline.com/doi/abs/10.1080/01418619708210280

[108] H. Sai, T. Matsui, T. Koida, K. Matsubara, M. Kondo, S. Sugiyama, H. Katayama, Y. Takeuchi, and I. Yoshida, "Triple-junction thin-film silicon solar cell fabricated on periodically textured substrate with a stabilized efficiency of 13.6%," *Applied Physics Letters*, vol. 106, no. 21, p. 213902, may 2015. [Online]. Available: http://scitation.aip.org/content/aip/journal/apl/106/21/10.1063/1.4921794

[109] Y. Cao, J. Zhang, C. Li, T. Li, Z. Huang, J. Ni, Z. Hu, X. Geng, and Y. Zhao, "Hydrogenated microcrystalline silicon germanium as bottom sub-cell absorber for triple junction solar cell," *Solar Energy Materials and Solar Cells*, vol. 114, pp. 161–164, 2013. [Online]. Available: http://dx.doi.org/10.1016/j.solmat.2013.03.004

[110] C. Feser, "Integration von germaniumbasierenden pin-Strukturen in Silizium-Dünnschicht-Solarzellen," Ph.D. dissertation, Universität Oldenburg, 2012. [Online]. Available: http://oops.uni-oldenburg.de/1616/1/fesint12.pdf

[111] A. Terakawa, M. Shima, K. Sayama, H. Tarui, H. Nishiwaki, and S. Tsuda, "Optimization of a-SiGe:H Alloy Composition for Stable Solar Cells," *Japanese Journal of Applied Physics*, vol. 34, no. Part 1, No. 4A, pp. 1741–1747, apr 1995. [Online]. Available: http://stacks.iop.org/1347-4065/34/1741

[112] B. Rech, C. Beneking, and H. Wagner, "Improvement in stabilized efficiency of a-Si:H solar cells through optimized p/i-interface layers," in *Proceedings of 1994 IEEE 1st World Conference on Photovoltaic Energy Conversion - WCPEC (A Joint Conference of PVSC, PVSEC and PSEC)*, vol. 1. IEEE, 1994, pp. 472–475. [Online]. Available: http://ieeexplore.ieee.org/articleDetails.jsp?arnumber=520000

[113] T. Matsui, H. Sai, A. Bidiville, H.-J. Hsu, and K. Matsubara, "Progress and limitations of thin-film silicon solar cells," *Solar Energy*, vol. 170, pp. 486–498, aug 2018. [Online]. Available: https://www.sciencedirect.com/science/article/pii/S0038092X18305103

[114] N. Reininghaus, C. Feser, B. Hanke, M. Vehse, and C. Agert, "Amorphous single-junction cells for vertical BIPV application with high bifaciality," *Energy Science & Engineering*, vol. 4, no. 3, pp. 183–189, may 2016. [Online]. Available: http://doi.wiley.com/10.1002/ese3.116

[115] V. M. Görlitz, R. Minke, W. Trautvetter, and G. Weisgerber, "Struktur und Eigenschaften von Polyvinylfluorid (PVF) und Polyvinylidenfluorid (PVF2)," *Angewandte Makromolekulare Chemie*, vol. 29, no. 1, pp. 137–162, may 1973. [Online]. Available: http://doi.wiley.com/10.1002/apmc.1973.050290108

[116] T. Dullweber, C. Kranz, R. Peibst, U. Baumann, H. Hannebauer, A. Fülle, S. Steckemetz, T. Weber, M. Kutzer, M. Müller, G. Fischer, P. Palinginis, and D. Neuhaus, "The PERC+ Cell: a 21%-Efficient Industrial Bifacial PERC Solar Cell," in *31st European Photovoltaic Solar Energy Conference and Exhibition*, 2015, pp. 341 – 350. [Online]. Available: http://www.eupvsec-proceedings.com/proceedings?paper=35037

[117] J. Hohl-Ebinger and W. Warta, "Bifacial Solar Cells in STC Measurement," *Eupvsec*, vol. 25, no. 0, pp. 1358–1362, 2010. [Online]. Available: http://www.eupvsec-proceedings.com/proceedings?paper=7718

[118] U. Feister and R. Grewe, "Sectral Albedo Measurements in the UV and Visible Region over Different Types of Surfaces," *Photochemistry and Photobiology*, vol. 62, no. 4, pp. 736–744, oct 1995. [Online]. Available: http://doi.wiley.com/10.1111/j.1751-1097.1995.tb08723.x

[119] Tiocat International, "Canada's First Rooftop Bifacial Solar PV Installation. Accessed 03.02.2016." [Online]. Available: http://www.tiocoat.com/solar.html

[120] Y. K. Chieng and M. A. Green, "Computer simulation of enhanced output from bifacial photovoltaic modules," *Progress in Photovoltaics: Research and Applications*, vol. 1, no. 4, pp. 293–299, oct 1993. [Online]. Available: http://doi.wiley.com/10.1002/pip.4670010406

[121] L. Kreinin, N. Bordin, A. Karsenty, A. Drori, D. Grobgeld, and N. Eisenberg, "PV module power gain due to bifacial design. Preliminary experimental and simulation data," in *2010 35th IEEE Photovoltaic Specialists Conference*. IEEE, jun 2010, pp. 002 171–002 175. [Online]. Available: http://ieeexplore.ieee.org/articleDetails.jsp?arnumber=5615874

[122] K. Trapani and M. Redón Santafé, "A review of floating photovoltaic installations: 2007-2013," *Progress in Photovoltaics: Research and Applications*, vol. 23, no. 4, pp. 524–532, apr 2015. [Online]. Available: http://doi.wiley.com/10.1002/pip.2466

[123] A. Cuevas, A. Luque, J. Eguren, and J. del Alamo, “50 Per cent more output power from an albedo-collecting flat panel using bifacial solar cells,” *Solar Energy*, vol. 29, no. 5, pp. 419–420, 1982. [Online]. Available: http://www.sciencedirect.com/science/article/pii/0038092X82900780

[124] H. Mori, “Radiation energy transducing device,” oct 1966. [Online]. Available: https://www.google.com/patents/US3278811

[125] A. Luque, J. M. Ruiz, A. Cuevas, J. Eguren, and M. G. Agost, “Double sided solar cells to improve static concentration,” *In: Photovoltaic Solar Energy Conference*, pp. 269–277, 1978. [Online]. Available: http://adsabs.harvard.edu/abs/1978pvse.conf..269L

[126] Solarworld, “Photovoltaik-Anlage, Modulhalter-System und Reflektor Photovoltaic system, module holder and reflector system.” dec 2014. [Online]. Available: http://www.google.com/patents/DE202014105516U1?cl=en

[127] T. Joge, Y. Eguchi, Y. Imazu, I. Araki, T. Uematsu, and K. Matsukuma, “Basic Application Technologies of Bifacial Photovoltaic Solar Modules,” *Electrical Engineering in Japan*, vol. 149, no. 8, pp. 32–42, 2004.

[128] Ertex-solar, “Gebäudeintegrierte Photovoltaik, Austria. Accessed 2016-02-04.” [Online]. Available: http://www.ertex-solar.at/presse/bilderarchiv/cat_view/27-picture-library/46-sound-protection

[129] S. Ito, S. M. Zakeeruddin, P. Comte, P. Liska, D. Kuang, and M. Grätzel, “Bifacial dye-sensitized solar cells based on an ionic liquid electrolyte,” *Nature Photonics*, vol. 2, no. 11, pp. 693–698, oct 2008. [Online]. Available: http://dx.doi.org/10.1038/nphoton.2008.224

[130] M. Abbott, J. Cotter, and K. Fisher, “N-Type Bifacial Solar Cells with Laser Doped Contacts,” in *2006 IEEE 4th World Conference on Photovoltaic Energy Conference*, vol. 1. IEEE, may 2006, pp. 988–991. [Online]. Available: http://ieeexplore.ieee.org/articleDetails.jsp?arnumber=4059796

[131] A. Hübner, A. G. Aberle, and R. Hezel, “Novel cost-effective bifacial silicon solar cells with 19.4% front and 18.1% rear efficiency,” *Applied Physics Letters*, vol. 70, no. 8, p. 1008, feb 1997. [Online]. Available: http://scitation.aip.org/content/aip/journal/apl/70/8/10.1063/1.118466

[132] A. Kranzl, R. Kopecek, K. Peter, and P. Fath, “Bifacial Solar Cells on Multi-Crystalline Silicon with Boron BSF and Open Rear Contact,” in *2006 IEEE 4th World Conference on Photovoltaic Energy Conference*, vol. 1. IEEE, may 2006, pp. 968–971. [Online]. Available: http://ieeexplore.ieee.org/articleDetails.jsp?arnumber=4059791

[133] C. Voz, D. Muñoz, M. Fonrodona, I. Martin, J. Puigdollers, R. Alcubilla, J. Escarre, J. Bertomeu, and J. Andreu, “Bifacial heterojunction silicon solar cells by hot-wire CVD with open-circuit voltages exceeding 600 mV,” *Thin Solid Films*, vol. 511-512, pp. 415–419, jul 2006. [Online]. Available: http://www.sciencedirect.com/science/article/pii/S0040609005023187

[134] U. Eitner, S. Kajari-Schröder, M. Köntges, and H. Altenbach, “Shell-like Structures: Non-classical Theories and Applications,” H. Altenbach and A. V. Eremeyev, Eds. Berlin, Heidelberg: Springer Berlin Heidelberg, 2011, ch. Thermal St, pp. 453–468. [Online]. Available: http://dx.doi.org/10.1007/978-3-642-21855-2_29

[135] H. Taha, “Urban climates and heat islands: albedo, evapotranspiration, and anthropogenic heat,” *Energy and Buildings*, vol. 25, no. 2, pp. 99–103, 1997. [Online]. Available: https://www.sciencedirect.com/science/article/pii/S0378778896009991

[136] P. HOFFMAN and G. Frey, “Praxistest "Moderne Energiesparsysteme im Haushalt",” *Institut für ZukunftsEnergieSysteme, Saarbrücken*, 2012. [Online]. Available: http://www.izes.de/cms/upload/publikationen/EM_8_705.pdf

[137] G. Ruichao, H. Hongtao, C. Paichun, L. Linfeng, C. Xiaoyuan, Y. Xiaofei, F. Zhiyong, Z. Benpeng, and L. Dongdong, “Coupled optical and electrical modeling of thin-film amorphous silicon solar cells based on nanodent plasmonic substrates,” *Nano Energy*, vol. 8, pp. 141–149, 2014. [Online]. Available: https://www.sciencedirect.com/science/article/pii/S2211285514001050

[138] H. Lerchenmüller, A. W. Bett, J. Jaus, and G. Willeke, “Cost and market perspectives for FLATCON-systems,” *Proceedings of the 3rd International Conference on Solar Concentrators for the Generation of Electricity or Hydrogen*, 2005. [Online]. Available: https://www.researchgate.net/profile/Andreas_Bett/publication/238681317_Cost_and_market_perspectives_for_FLATCON-systems/links/00b7d52bed48809f09000000.pdf

List of Publications

Journal Publications

Related to this Work:

- N. Reininghaus, M. Kellermann, K. von Maydell and C. Agert, "Effects of process parameters on µc-$Si_{1-X}Ge_X$:H solar cells performance and material properties", *EPJ Photovoltaics,* vol. 6, p. 65301, 2015. [Online] Availible: http://dx.doi.org/10.1051/epjpv/2015002
- N. Reininghaus, C. Feser, B. Hanke, M. Vehse, and C. Agert, "Amorphous single-junction cells for vertical BIPV application with high bifaciality", *Energy Science & Engineering*, vol. 4, no. 3, p. 183-189, 2016. [Online] Available: http://dx.doi.org/10.1002/ese3.116
- B. Fernandez, L. Lobo, N. Reininghaus, R. Pereiro and A. Sanz-Medel, "Assessment of thin tandem solar cells by depth profile characterization using radiofrequency pulsed glow discharge-time of flight mass spectrometry", *Journal of Analytical Atomic Spectrometry*, vol. 165, p. 289-296, 2016. [Online] Available: http://dx.doi.org/10.1016/j.talanta.2016.12.062

Other:

- A. Castro-Carranza, J.C. Nolasco, N. Reininghaus, S. Geißendörfer, M. Vehse, J. Parisi, J. Gutowski, and T. Voss, "Analytical energy-barrier-dependent V_{oc} model for amorphous silicon solar cells", *Applied Physics Letters*, vol. 109, no. 4, 2016. [Online] Available: http://scitation.aip.org/content/aip/journal/apl/109/4/10.1063/1.4959939
- R. E. Nowak, S. Geißendörfer, K. Chakanga, M. Juilfs, N. Reininghaus, M. Vehse, K. von Maydell and C. Agert, "Optimizing Folded Silicon Thin-Film Solar Cells on ZnO Honeycomb Electrodes", *IEEE Journal of Photovoltaics*, vol. 5, no. 2, p.

479-486, 2015. [Online] Available: http://dx.doi.org/10.1109/JPHOTOV.2014.2388079

Conference Contributions

Related to this Work:

- N. Reininghaus, T. Kilper, S. Geißendörfer, M. Kellermann, K. von Maydell, C. Agert, "Development of a-Si:H/μc-Si:H/μc-$Si_{1-X}Ge_X$:H Triple Solar Cells with Thin Absorber Layers", *28th European Photovoltaic Solar Energy Conference and Exhibition*, p. 2520-2523, 2013. [Online] Available: http://dx.doi.org/10.4229/28thEUPVSEC2013-3CV.1.30
- N. Reininghaus, C. Feser, K. von Maydell, "Investigation of Bifacial Thin-Film Silicon Solar Cells for Building Integration", *29th European Photovoltaic Solar Energy Conference and Exhibition*, p. 3837-3841, 2014. Available: http://dx.doi.org/10.4229/EUPVSEC20142014-6AV.5.39
- N. Reininghaus, S. Kirner, B. Stannowski, O. Gabriel, T. Kilper, K. von Maydell, R. Schlatmann, C. Agert, "Thin Triple Junction Cells with New Absorber Layer For Enhanced Current Generation", *29th European Photovoltaic Solar Energy Conference and Exhibition*, p. 1614-1619, 2014. Available: http://dx.doi.org/10.4229/EUPVSEC20142014-3CV.1.5
- N. Reininghaus, T. Kilper, K. von Maydell, and C. Agert, "Effects of Process Parameters on a-Si:H/μc-Si:H/μc-$Si_{1-X}Ge_X$:H Solar Cells Performance and Material Properties", *Photovoltaic Technical Conference*, **Poster and Flash Talk**, 2014
- N. Reininghaus, C. Feser, B. Hanke, M. Vehse and C. Agert, "Optimized Thin Amorphous Bifacial Single Junction Cells for BIPV Application", *30th European Photovoltaic Solar Energy Conference and Exhibition*, **Poster**, 2015.
- N. Reininghaus, "New Layers for Thin Triple Junction Cells" *EHF-Kompaktseminar*, **Talk**, 2014.

Other:

- U. Banik, N. Reininghaus, M. Vehse, C. Agert, "Long Term Stability Test and Analysis of Amorphous Silicon Glass-Glass Modules", *33rd European Photovol-*

taic Solar Energy Conference and Exhibition, p. 1784 - 1789, 2017. [Online] Available: http://dx.doi.org/10.4229/EUPVSEC20172017-5DV.3.19

Erklärung gemäß §11 der Promotionsordnung

Hiermit erkläre ich, dass ich die vorliegende Dissertation selbstständig verfasst und nur die angegebenen Hilfsmittel benutzt habe. Die Arbeit wurde weder in ihrer Gesamtheit noch in Teilen einer anderen wissenschaftlichen Hochschule zur Begutachtung in einem Promotionsverfahren vorgelegt. Die Leitlinien guter wissenschaftlicher Praxis an der Carl von Ossietzky Universität Oldenburg wurden befolgt. Außerdem wurden im Zusammenhang mit dem Promotionsvorhaben keine kommerziellen Vermittlungs- oder Beratungsdienste (Promotionsberatung) in Anspruch genommen.

Oldenburg, 15th January 2019

Ort, Datum Nies Reininghaus

Danksagung

Eine Doktorarbeit ist in großen Teilen auch eine gemeinschaftliche Arbeit aller Menschen, die an ihrer Entstehung beteiligt sind. Mein Dank geht deshalb an alle unterstützenden Personen. Insbesondere auch diejenigen, die mir mit einem „Du schaffst das schon!“ immer wieder Mut gemacht haben. Speziell bedanke ich mich bei:

- Prof. Dr. Carsten Agert für die Betreuung und Begutachtung der Arbeit sowie für die Möglichkeit zur Durchführung der Promotion im DLR Institut für Vernetzte Energiesysteme.
- Prof. Dr. Jürgen Parisi für die Betreuung und die Übernahme des Zweitgutachtens.
- Dr. Karsten von Maydell für die Aufnahme in die Arbeitsgruppe und die anfängliche Betreuung der Arbeit.
- Dr. Martin Vehse für die weitere Betreuung der Arbeit und die Unterstützung im DLR Institut für Vernetzte Energiesysteme.

Weiterhin gilt mein herzlicher Dank:

- Dr. Beatriz Fernández García an der Universität Oviedo in Spanien für die rf-GD-ToFMS Messungen.
- Dr. Benedikt Hanke für sein Programm zum Meteonorm Auswerten und seine Unterstützung bei den Graphen zur Einstrahlung.
- Dr. Clemens Feser für seine Zusammenarbeit, insbesondere bei den Untersuchungen zu bifacialen Zellen.
- Martin Kellermann, Dr. Clemens Feser und Dr. Stefan Geißendörfer vom DLR Institut für Vernetzte Energiesysteme für die Unterstützung bei der Substratpräparation sowie bei PECVD- und Elektronenstrahlabscheidungen.
- Ortwin Siepmann, Martin Kellermann, Antje Schweitzer und Kristina Borzutzki vom DLR Institut für Vernetzte Energiesysteme für Laserstrukturierungen.

- Tim Möller und Ulrike Kochan vom DLR Institut für Vernetzte Energiesysteme für UV-VIS, Profilometer, Ellipsometer und EQE Messungen.
- Dr. Martin Vehse und Dr. Clemens Feser vom DLR Institut für Vernetzte Energiesysteme sowie Dr. Jörg Ohland von der Universität Oldenburg für das Korrekturlesen der Arbeit.
- Lea Brenningmeyer von der Universität Oldenburg für Ihre Unterstützung, Ihre Liebe und die sprachliche Korrektur der Arbeit.
- Jens Sürig-Morieng für die Unterstützung bei den Elektronenstrahlabscheidungen und allen anderen Bastelprojekten.
- Ulf Kirstein, Dr. Cordula Walder, Dr. Peter Klement, Dr. Kambulakwao Chakanga für die Unterstützung im Hocheffizienz-Team.
- dem gesamten Team vom DLR Institut für Vernetzte Energiesysteme, die meine Promotionszeit nicht nur durch wertvolle, witzige und interessante Diskussionen, sondern auch durch ihre Freundschaft bereichert haben!
- meiner Familie, meinen Freundinnen und Freunden für die Unterstützung und das Zuhören sowie für den nötigen Rückhalt die Promotion zu Ende zu bringen!

Nies Reininghaus

CURRICULUM VITAE

Gaststr. 17
26122 Oldenburg
☎ *015156332331*
✉ *nies.reininghaus@gmx.de*

Zu meiner Person

Geboren	am 17.02.1985 in Werther (Westf.)
Familienstand	ledig

Ausbildung

Schulbildung

1996 - 2004	Gymnasium Lage Abitur, *Note: 2,0*

Diplomstudium Physik

2004 - 2011	an der Universität Bielefeld
19.08.2011	Diplomarbeit
Titel	Elektronenmikroskopische Untersuchungen von Silizium-Dünnschicht-Tandemsolarzellen
Betreuer	Prof. Dr. Helmut Stiebig, Prof. Dr. Ulrich Heinzmann
Note	1.7

Promotion

2013 - 2018	Carl-von-Ossietzky-Universität in Oldenburg
durchgeführt am	DLR Institut für vernetzte Energiesysteme e. V.
betreut durch	Prof. Dr. Carsten Agert
Titel	Silicon Thin Film Concepts for Building Integrated Photovoltaic Applications

Wissenschaftliche Beschäftigungen

2006 - 2010	Teutolab Physik, Mitmachlabor für 4-6. Klassen
2008 - 2010	Tutor, Einführung in die Physik für Nebenfach 1 + 2
2008 - 2009	Praktikumsbetreuer für das Physik Grundpraktikum
2010 - 2012	Wissenschaftlicher Mitarbeiter am Institut für Innovationstransfer
2013-2015	Wissenschaftlicher Mitarbeiter am Projekt SiDS12+ des BMU und BMBF bei NEXT ENERGY
seit 2016	Projektleiter des INTERREG Projektes MOVERO beim DLR Institut für vernetzte Energiesysteme e. V.